Fluidic Sealing Fundamental Physics and Development for Turbomachinery Implementation

Hilfer, Michael

Fluidic Sealing

Fundamental Physics and Development for Turbomachinery Implementaion

Michael Hilfer

University of Durham

A thesis submitted for the degree of

Doctor of Philosophy

March 2016

This work is dedicated to Elisabeth and Valentin.

Acknowledgements

I would like to express my gratitude to my supervisors, Dr. Simon Hogg and Dr. Grant Ingram for their invaluable support, advise and patience. I appreciate their assistance in writing the reports, publications and this thesis. Their vast knowledge enriched my own and their enthusiasm, motivation and encouragement kept me going.

A very special thanks goes to all the members of the technical staff, who made this work with their skill and their patience possible: Colin, Tony, Gary, Tony, Ian, Stuart, Ian, Paul, Simon, Neil, Colin, Philip and Kevin.

I recognize that this research would not have been possible without the support and assistance of Cummins Turbo Technologies and, in particular, I wish to sincerely thank Phil Wild and Steven Rooks.

Many more people have contributed directly or indirectly to this thesis. I owe my gratitude to all those people.

I would also like to thank my wife for the support and love she provided without compromise.

And finally, to my son: I started this work for myself and finished for you.

Abstract

With ever growing demand on turbine manufacturers to offer higher efficiency and lower operational costs, new modern seals must be able to withstand higher temperatures, pressures and shaft speeds but at the same time efficiently restrict flow at peak and transient load conditions and withstand abrasion, erosion, oxidation and depositions. This work investigates an alternative seal design, the fluidic seal, which could satisfy the demands of new seal designs.

Fluid seals use a jet inclined upstream in direction of the leakage flow relying on the momentum exchange to block or reduce the leakage flow. Theoretically, fluidic seals could be implemented on any location where other seal designs are considered or installed.

This work concentrates on fluidic seal design implemented between rotor-shroud and housing of the steam and gas turbines. Numerical, analytical and experimental investigations were carried out to explore the fundamental principals of fluidic sealing, showing a possible leakage reduction of up to 40% compared to base configuration. Subsequently these principles were used to develop a fluidic seal on a small scale turbo expander unit.

Contents

List of Figures

List of Tables

Nomenclature

αg	Entrainment Coefficient	[]
α	Fluidic jet injection angle	$[deg]$
α_L	Jet Turning Angle	$[deg]$
Δp	Differential pressure	$[Pa]$
$\dot{m}$	Mass flow rate	$\left[\frac{kg}{s}\right]$
γ	Heat capacity ratio	[]
$\hat{R}$	Turbine Reaction Ratio	[]
∇	Nabla-Operator	[]
ω	Rotational speed	$\left[\frac{1}{s}\right]$
ϕ	Friction factor	[]
Ψ	Flow coefficient	[]
ψ	Flow coefficient	$\left[\frac{usgal}{min}\right]$
ρ	Density	$\left[\frac{kg}{m^3}\right]$
$\tilde{R}$	Specific gas constant	$\left[\frac{J}{kgK}\right]$
$\tilde{\alpha}$	Contraction Coefficient	[]
A	Area	$[m^2]$

b_i	Labyrinth fin root thickness	$[m]$
b_w	1/e - Width of the Gauss Function	$[m]$
c	Jet Distance from the Corner	$[m]$
C_d	Discharge coefficient	[]
C_f	Semi-empirical flow coefficient	[]
c_p	Specific heat capacity	$\left[\frac{J}{kgK}\right]$
D	Diameter	$[m]$
G	Specific gravity of the fluid	[]
g	Gravitation constant	$\left[\frac{m}{s^2}\right]$
H	Channel hight	$[m]$
h	Specific enthalpy	$[J]$
H_i	Clearance between labyrinth fin and opposing wall	$[m]$
HP	High Pressure	[]
IP	Intermediate Pressure	[]
K	Entrainment Constant	[]
L_i	Labyrinth cavity axial clearance	$[m]$
l_i	Labyrinth fin pitch	$[m]$
M	Momentum flux	$\left[\frac{Ns}{m^2s}\right]$
N	Number of restrictions	[]
P	Power	$[W]$
p	Static pressure	$[Pa]$
p_0	Total pressure	$[Pa]$

PR	Pressure Ratio	[]
Q	Flow Rate	$\left[\frac{m^3}{s}\right]$
R, r	Radius	$[m]$
T	Temperature	$[K]$
t_i	Labyrinth fin tip thickness	$[m]$
th	Jet Outlet Size	$[m]$
v	Velocity	$\left[\frac{m}{s}\right]$
v_s	Isentropic Fluid Velocity	$\left[\frac{m}{s}\right]$
V_t	Tangential velocity	$\left[\frac{m}{s}\right]$
v_t	Circumferential Velocity Ratio	[]
$y+$	Non-Dimensional Wall Distance	[]
z	Jet Path Length	$[m]$

Subscripts

0	Stagnation values
$i, 1...n$	Numeration

Chapter 1

Introduction

1.1 Application of Fluidic Sealing in Turbomachinery

The overall efficiency of gas and steam turbines is highly affected by the performance of the seals between the stationary and rotating components. For example in a steam turbine, the leakage flow between stationary and rotating parts can account for up to 29% of the total stage efficiency, as reported by Pastrana et al. [49]. Further studies showed, among others Steinetz et al [59], that reduced leakage flow would reduce specific fuel consumption leading to reduced fuel burn and reduced emissions. The fundamental requirements on all seal designs is to maintain an accurate clearance during any modes of operation and to provide significant reduction of the leakage flow rate. Another important requirement on the seal designs is extremely high durability especially on aero-engine applications. The requirements mentioned above are only partially satisfied by any given seal technology due to design constraints associated with, for example, installation space, cost, operational conditions and the materials used. Fluidic seal design technology has the theoretical potential to accommodate several of these constraints and could be used in many gas or steam sealing locations in modern gas and steam turbines to replace a more conventional seal design. This work investigates this alternative sealing technology, the fluidic seal, which could satisfy the demands for the new seal design in turbomachinery applications. The applications relating to turbines described in this thesis are just one of many potential opportunities for this new technology e.g. compressors, sealing along rotating shafts etc.

With the ever growing demand on turbine manufacturers to offer products with higher efficiency and lower operational costs, new seal designs must be able to withstand increasingly higher temperatures (with gas path temperatures above 1673 K in the first turbine stage, Chupp et al. [12]), pressures and shaft speeds whilst at the same time efficiently restricting leakage flow at peak and transient load conditions. They must also be resistive to abrasion, erosion, oxidation and depositions. A variety of new turbomachinery sealing arrangements and materials are constantly under development to satisfy the increasing requirements. Fluidic seals could offer robust, effective and relatively simple seal geometries with the potential to readily accommodate flexible operating conditions.

Fluidic seals use fluid jets inclined upstream in the direction of the leakage flow and rely on the momentum exchange to block or reduce the leakage flow. Theoretically, fluidic seals could be implemented in any location where conventional seal designs can be applied.

1.2 Seal Design Constraints in Turbomachinery

The fundamental design constraints of the main seal technologies in turbomachinery compared to the fluidic seal are summarised in Table 1.1 and in Figure 1.1 schematic drawings of the selected seals are shown.

Table 1.1: Selection of common Seal Types.

Seal Type	Rub Tolerance	Pressure Loading	Operation Issues e.g. Debris	Seal Performance Normalized
Labyrinth	χ	✓	-	100%
Brush	-	-	χ	≤20%
Fluidic	✓	✓	✓	60% - 70%

Rub Tolerance is an important design consideration. Labyrinth seals are usually rub intolerant with any rub event leading to considerable damage to the labyrinth seal and consequently sudden permanent performance drop (e.g. Mushrooming, Tooth Bending, Grooving, etc)[71],[17]. Brush seals are able to withstand a certain amount of rubbing, due to their specifically designed flexible bristles, which deflect in a rub

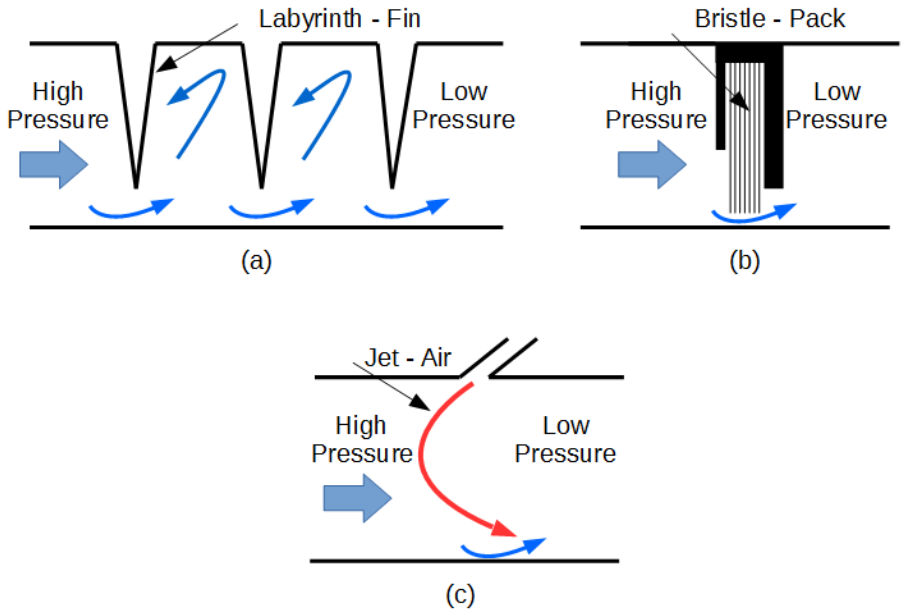

Figure 1.1: Schematic Drawings of Selected Seal Types: (a) - Labyrinth Seal, (b) - Brush Seal and (c) - Fluidic Seal

event [12]. Nonetheless, extensive rubbing still leads to bristle pack damage and gradually reduced sealing capability (e.g. bristles wear, rotor damage). Compared to labyrinth and brush seals, the pure fluidic seals do not feature components able to rub, so the rub tolerance constrain can be eliminated.

Pressure Loading is another important design constraint (pressure drop across the seal). Labyrinth seals are in general pressure loading insensitive and are able to withstand virtually any static and transient loading conditions. The brush seals are sensitive to high pressure loading with several effects emerging. On one hand, with increasing loading the so called blow-down effect moves the seal bristles toward the rotor, changing the lay angle and resulting in possible increased wear between bristle tips and rotor surface. On the other hand, high pressure loading can lead to reduced brush seal flexibility, also increasing wear in case of a rub event. Eventually, the over-pressurization of the brush seal leads to bending of the bristles under the backing plate and their permanent deformation, [12]. Fluidic seals are pressure loading insensitive requiring only higher jet inlet pressure to create a barrier at higher pressure loading.

Impact from Debris is another operational issue, which has to be considered when designing seals. In labyrinth seals, debris impact may lead to increased wear of the labyrinth fins and undesirable depositions, reducing the sealing capability, [12].

The bristle pack of a brush seal is very sensitive to debris impact, sometimes resulting in considerable damage to the bristles (breaking off), [12]. Since a pure fluidic seal does not feature components inside the leakage flow, the debris would pass the seal without causing any damage. Fluidic seals may also offer advantages with further operation issues, such as, high seal inlet temperature, fluid type (air, steam, oil mist, etc), axial rotor displacement, etc.

Seal Performance for similar size seals depends on the sealing clearance. Brush seals represent the best possible performance with the lowest effective clearance since they are designed with an interference fit between the bristle pack and the rotor. They offer more than 80% leakage reduction compared to equivalent labyrinth seals, [45]. If carefully implemented, fluidic seals offer up to 40% seal performance improvement compared to labyrinth seals.

As can be seen from Table 1.1 from a simple overview of design considerations, fluidic seal technology offers compelling advantages over other established seal technologies. The development of fluidic seal technology is the subject of this thesis.

1.3 Thesis Outline

This thesis consists of six further chapters, following this introduction.

Chapter 2: Literature Review contains a literature review of existing turbomachinery seal technologies before focusing on previous work on fluidic seals, notably the exceptional work of Curtis et al in 2009 [14]. This chapter concludes with a review of fluid seal modelling, which informs the work described in the following chapter, where the development of a new fluidic seal model is described.

Chapter 3: The Fluidic Seal Concept Developed during this Study and its Experimental Validation outlines a new patented concept for fluid seals and describes an analytical model of its behaviour. A new test facility is introduced in this chapter and experimental data obtained from the facility is used to validate the new fluidic seal concept. The potential of the fluidic seal to reduce leakage flow by over 40% is demonstrated.

Chapter 4: Design of a Fluid Curtain Seal to Reduce Rotor Tip Leakage on a Single Stage Turbo Expander Unit describes the design and the optimisation of a fluidic seal for a particular application - that of a single stage turbo expander unit. This chapter also introduces the modifications to the commercial turbo expander unit carried out to accommodate the new seal design.

Chapter 5: Static testing of the Turbo Expander Fluidic Seal Design to Demonstrate the Leakage Reduction Potential - "Mosquito" Tests. outlines the design of a static fluidic seal test rig using the rotor and the fluidic seal components from the Turbo Expander unit introduced in the previous chapter. The results obtained in this experiment verified the functionality of the fluidic seal design for this particular application.

Chapter 6: Fluidic Seal Tests on a Rotating Facility describes the design of a new rotating test facility including the modified turbo expander unit including the new fluidic seal geometry. In the rotating tests described in this chapter it was not possible to demonstrate the expected performance improvement. Possible causes are discussed and suggestions for improvement are presented, which will form a base for future work.

Chapter 7: Conclusion and Future Work presents and discusses an overview of the advances and principal findings from the investigations into fluidic seal devices described in this thesis. A number of suggestions for future work are listed at the end of this chapter.

Chapter 2

Literature Review

2.1 Overview: Seals in Turbomachinery

Since the early days of turbomachinery, engineers have faced the challenge of how to ensure that as much as possible of the fluid going through a turbine stage contributes to power generation, by flowing through the turbine blade rows and not circumventing them through the necessary gaps between the rotating parts and the stationary parts. Many authors e.g. Stocker [60] and Steinetz et al [59] suggested that, for example, in a gas turbine a reduction of 1% in leakage flow could lead to 1% increase in thrust and a 0.1% reduction in specific fuel consumption. Over the last 100 years, engineers have come up with a variety of different solutions to seal against leakage flows, such as labyrinth seals which appeared in the first gas turbines in early 1900s-1930s (Martin [40], Stodola [61], Egli [18]) and which are still widely used today. From 1960s (Chupp et al [12]) abradable materials were successfully used in combination with labyrinth seals to improve performance in aviation applications, but this technology has only slowly transitioned to industrial applications in turbines due to the longer service life needed. Brush seals were introduced in 1980s (Ferguson [21]) offering greatly reduced leakage flows but they have proved to be difficult to apply generally due to bristle wear rates and other effects such as pressure stiffening and hysteresis. Contacting seal designs such as brush seals, leaf seals etc are also more compact compared to the labyrinth seal designs, but are subjected to higher wear and performance reduction (Proctor and Delgado [50], Chupp et al [12]). Today, a variety of different solutions and combinations of the technologies described above are available, with each solution having its own advantages and disadvantages.

2.1.1 Early Non-Contacting or Clearance Seals

From 1900s to 1960s seals in gas and steam turbines were dominated by labyrinth seal designs. The first flying axial-compressor and -turbine gas engine (Junkers JUMO 004) featured several labyrinth seals in 1944, including one as shown in Figure 2.1 to create a seal between last compressor disc and the housing, which was also used to extract a fraction of compressed air for use in turbine blade cooling, Hirschel et. al. [32]. Still today labyrinth seals are used extensively in many modern turbomachinery designs with good performance and mechanical reliability. Further non-contacting seal designs include windback or windage seals which in cross section look similar to the labyrinth seals but work under different principles, see Section 2.1.1.2.

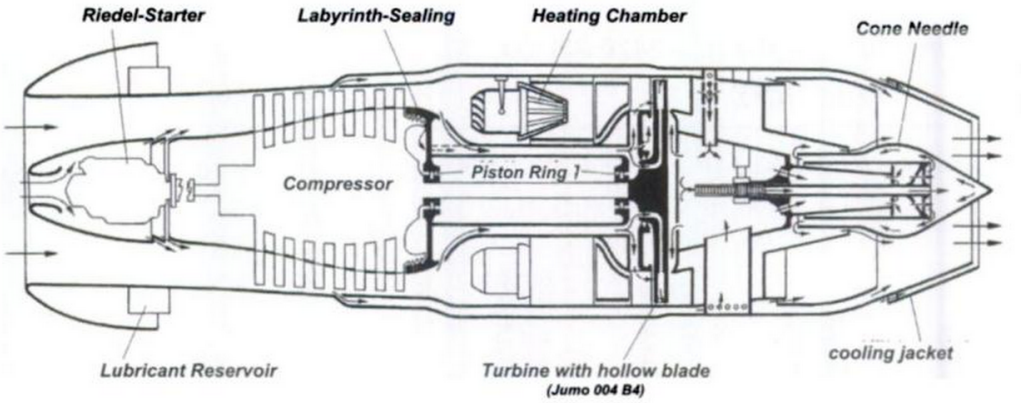

Figure 2.1: Cross Section of Junkers JUMO 004B4 Jet Engine, Hirschel et. al. [32]

2.1.1.1 Labyrinth Seals

The leakage rate of a labyrinth seal is largely dependent on the gap (H_i) between the labyrinth seal tooth or knife edge and the opposing surface as shown in Figure 2.2, and the differential pressure across the labyrinth of restrictions. The influence of seal geometry is highlighted in Figure 2.3 and is described by Equation 2.1 [46], where Q = flow rate in gallons per minute, ψ = rate of flow of water in US gallons per Minute at 60° F at a pressure drop of 1 psi, Δp = differential pressure across the labyrinth in psi and G = specific gravity of the fluid. In Figure 2.3 for comparable flow conditions the geometry with tighter clearance (H_i) offers lower flow coefficient and therefore the higher performance.

$$\psi = \frac{Q}{\sqrt{\frac{\Delta p}{G}}} \tag{2.1}$$

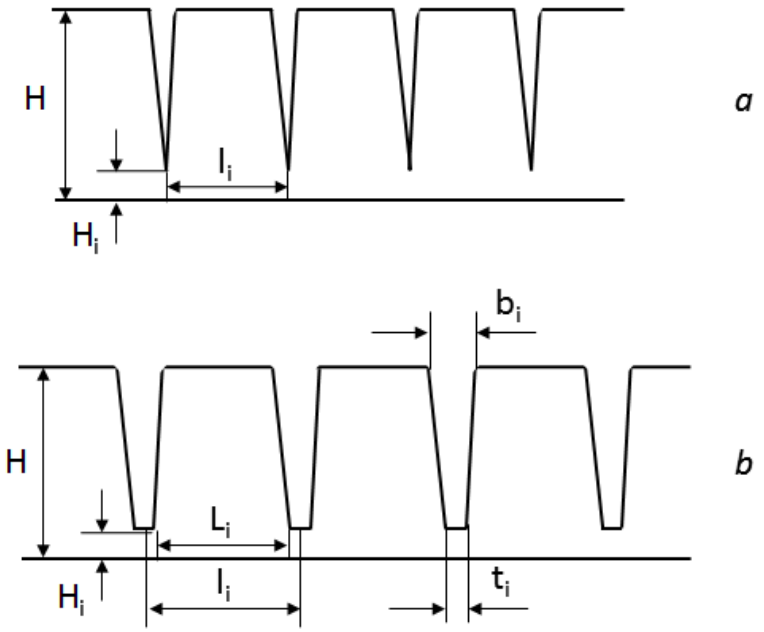

Figure 2.2: Notation for Labyrinth Seal Calculations: a) Knife Edge, b) Blunt Fin

The labyrinth seal restricts the leakage flow by first accelerating it through the clearance gap (H_i), which increases the kinetic energy of the fluid flow and the decelerating it in an uncontrolled expansion into the following cavity (H x L_i), with dissipation of the kinetic energy transforming it into heat energy, friction and turbulence (Egli [18], NASA [46]). This principle of acceleration, uncontrolled deceleration and dissipation is repeated in a sequence the restrictions and cavities along the labyrinth. In an ideal labyrinth seal, the kinetic energy of the accelerated fluid flowing under the labyrinth tooth is completely transformed into heat energy and turbulence in the following cavity (St. Venant-Wantzel, Vennard [68]), yet in a real labyrinth seal, only part of the kinetic energy is dissipated in this way, the remaining amount is passed on into the following tooth-cavity system (NASA [46]). Due to this kinetic energy carry-over, the ideal performance of the relations is modified in analytical models using empirical or semi-empirically defined factors as described later in Section 2.2. The amount of kinetic energy passed on is dependent on geometrical features of the seal fins such as their sharpness and shape of the tooth edge (t_i) (Mahler [39]) and

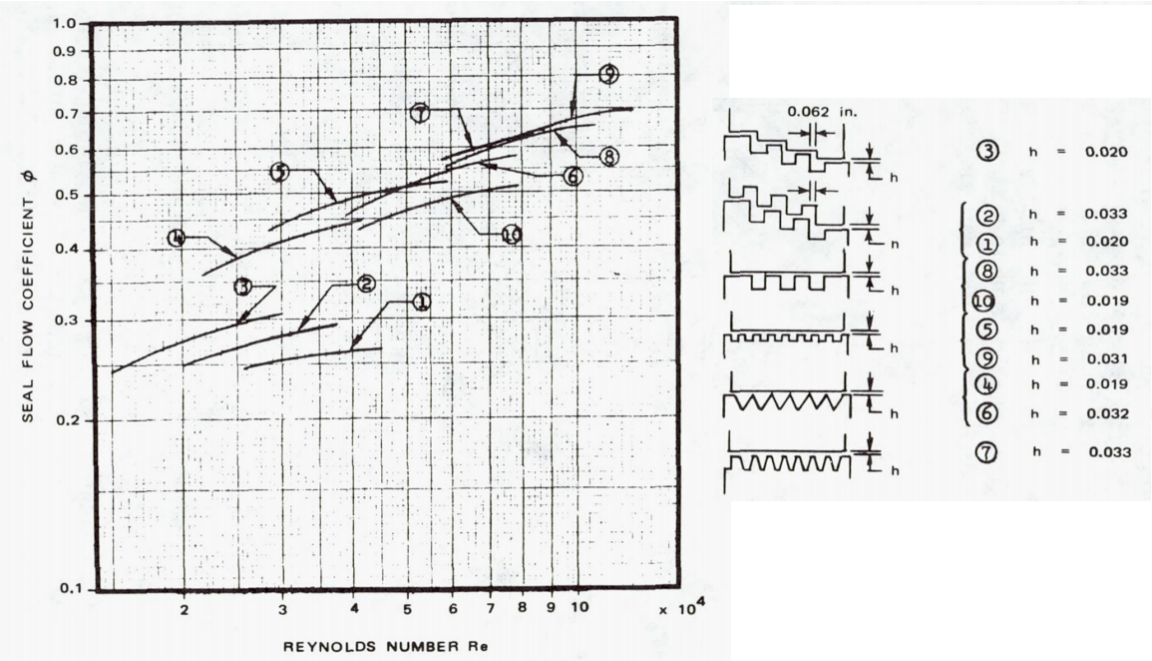

Figure 2.3: Change of Seal Flow Coefficient with Reynolds Number and Clearance Size for Various Labyrinth Seal Configurations, [46]. Sizes are in Inch

pitch (l_i) as well as depth of the cavity (H) (Hodkinson [33], Vermes [69], Egli [18] and others). Also, as tooth-cavity number is increased, each tooth-cavity system has to contribute less to the overall pressure reduction across the labyrinth, thus reducing kinetic energy carry over and increasing overall seal performance. In 1985 Hendricks and Stetz [30] derived a simple relation, Equation 2.2, between the number of tooth-cavity systems and leakage rate, based on observations of the flow through axially aligned orifices, where $\dot{m}$ = mass flow rate through the whole system, $\dot{m}_1$ = mass flow rate for a single restriction and N = the number of restrictions.

$$\frac{\dot{m}}{\dot{m}_1} = N^{-0.4} \tag{2.2}$$

Equation 2.2 also highlights that in order to achieve lower leakage rates, a higher tooth-cavity number and with it a larger installation space is needed, resulting in additional labyrinth seal weight, [46]. A selection of different labyrinth seal designs used in modern turbines is presented in Figure 2.4.

Compared to the straight labyrinth (a) and inclined seal (b) designs the furrow (c), full-labyrinth (d) and (up- or down-) stepped designs (e), offer improved performance due to their ability to prevent a substantial kinetic energy carry-over in the leakage

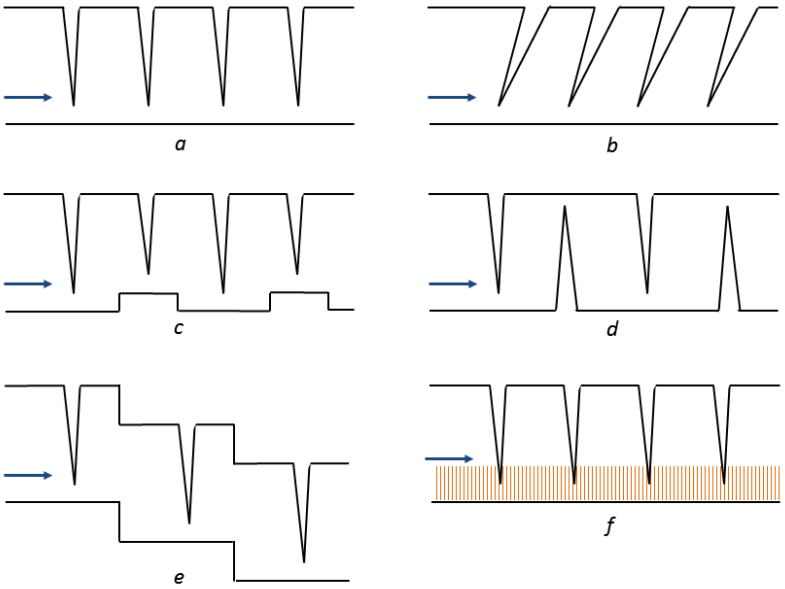

Figure 2.4: Variations off Labyrinth Seal Designs: a) Straight Labyrinth, b) Inclined, c) Furrow, d) Full-Labyrinth, e) Stepped, f) Wear-In in Combination with Abraidable Material

flow as a direct line-of-sight for the jet flow from one restriction to the next is not possible. However, they need more complex components as well as higher installation and maintenance effort, as installation in the axial direction is not possible and the seal ring has to be split. Figure 2.3 shows a better (lower) flow coefficient for stepped labyrinth seal designs compared to straight labyrinths for similar flow conditions with improvements of up to 50% [46].

The performance of any type of labyrinth seal is primary dependent on the size of the clearance between the tip of the labyrinth tooth and the opposing surface. A nominal gap size of between 0.2 mm and 1.0 mm can be found in a typical applications in steam and gas turbines, [13]. The greatest risk of contact between the labyrinth seal fins and their opposing sealing surface occurs during startup, shutdown and when changing load, Whalen [70], Hoopock [35], Cofer et al [13]. Cofer at al [13] reported that in a steam turbine application, the internal mid-span packing and the first three High Pressure (HP) and Intermediate Pressure (IP) stage diaphragm packing are most susceptible to rubs during the startup of the unit. A packing is a stationary seal arrangement, which may consist of different seal technologies assembled in one device, usually installed in two or more segments around a rotor.

Cofer et al [13] reported cases where the nominal design clearance of 0.381 mm had opened up after just five years of operation to 1.524 mm due to rubs. For gas turbine applications, Johnston [36] reports significantly higher seal clearances than originally designed (0.5mm to 1.5 mm) due to thermal growth and rotor movements during high vibration events. Johnston [36] also reports that for a MS7001E gas turbine unit, a rub of 0.5 mm on the labyrinth seal teeth reduces the performance of the unit by up to 1.0%. Rotor excursions and thermal expansion has to be taken into account when designing labyrinth seals. Gap sizes are set to mitigate the possibility of rubbing. The performance of the seal is calculated with an allowance for a certain degree of running-in and seal damage, accepting that there will be some performance reduction over time due to wear, [35].

Labyrinth seals can be used at very high rotor speeds, over a wide range of operating pressures and temperature and are relatively unaffected by displacement of the rotor due to periodic transient loads, [46], providing that any steps along the labyrinth seal leakage path have been carefully designed for a specific application.

2.1.1.2 Windback Seals

A windback seal is in many aspects similar to a straight labyrinth seal design. It features similar tooth geometry with similarly proportioned cavities (groves) between the teeth. However, in a windback seal the groove between the fins is arranged in a single continuous helical spiral as shown in Figure 2.5, Flitney [22], Neale [47], Schmal [55].

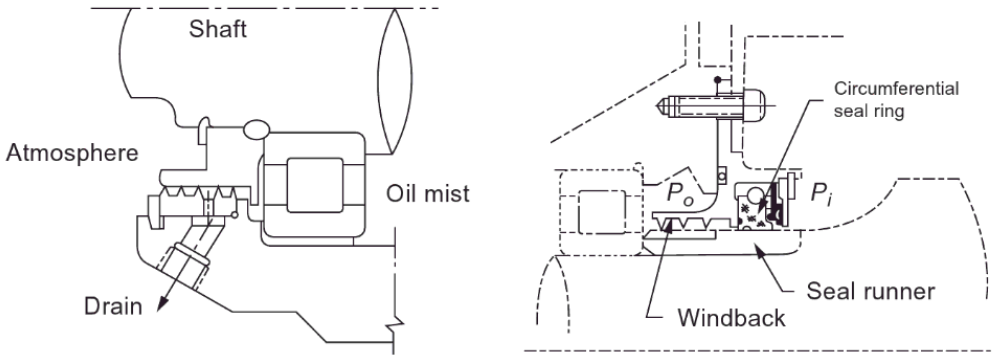

Figure 2.5: Variations off a Seal Assembly With Windback, Schmal [55]

This seal can be installed on the stationary components or on the rotational components, with fin clearances similar to labyrinth seals. It can be used in two different modes either to amplify the pressure difference across the seal or to create an adverse pressure gradient, by using the pumping effect from the rotation [22], [55]. In the first mode the rotation of the seal components coincides with the sense of rotation of the helix, which acts to increase the leakage flow, this mode is usually used to keep oil contaminations out of the internal gas flow through gas or steam turbines. In the second mode, the rotation of the seal opposes the rotational sense of the helix. In this configuration, the seal works to induce a pressure gradient that can lower the seal leakage flow-rate by using the pumping action to import additional momentum to the fluid in a direction opposite to the main flow direction. For gases, this type of seal has similar flow rates to labyrinth seals, with higher helix angle having a major effect on the performance of the seal [24], [55].

2.1.1.3 Abradable Seals

Abradable seals were first used in the late 60's in aero-turbine designs. They consisted of a soft material layer or honeycomb applied to one of the seal surfaces and conventional labyrinth seal fins mounted onto the other seal surface. This allowed the initial design labyrinth seal fin tip clearance to be set such that the labyrinth seal fins were able to machine their own minimum clearance into the abradable surface layer during the initial operation of the machine, as shown in Figure 2.6.

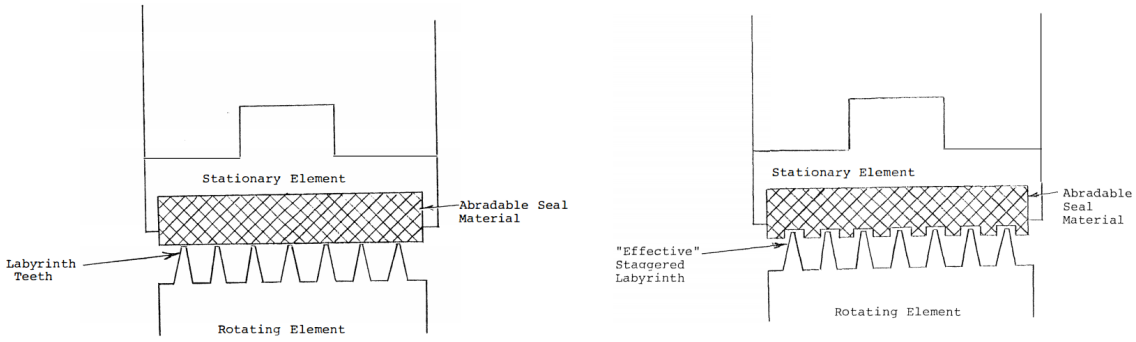

Figure 2.6: Labyrinth Seal on Rotating Component With Abradable Material on Opposing Surface Before (Left) and After (Right) Initial Operation [35].

Furthermore, the abradable materials were also used to reduce blade tip axial

and radial clearances on turbine configurations without blade shrouds, where, as on shrouded turbine blades, the abradable surface layer is sacrificed locally to minimize seal clearance without damaging the blades [35].

2.1.2 Contacting Seals

Compared to the non-contacting seals, the contacting seals are designed with an interference between the rotor and stationary seal components.

2.1.2.1 Brush Seals

Brush Seal were the first practical alternative seal design to labyrinth seals. They were first introduced in 1980s by Rolls Royce and MTU [26]. A typical early brush seal design consisted of a front plate, bristle pack and a back plate with bristle pack aligned radially and angled in the circumferential plane in the direction of the rotor. Figure 2.7 (Left) shows a typical brush seal cross section and in Figure 2.7 (Right) the radial bristle lay angle can be seen. In general, a brush seal offers better leakage flow performance compared to labyrinth seals, with leakage flow reductions of over 50% in some applications (see Section 2.1.5).

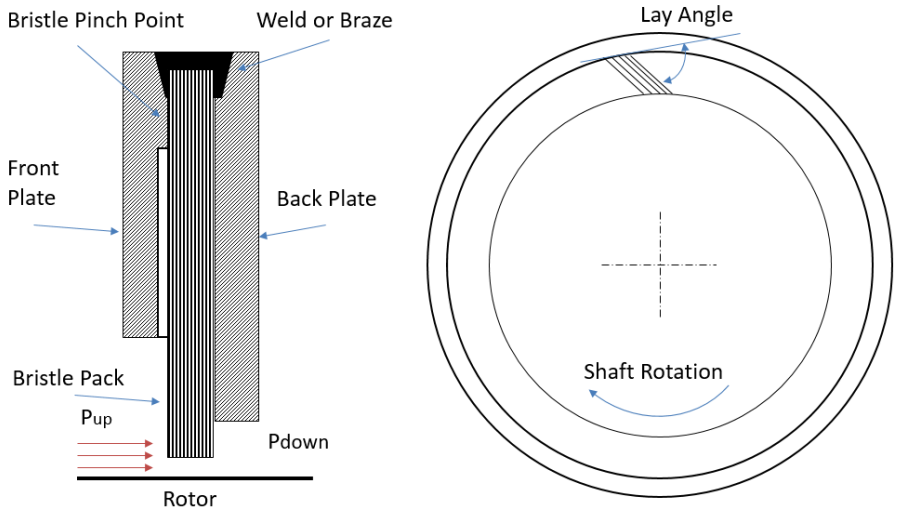

Figure 2.7: Typical Brush Seal Design (Left) With the Bristle Lay Angle (Right).

In a conventional brush seal design, the flexible bristle wire pack are clamped between an upstream front plate and a back plate on the downstream side. Usually by a weld on the top. Generally, the bristles are designed to have a small interference

with the rotor, with the intention that they will wear-in during initial operation, Dinc at al [16]. The performance of the seal varies depending on geometric features including brush pack stiffness and density as well as the thickness of the individual bristle wires, their material, the lay angle, the size of the upstream and downstream plates, among other parameters. In 1988, Ferguson [21] investigated the performance of the brush seals compared to labyrinth seals. He highlighted their potential for reducing leakage and their ability to accommodate significant shaft excursions, as well as the reduced requirement for axial space.

There are a number of important design considerations which need to be carefully taken into account when designing brush seals [16]. An excessive bristle interference can lead to high frictional heating of the seal and the rotor and high wear rate of bristles, leading to high performance degradation and, in worse case unacceptable shaft distortion. In highly swirling leakage flow environments, brush seal bristle flutter may occur, leading to aerodynamic bristle instability and fatigue [16]. Finally, the performance of a brush seal is highly dependent on the design of its bristle pack, affecting the operational live span, seal hysteresis, bristle stiffening and response to high pressure drop [56], [7].

2.1.2.2 Leaf, Film Riding Leaf and Finger Seals

A Leaf Seal is a variation on a brush seal where the bristle pack is replaced by a number of thin metal plates (leafs) inclined in the circumferential direction. The surface of the leaf oriented parallel to the axis of rotation, Figure 2.8. Compared to a brush seal, this configuration offers higher stiffness and rigidity at higher pressure drops across the seal and higher durability in case of contact with the rotor.

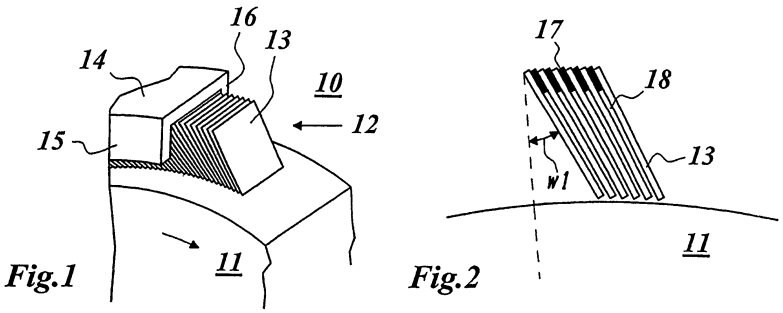

Figure 2.8: Typical Leaf Seal Design [25].

Film Riding Leaf seals are a relatively novel design first patented in 2003 by Grondahl et al. [25]. As shown in Figure 2.9 the film riding leaf seal consists of elastic thin leafs that are able to deflect in the axial direction due to the differential pressure drop across the seal [8]. The seal is designed to operate with a sealing clearance and hence avoid rubs during system start-up and shut-down, as well as of off design conditions.

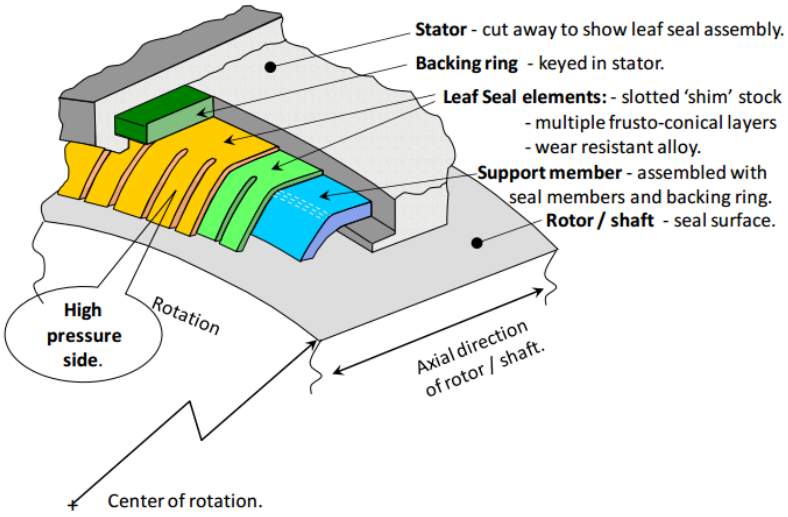

Figure 2.9: Film Riding Leaf Seal [4].

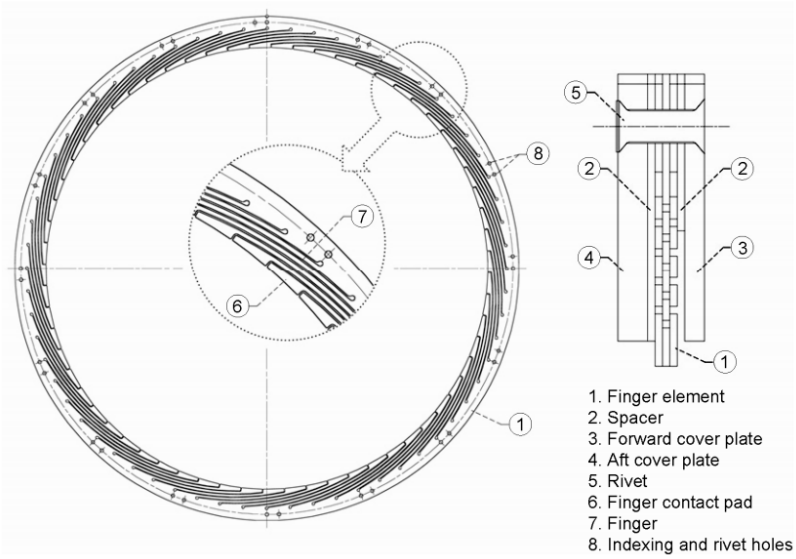

Figure 2.10: Basic Finger Seal Design. [15]

The finger Seal was patented in 2001 by AlliedSignal Engines (AE). It was initially

tested at the NASA Glenn Research Center and showed an improved performance compared to labyrinth seals at a price of up to 50% lower than that of an equivalent brush seals design [4]. The finger seal assembly (Figure 2.10) consists of multiple fingers or elements arranged around the circumference of the shaft and designed to bend radially (away from the rotor) to accommodate shaft excursions and rotor and seal thermal growth.

2.1.3 Damper Seals

In general, damper seals have the dual purpose of reducing leakage and adding additional damping to improve rotor-dynamic stability of high speed rotating systems, as shown by Vance and Li [66]. If the center of rotation of the shaft moves away away from the geometric centerline of a turbomachine due to, for example, rotor bowing, the seal clearances around the shaft will change with time. This will induce lateral forces on the rotor that are out of phase with the rotors displacement. This will result in aerodynamic excitation of the rotor that can lead to instability unless the system has sufficient damping, as shown by Hendrics [29] and Alfords [2].

2.1.3.1 Pocket Damper Seals

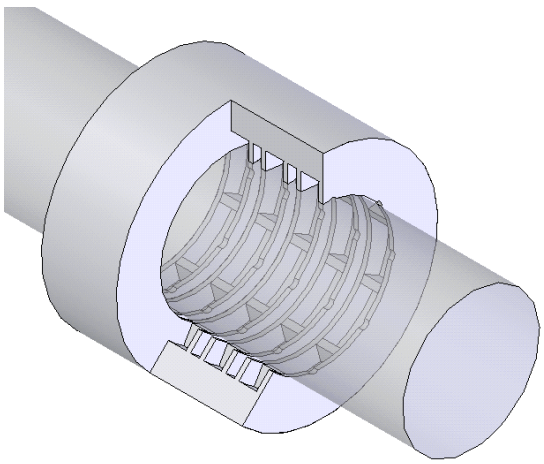

Figure 2.11: Pocket Damper Seal [23].

Pocket Damper Seals are the result of investigations into the dampening effects of labyrinth seals to determine and quantify positive and negative effects on rotor

dynamic stability. In 1965 Alford [2] presented one of the first predictions of damping coefficients for labyrinth seals. His work was limited to chocked flow through a two-tooth labyrinth seal. In 1991 Vance and Shultz [67] developed the pocket damper seal, by introducing circumferentially placed partitions in grooves of a labyrinth type seal, as shown in Figure 2.11. This reduced the ability of fluid to flow circumferential around the seal, thereby reducing circumferential differential pressure variations. Further, the introduction of partitions made the seal leakage flow more two dimensional and prediction using 2D models more accurate. Subsequently, a number of researchers showed positive dampening effects of pocket damper seals compared to similar labyrinth seals, without significant changes in leakage flow rates [23].

2.1.3.2 Honeycomb and Hole Pattern Seals

Amstrong and Perricone [3] showed in their research that honeycomb material applied as an annular seal could be used as a replacement for labyrinth seals, to seal the leakage flow and to greatly improve damping in steam turbines. Further, among others, Childs and Vance [11], [20] showed that honeycomb seals exhibit six times better damping effects compared to those of labyrinth seals. Hole Pattern Damper Seals were developed by the Dresser-Rand Company as an alternative to honeycomb damper seals. Childs et al [9] compared the leakage performance for a honeycomb seal (Figure 2.12a), labyrinth stator and a smooth stator . All seals had the same length (50.8 mm), radial clearance (0.41 mm) and rotor diameter (151.36 mm). They compared the flow coefficient, Equation 2.3, at constant rotor speed and seal pressure ratio with alternating circumferential velocity ratio v_t, Equation 2.4. The results showed a lower flow coefficient (ie. lower leakage flow) for the honeycomb seal (squares in Figure 2.12b) compared to the labyrinth seal (circles) and significantly lower flow coefficients than the smooth leakage channel (triangles), for all velocity ratios.

$$\psi = \frac{\dot{m}\sqrt{\tilde{R}T}}{\pi D H P_{0in}} \tag{2.3}$$

$$v_t = \frac{V_t}{R\omega} \tag{2.4}$$

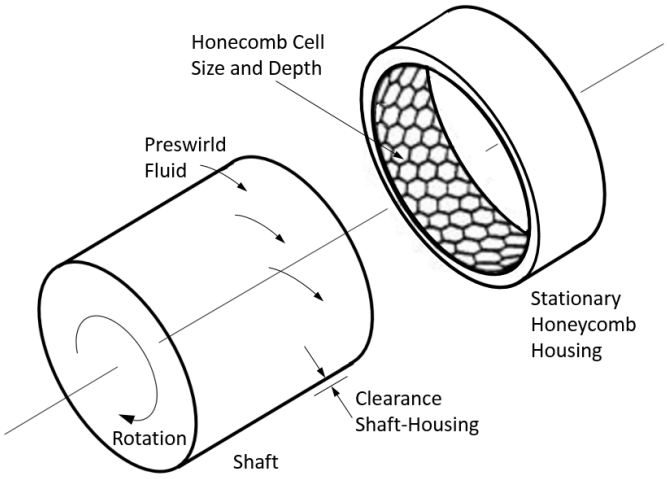

(a) Experimental Setup with Rotating Shaft and Stationary Honeycomb Seal, Childs et al [9].

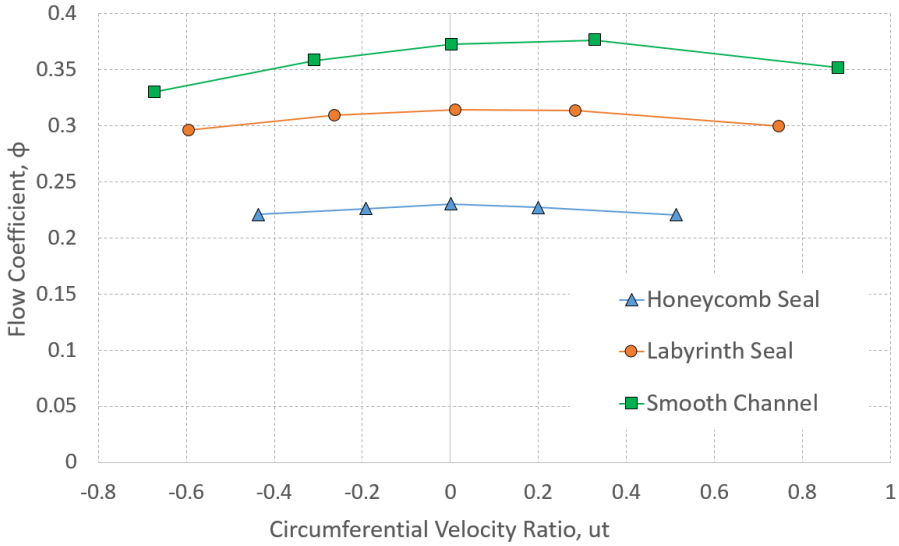

(b) Experimental Results for Honeycomb and Labyrinth Seal and a Smooth Leakage Channel, Childs et al [9].

Figure 2.12: Experimental Setup and Results of Seal Performance Comparison by Childs et al [9].

2.1.4 Fluidic Seals

Fluidic jet type seals are a non-contacting sealing technology that was first proposed in a patent by Auyer [6] in 1955. In an ideal fluidic seal, the physical restriction or restrictions normally present in conventional seals such as labyrinth seals, brush seals

etc are replaced by a high momentum fluid jet which enters the flow at an angle of between 0 and 90 degree opposing the main leakage flow, as shown in Figure 2.13. In principle, the high momentum fluid jet introduces a cross-flow which traverses the leakage path and creates a curtain type blockage. As shown in Figure 2.13, a pressure drop is required across the fluid jet in order for the jet momentum to be turned towards the direction of the main leakage flow. This pressure drop acts to effectively reduce the pressure gradient in the leakage channel upstream and downstream of the jet, thereby reducing the amount of leakage flow through it. This type of seal has a trade off because the jet flow has to be supplied from a high pressure location somewhere upstream of the seal, and so this flow is no longer available to produce useful work in the turbine. Any direct benefit from the fluidic seal needs to be greater than this reduction in work output for the fluidic seal to be effective.

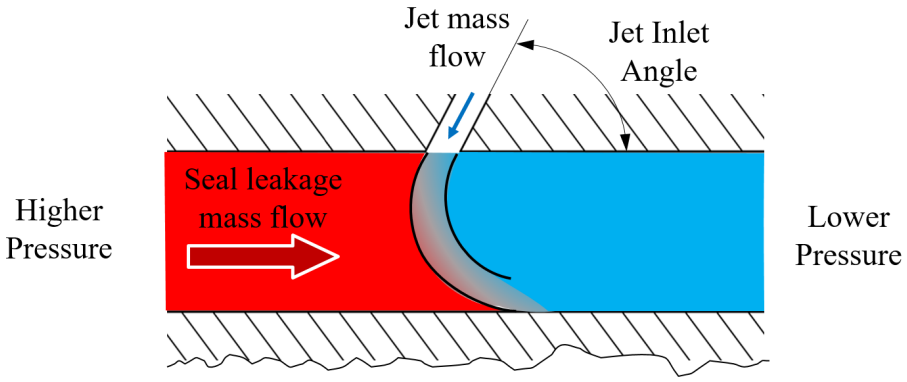

Figure 2.13: Principal Sketch of the Fluidic Jet Seal in a Generic Leakage Path.

2.1.4.1 Research on Fluidic Sealing Before 2012

In 2009, Curtis et al [14] noted that only few articles have been published on using curtain type fluidic jet seals to reduce turbine stage leakage flow. Descriptions of fluidic jet type seals are mainly found in patents dating back over several decades.

2.1.4.2 Fluidic Sealing Patents

The following patents show examples of fluidic type seals:

Auyer [6], 1954 Proposed placing an inclined jet over an unshrouded turbine blade row as shown in Figure 2.14. In this design a circumferential stationary part 11 is

introduced between the stationary housing and the rotor tip with an appropriate clearance between the rotor and the new part to avoid mechanical rub. A seal cavity 19 is supplied with fluid extracted from a preceding compressor. The high pressure seal fluid is then released into the clearance between he rotor and part 11 with high kinetic energy, introducing a significant velocity component in axial upstream direction. The main feature of the seal was to divert the hot gases into the blade passage for expansion. Additionally to sealing Auyer claimed a cooling effect in gas turbine applications provided by the relatively cold air from the compressor.

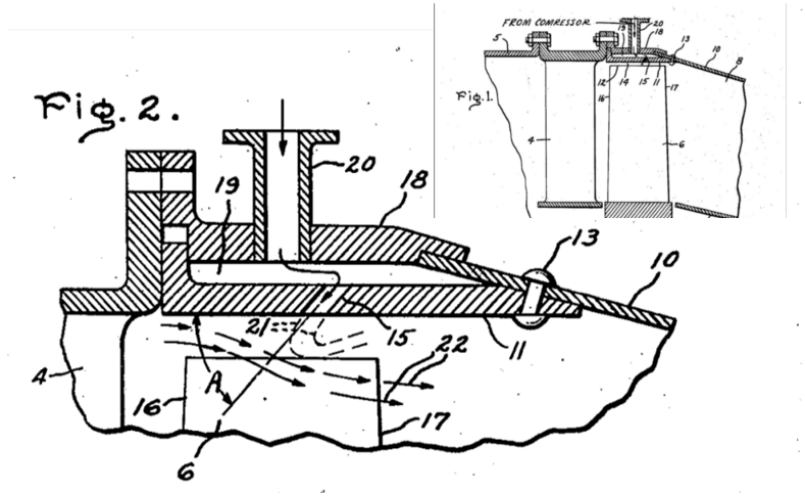

Figure 2.14: Inclined Jet Over Unshrouded Turbine Blade Row [6]

The shortcomings of the invention are apparent after the solidity of the circumferential blade tip area is considered. Here the seal generated by the introduced jet, is only functional over the relatively small solid tip surface, over the remaining unshrouded area the jet enters the blade passage and disturbs the flow creating additional losses, which Auyer aslo recognized [6]. No study of possible improvements or comparison with conventional seals were provided in the patent.

Smile [57], 1960 Suggested pressurizing a chamber-like structure between a rotating and stationary element, to form a pressurized seal, as shown in Figure 2.15. Smile claimed that, the main purpose of the invention was to create a sealing arrangement, that would cancel out or counteract centrifugal forces created by

fast rotation of the rotor using pressurized circumferential channels (position 19 in Figure 2.15). The part 19 could be a continuous circumferential channel or a honeycomb structure, according to the invention. A secondary purpose of the invention was to create a seal against the leakage flow and to provide a cooling effect. No evaluation of the performance or comparisons of the benefits with conventional seal designs, were provided with the invention.

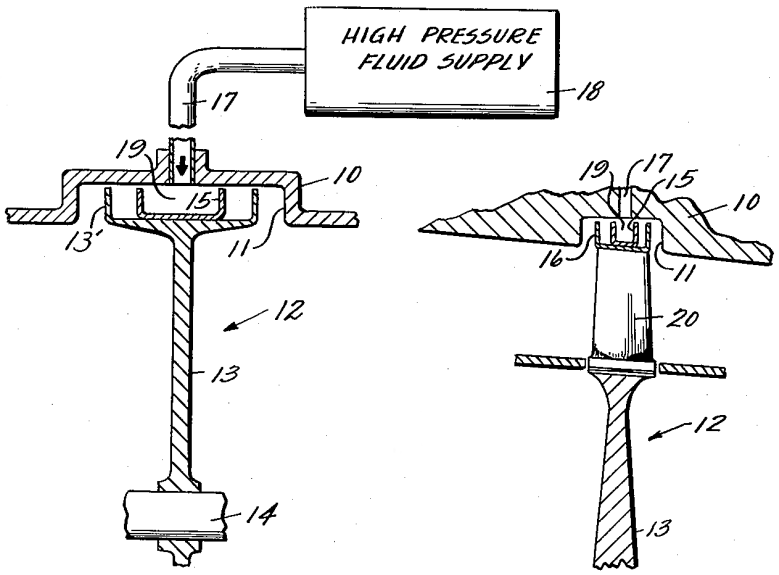

Figure 2.15: Pressurized Seal [57]

Unsworth and Burton [65], 1971 Suggested using an annular jet of fluid which is directed into the passage to prevent leakage of fluid along the passage defined by a turbine rotor and stator. In their suggestion, the jet is formed by a curtain of fluid between rotor and stator. Three variations of the invention are shown in Figure 2.16. The first, FIG 1., shows a variation that employs a single curtain type jet supplied by high pressure fluid creating a restriction between the housing and shroud surfaces. The second section view, FIG 2., shows a seal configuration where the jet air supplied through cavity 15 is extracted upstream of the jet inlet through port 16 and is supplied to a secondary jet curtain seal arrangement downstream of the first one, 18. Due to the pressure difference across the first jet curtain the higher pressure upstream of the first jet should be sufficient to create a secondary jet restriction. The third section view, FIG 3., is shows a seal arrangement where the high pressure air supplied through

cavity 15 is extracted through port 16 together with a part of the leakage flow and is used to supply a similar seal arrangement on a rotor downstream, which could be repeated for complete turbine arrangements.

Unsworth and Burton claimed in the patent that their invention enables steam turbines, for example, to be designed with a greater running clearance between selected portions of the rotor and the surrounding casing or diaphragms, thus reducing the danger of rotor damage occurring during operation. Furthermore, during assembly, the axial alignment of the rotor with respect to the surrounding casing becomes less critical than it is for when labyrinth type seals are employed.

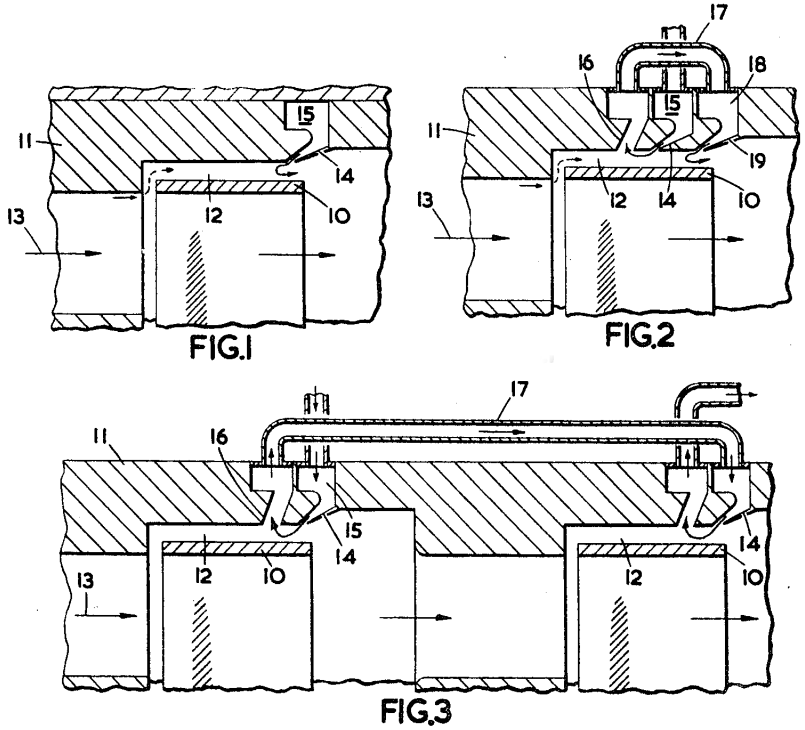

Figure 2.16: Pressurized Seal [65]

Similarly to other patents, no study of the seals performance or comparisons to conventional seal designs are described in the patent.

Turner [63], 1978 Proposed a fluid jet type seal applied upstream of a conventional seal such as labyrinth as depicted in Figure 2.17. Further, Turner claimed in his invention to be able to maintain reduced leakage over a wide range of clearances between the rotating and stationary parts during operation. The

primary feature of the invention was the nozzle 46 in Figure 2.17, which was positioned at the upstream end of a seal. The nozzle was oriented to discharge high pressure air in opposition to the leakage fluid flow approaching the seal. Turner also suggested a configuration where air was discharged perpendicular to the seal flow approaching the first labyrinth restriction. Turner also claimed in his invention a cooling effect, in case the high pressure air was supplied from a relatively low temperature environment.

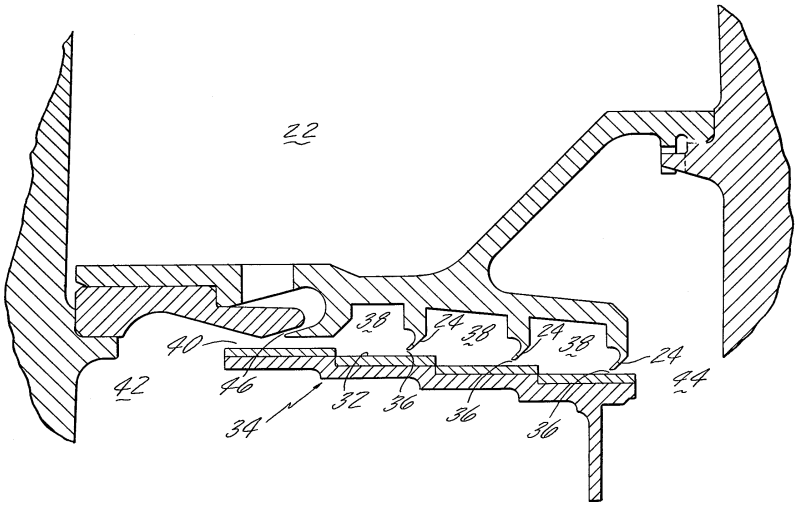

Figure 2.17: Fluidic type seal build around conventional seal [63]

As in all other patents presented above, no study of the seal performance or comparisons to the conventional seal designs was offered.

Minoda et al [43], 1988 Proposed an array of inclined blow holes extending circumferentially over an unshrouded turbine blade row as depicted in Figure 2.18. According to this invention, the holes were inclined with respect to the wall of the casing so the fluid discharging through the blow holes was opposing the primary fluid leakage flow through the clearances formed between the casing and the tips of the rotor blades. Thus, the leakage of the primary fluid was controlled by a hydro-mechanical effect, without changing the clearance geometry.

Minoda et al also reported in their patent, details of an experimental set-up that used a gas turbine and an arrangement of blow holes as shown in Figure 2.18, with 450 blow holes distributed circumferentially equidistant in three rows along

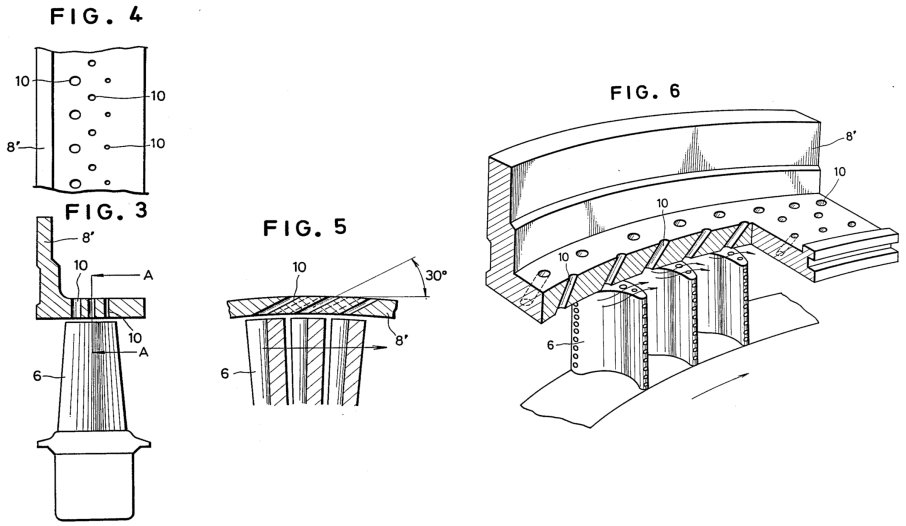

Figure 2.18: Inclined blow holes over unshrouded turbine row [43]

the chord of the rotor blade, with a clearance between the blade and casing of 0.5 mm. The results of the experiments showed that by increasing the flow rate through the blow holes, the leakage of primary fluid could be minimized and this resulted in additional work from the turbine in the blade tip region.

Turnquist et al [64], 2009 Suggested harvesting momentum of the flow through a labyrinth seal or in the first part of the seal to create a jet between labyrinth fins further downstream, as depicted in Figure 2.19. The invention was based on two primary principles. The first consideration was that the leakage flow inside the labyrinth seal immediately upstream of the jet outlet 28 would have a high momentum which could be harvested. The second principle was that in a conventional seal a reduced pressure downstream the jet inlet 24 along the leakage path was present so the fluid pressure supplying the jet seal was greater than the pressure at the axial position of the outlet 28 of the jet seal. In the patent modifications of the fluidic seal design were proposed employing various labyrinth seal configurations and including abradable surfaces.

No study of the seals performance or comparisons with other conventional seal technologies were given in the patent.

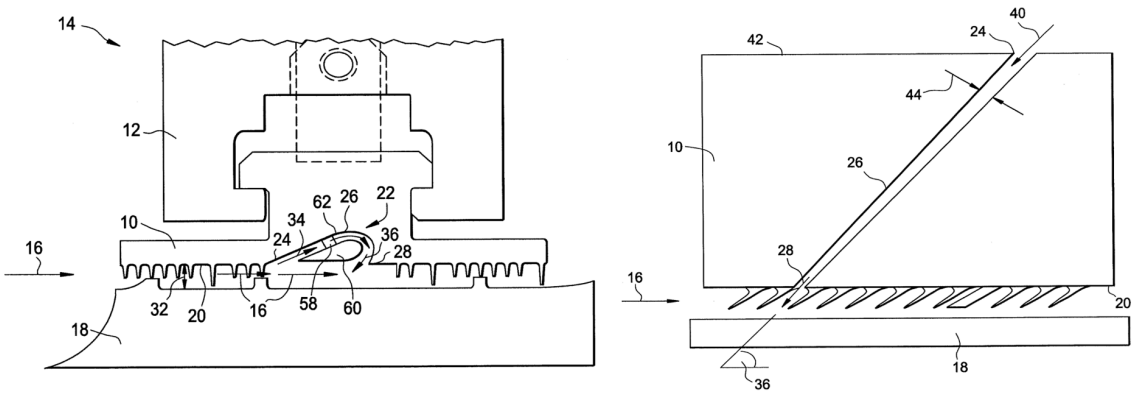

Figure 2.19: Fluidic Seal [64]

2.1.4.3 Fluidic Sealing Publications and Discussion

A fluidic type seal was examined experimentally, numerically and analytically by Curtis et al. [14] in 2009. Their experimental work was carried out on a single-stage, low-speed, axial-flow air-turbine test facility with a rotor tip radius of 0.5 m. A fluid jet was supplied through the turbine outer wall into the rotor blade tip-seal cavity above the turbine blade shroud as shown in Figure 2.20. The jet was inclined in an upstream direction to oppose the tip leakage flow above the blade shroud, in order to produce blockage and reduce the shroud leakage flow.

The results showed conclusively that net overall leakage reduction (jet flow plus shroud tip seal inlet flow) could be achieved relative to the baseline leakage flow without a jet present. These test results are shown in Figure 2.21 where the measured and calculated mass flows are presented as a percentage of main flow for seal inlet and seal outlet over a range of jet mass flow rates. The results show a decrease of the total leakage flow from 5% of the main flow to 3.5% of the main flow, an overall decrease of 30%.

In 2011 Hogg and Ruiz published a comparison of performance of different types of fluidic seal designs [34]. At first the authors investigated an air curtain type fluidic seal generated by a series of coalescing circular jets exhausted perpendicular to the leakage flow and supplied with air through a jet supply plenum, as shown in Figure 2.22. After an extensive numerical study using the geometry in Figure 2.22, they concluded that the maximum reduction of the leakage flow was modest ranging between 5% and 10% compared to the initial leakage flow rate. They concluded

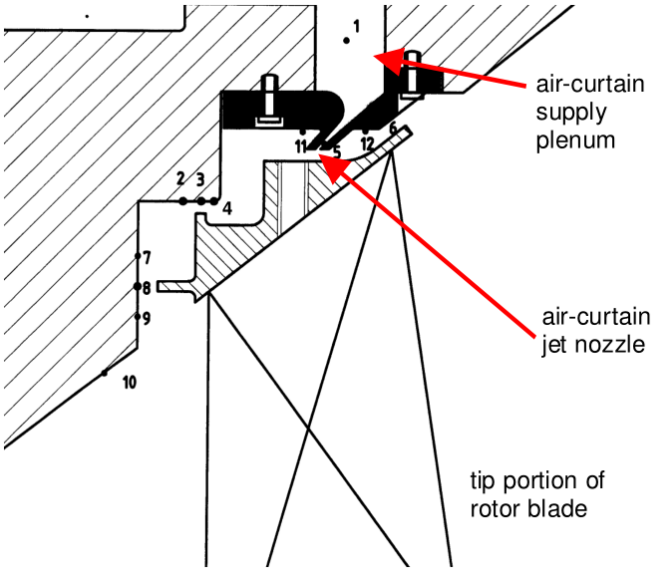

Figure 2.20: Details of the Air-Curtain Jet and Shroud Cavity Instrumentation Used by Curtis et al. [14], Nozzle Pieces Shown in Solid Black.

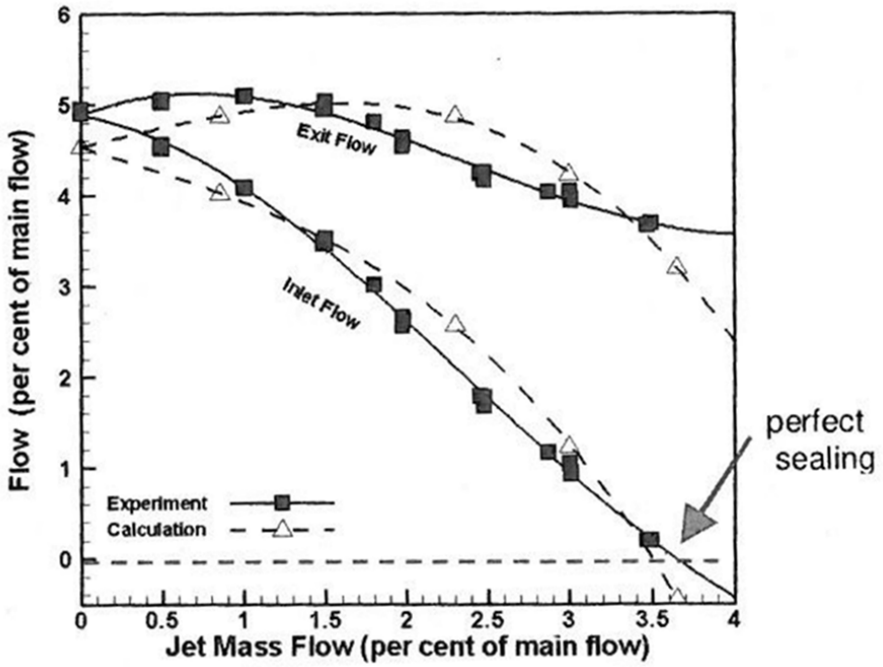

Figure 2.21: Measured and Calculated Variation of the Shroud Leakage Mass Flows with Changes in the Air-Curtain Sealing Mass Flow, Curtis et al. [14].

that this particular type of fluidic seal design has only limited potential for reducing leakage flows.

In a further numerical study, Hogg and Ruiz [34], proposed an alternative design,

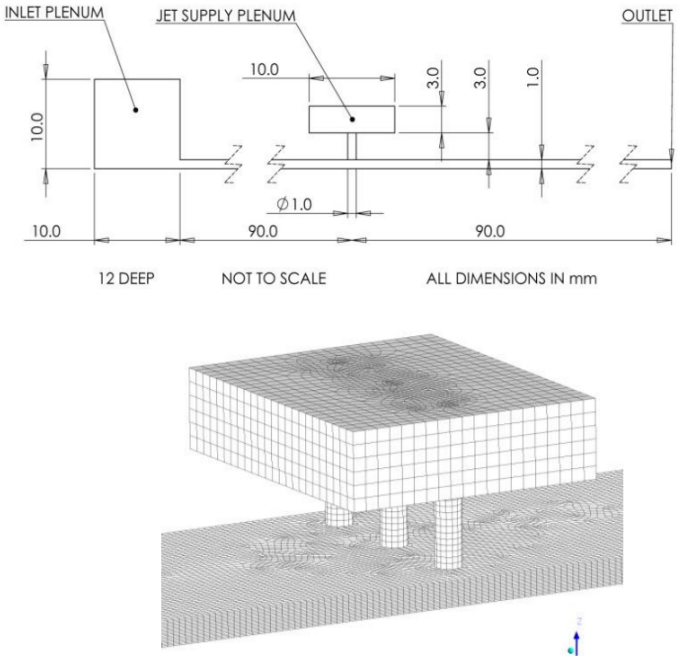

Figure 2.22: Domain Geometry with CircularJet Supply Holes as Used in Calculations by Hogg and Ruiz [34].

combining fluidic jets with a conventional labyrinth seal design. This design consisted of an idealized labyrinth seal geometry with fluidic jet supplied along an inclined tooth, as shown in Figure 2.23. The fluidic jet was introduced part-way along the seal leakage path between two labyrinth fins. The jet was modeled as a slot of 0.5 mm width, which was similar to the labyrinth tooth clearance size. Calculations were carried out for High Pressure and Low Pressure drop conditions. The calculations showed that a much greater potential for reducing leakage flows existed when fluidic jet curtains were combined with conventional labyrinth seal designs. In their study the leakage flow was reduced by up to 25% compared to the flow without the jet turned on.

2.1.5 Comparison of Conventional Seal Designs and Discussion

In the past, several studies have compared the performance of different seal designs. Amongst others Addy et al. [28], compared a new brush seal with a bristle-rotor interference of 0.1 mm with a 4-fin labyrinth seals with smooth and honeycomb abradable sealing surfaces. They concluded that a mass flow rate reduction between the

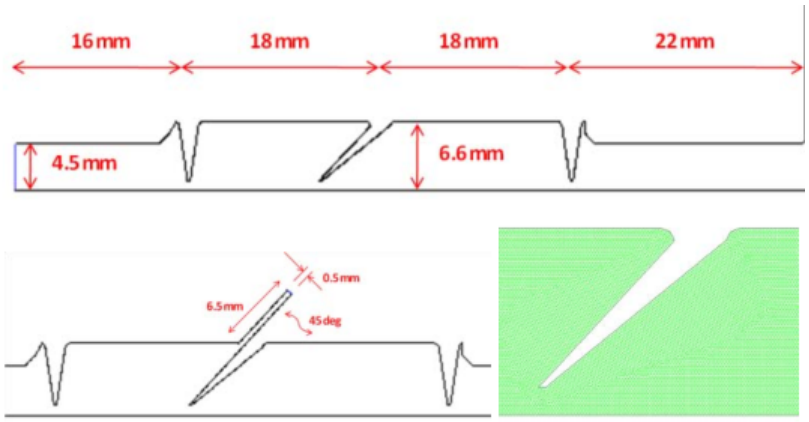

Figure 2.23: Idealized Labyrinth Seal Geometry and Mesh Used by Hogg and Ruiz [34] in their study.

smooth land labyrinth seal and the honeycomb layered labyrinth seal of 3 % could be achieved, and that the brush seal could reduce the mass flow by 92%. Ferguson [21] compared the leakage flow rate through various 5-toothed labyrinth seals designs featuring different clearances against a brush seal. In this study Ferguson [21] showed a consistent relationship between the clearance size and the flow rate with smaller clearances showing reduction of flow rates. Further the research showed that seals, which are designed to reduce the kinetic energy carry over effect (stepped labyrinth seal), reduced the flow rates even further. In an ideal seal, the kinetic energy of the jet is dissipated into heat energy in an repeated acceleration-deceleration process. Due to a kinetic energy carry over effect in a real seal, the kinetic energy is not completely transformed into the heat energy and is passed on into the following acceleration-deceleration process. Finally Ferguson [21] showed a significant reduction in flow rate for the single brush seal tested compared to the labyrinth seal designs. This comparison is shown in Figure 2.24.

In Figure 2.24 the results presented by Ferguson [21] have been combined with the results for fluidic seal from the work by Curtis et al [14] and Hogg and Ruiz [34] as well as by results from Auld et al [5] and Hilfer et al. [31] and which are part of the current study. The fluidic seal results have been calculated based on an assumed 30% improvement in labyrinth seal performance from introducing the fluidic jet upstream of the first labyrinth seal restriction (based on reported improvements of between 20% and 50% in [14], [34], [5], [31]).

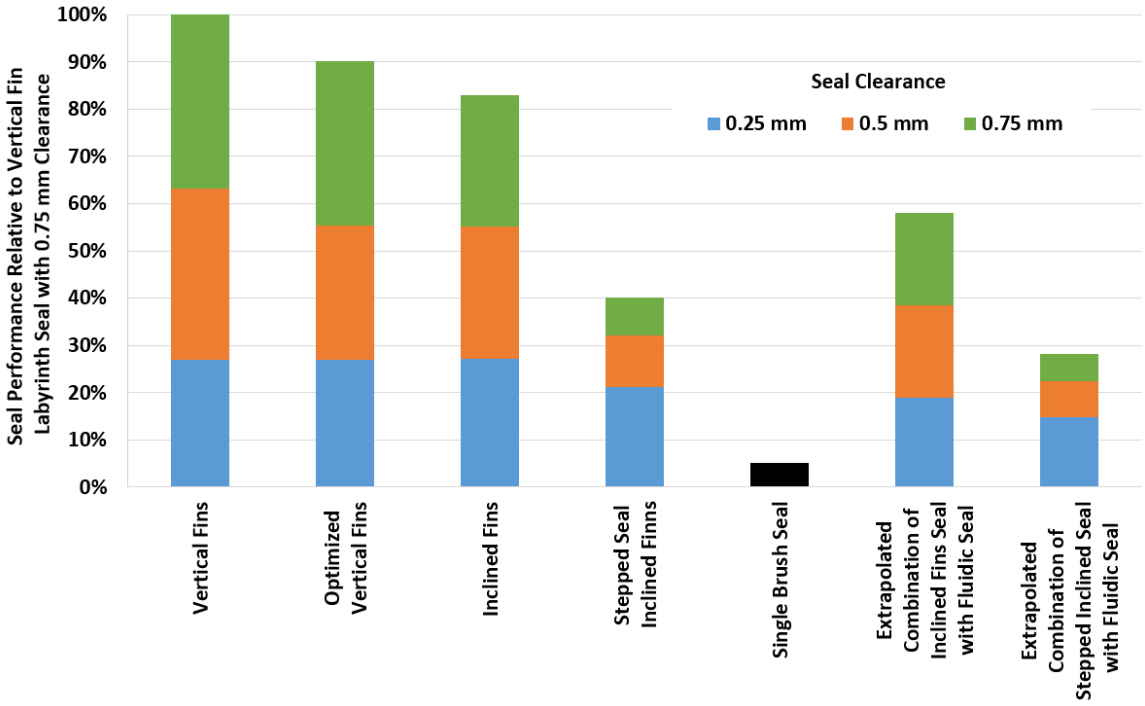

Figure 2.24: Five-Finned Labyrinth Seal Performance Compared to Single Brush Seal at a Pressure Ratio of 2 [21]. With Extrapolated Performances of Fluidic Seal - Labyrinth Seal Combination from Results by Curtis et al. [14] and Hogg and Ruiz [34]

In Figure 2.25, experimental leakage data for flow coefficients from experiments carried out by Childs at al. [20] are presented. The results were obtained with a consistent seal clearance (of 0.1 mm) for smooth rotor with smooth, honeycomb, hole pattern and labyrinth seal stator. The results showed that for the same clearances, the labyrinth with hole pattern seal had similar flow coefficients which are also significantly lower, approximately 26%, compared to the smooth bore flow coefficient. The flow coefficient for honeycomb seal was lower by approximately 13% compared to labyrinth seal and hole pattern seal.

Overall it can be noted that for similar size seals the primary leakage flow reduction can be achieved by reducing the sealing clearance. Brush seals represent the maximum possible clearance reduction since they are designed with interference and are able to deflect during operation in case of rotor excursion or thermal expansion. To further reduce leakage flow rates in labyrinth and similar seals the kinetic energy carry over effect has to be mitigated. The reduction of flow energy carry over can be achieved by introducing steps in the seal designs or through using restrictions on both seal

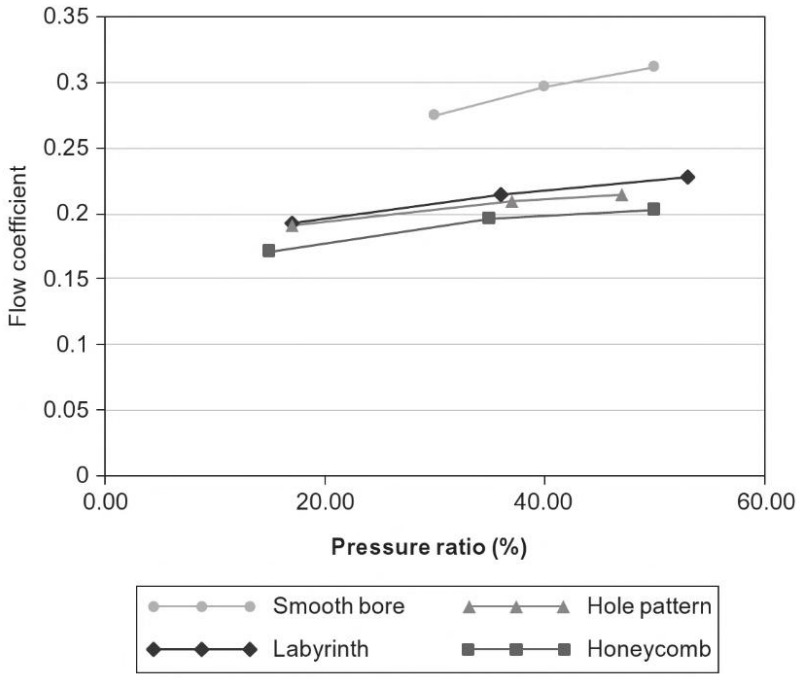

Figure 2.25: A Comparison of Flow Coefficients for Honeycomb, Hole Pattern and Labyrinth Seals at 0.1 mm Clearance Compared With a Smooth Bore Clearance [20].

surfaces. As noted previously steps and additional restrictions will all increase weight and impact manufactureability and repairability, plus a greater installation space will also be required.

2.2 Review of Calculation Methods for Clearance Seals.

In following sections some of the well established assumptions and calculation methods for clearance seals are reviewed. These will be used later to construct an analytical model of a fluidic seal.

2.2.1 Important Assumptions

The equations described in this review were used in publications by Martin (1908) ([40], Vennard (1940) [68], Gamal (2007) [19] and Childs (1993) [10] among others with following assumptions:

- Axial flow through the seal is not significantly affected by the tangential movement of the rotor and its boundary layer and/or the tangential movement of

the restricting component such as the labyrinth fin or brush.

- The flow is steady without any transient effects.
- The flow is adiabatic.
- The fluid behaves as an ideal gas.
- Rotating and stationary components remain concentric throughout operation.
- Initially the expansion after any restriction is assumed to be isentropic with uniformly distributed pressure.

2.2.2 Sub-Critical and Critical Flow Through an Ideal Nozzle

The flow through an ideal nozzle is assumed to be smooth without any losses associated with viscous effects. The fluid is assumed to behave as an ideal gas in accordance with equation (2.5).

$$p = \tilde{R} \cdot T \cdot \rho \tag{2.5}$$

If the fluid velocity through a nozzle increases beyond the sonic condition, the nozzle flow becomes choked. This means that any change in pressure downstream of the chocked nozzle does not have any further effect on the mass flow rate through it. Mass flow rate is then only governed by the pressure upstream of the nozzle. To calculate nozzle velocity (2.8) an enthalpy equation (2.6) is used with an ideal gas relation (2.7) and the ideal gas equation (2.5). The specific heat capacity factor (2.7) is dependent on the ideal gas property.

$$h_0 = h + \frac{v^2}{2} \quad \text{with} \quad dh = c_p \cdot dT \tag{2.6}$$

$$c_p = \frac{\gamma}{\gamma - 1} \cdot \tilde{R} \tag{2.7}$$

$$v = \sqrt{\frac{2\gamma}{\gamma - 1} \frac{p_0}{\rho_0} \left(1 - \frac{T}{T_0}\right)} \tag{2.8}$$

The isentropic gas relation (2.9) can be combined with equation (2.8) to produce the velocity equation (2.10).

$$\frac{T}{T_0} = \left(\frac{p}{p_0}\right)^{\frac{\gamma-1}{\gamma}} = \left(\frac{\rho}{\rho_0}\right)^{\gamma-1} \tag{2.9}$$

$$v = \frac{1}{\rho} \cdot \sqrt{p_0 \cdot \rho_0} \sqrt{\frac{2\gamma}{\gamma-1}\left[\left(\frac{p}{p_0}\right)^{\frac{2}{\gamma}} - \left(\frac{p}{p_0}\right)^{\frac{\gamma+1}{\gamma}}\right]} \tag{2.10}$$

The last part of the equation (2.10) is the flow function Ψ (2.11), which reaches its maximum as shown in Figure 2.26 when the fluid velocity is equal to speed of sound at critical pressure ratio (2.12). The maximum of the flow function is calculated by differentiation with respect to pressure ratio. In the case when the pressure ratio is equal or less than the critical pressure ratio, the flow function loses its dependency on pressure ratio and remains equal to its maximum value as shown in Equation (2.13) and plotted in Figure 2.27.

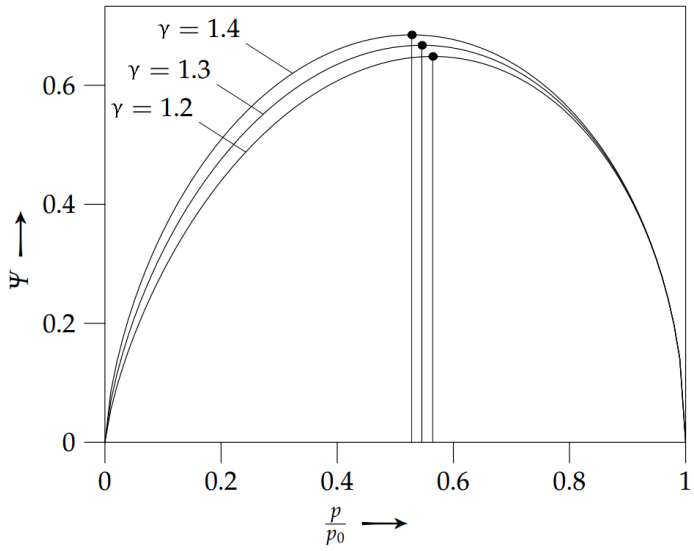

Figure 2.26: Flow Function Ψ [19]

$$\Psi = \sqrt{\frac{2\gamma}{\gamma-1}\left[\left(\frac{p}{p_0}\right)^{\frac{2}{\gamma}} - \left(\frac{p}{p_0}\right)^{\frac{\gamma+1}{\gamma}}\right]} \tag{2.11}$$

$$\left(\frac{p}{p_0}\right)_{crit,\gamma=1.4} = 0,5283 \tag{2.12}$$

$$\Psi = \left(\frac{2}{\gamma+1}\right)^{\frac{1}{\gamma-1}} \sqrt{\frac{2\gamma}{\gamma-1}} \quad \text{for} \quad \frac{p}{p_0} \leq \left(\frac{p}{p_0}\right)_{crit} \tag{2.13}$$

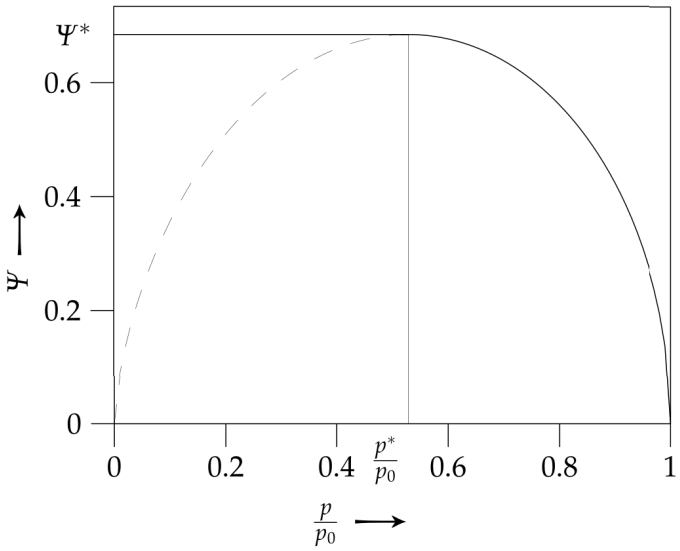

Figure 2.27: Corrected Flow Function Ψ for $\gamma = 1.4$ and Mach Number [19]

At the critical conditions, the pressure inside the fluid jet leaving the nozzle can't decrease below critical pressure, the jet has to expand behind the nozzle which leads to widening of the jet as presented in Figures 2.28 and 2.29. After the rapid expansion the pressure inside the jet drops below the ambient pressure which forces the jet to contract. The series of expansions and contractions is repeated until pressure equilibrium is reached with the ambient pressure.

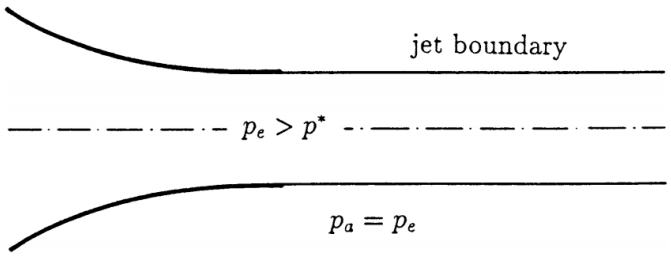

Figure 2.28: Subsonic Nozzle And Subsonic Jet [58]

2.2.3 Sudden Restriction in Flow Path

The majority of the seals work by introducing one or more sudden restrictions which compared to the ideal nozzle flow add viscous effects dissipating kinetic energy and reducing mass flow rate. In the case of a single restriction and assuming ideal flow, the mass flow rate can be calculated using equation (2.14) with flow function Ψ as

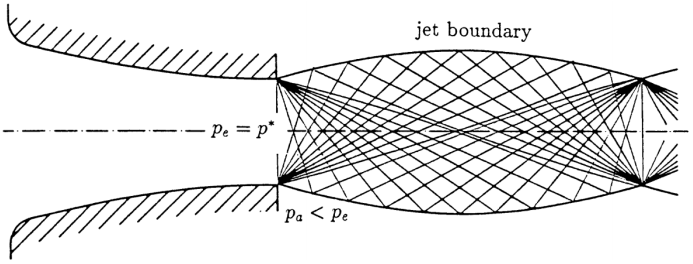

Figure 2.29: Subsonic Nozzle With After-Expansion In The Jet [58]

introduced above, A is the clearance area underneath the restriction and ρ is the fluid density.

$$\dot{m} = A \cdot \Psi \cdot \sqrt{p_0 \rho_0} \tag{2.14}$$

For real (non-ideal) flows equation (2.14) is amended by coefficients and factors to account for real gas effects. These corrections are introduced below.

2.2.4 Discharge Coefficient

The discharge Coefficient (2.15) is the dimensionless ratio of ideal or theoretical mass flow rate through a constriction or seal compared to actual mass flow rate.

$$C_d = \frac{\dot{m}}{\dot{m}_{ideal}} \tag{2.15}$$

The theoretical mass flow rate is calculated using equation (2.14). The actual mass flow rate depends on contraction coefficient $\tilde{\alpha}$, a ratio of geometrical opening size over actual contracted jet size and friction factor ϕ. So the discharge coefficient can be expressed as equation (2.16).

$$C_d = \tilde{\alpha} \cdot \phi \tag{2.16}$$

2.2.5 Contraction Coefficient

Compared to the ideal nozzle the flow through a constriction with sharp edges, such as an orifice plate or labyrinth fin, separates on the tip of the corner, which results in a contraction of the jet, hence a smaller effective area of the jet compared to the true clearance area, as shown in Figure 2.30. The Contraction Coefficient $\tilde{\alpha}$ is the

ratio of contracted jet area to the geometrical opening (2.17). For a labyrinth seal the contraction effect is a positive effect, since the aim is to reduce mass flow rate which is directly related to the effective jet area.

$$\tilde{\alpha} = \frac{A^{\star}}{A_2} \tag{2.17}$$

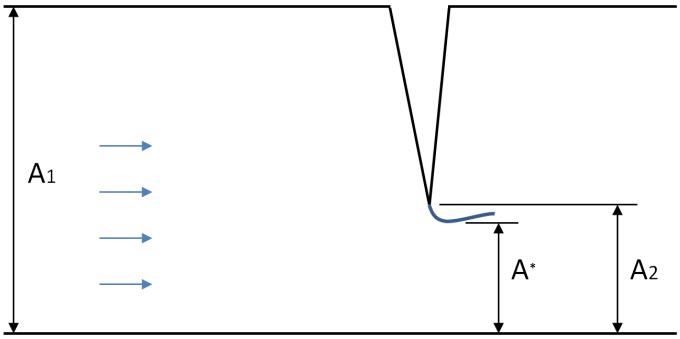

Figure 2.30: Jet Contraction After Separation on a Sharp Edge

2.2.6 Friction Factor

Friction Factor ϕ is introduced to take into account any flow effects due to friction . Friction Factor (2.20) is defined as ratio of fluid velocity (2.18) to the isentropic fluid velocity (2.19), or alternatively the square root of the isentropic efficiency η_s.

$$v = \sqrt{2\,(h_0 - h)} \tag{2.18}$$

$$v_s = \sqrt{2\,(h_0 - h_s)} \tag{2.19}$$

$$\phi = \frac{\sqrt{2\,(h_0 - h)}}{\sqrt{2\,(h_0 - h_s)}} = \sqrt{\eta_s} \quad \text{with} \quad \eta_s = \frac{h_0 - h}{h_0 - h_s} \tag{2.20}$$

2.2.7 Kinetic Energy Carry-Over Factor

In an ideal seal the kinetic energy of the jet passing underneath a restriction is dissipated into viscous heat energy in the following cavity. In a real seal,there is a risk that some of the kinetic energy of the leakage jet impinges on the opening under the next restriction resulting in some of the energy being carried over into the following

cavity. Different workers have attempted to specify a carry-over factor μ, based on the geometry of the seal, as described in following sections.

2.2.8 Flow Through a Series of Constrictions

Usually, a seal in turbomachinery consists of multiple successive labyrinth restrictions. Assuming a see-through labyrinth seal, as shown in Figure 2.31, the mass flow rate can be calculated by examining the flow function Ψ for each restriction. Here, capital Ψ represents the flow function through the whole seal, whereas the lower case ψ denotes the flow function through a single restriction.

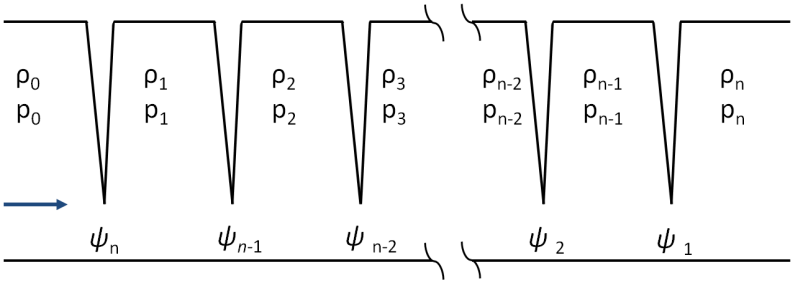

Figure 2.31: Generic See-Through Labyrinth Seal

The mass flow rate through each of the restrictions of the seal must be identical, so for each restriction, the mass flow equation (2.14) can be written as shown in (2.21) .

$$\dot{m} = A \cdot \psi_n \cdot \sqrt{p_0 \rho_0} = A \cdot \psi_{n-1} \cdot \sqrt{p_1 \rho_1} = ... = A \cdot \psi_1 \cdot \sqrt{p_{n-1} \rho_{n-1}} \tag{2.21}$$

Now assuming that the areas of all of the restrictions are the same ($A_1 = A_2 = ... = An$) and that the flow is isothermal ($p \cdot \upsilon = const$), equation (2.22) results.

$$\psi_{n-1} = \psi_n \frac{1}{\frac{p_1}{p_0}}; \psi_{n-2} = \psi_{n-1} \frac{1}{\frac{p_2}{p_1}}; ...; \psi_1 = \psi_2 \frac{1}{\frac{p_{n-1}}{p_{n-2}}} \tag{2.22}$$

From equations (2.22) it then follows that:

$$\psi_1 = \psi_n \frac{1}{\frac{p_{n-1}}{p_0}} \tag{2.23}$$

Combining equation (2.23) with equation (2.21) leads to equation (2.24). Further, replacing ψ with the expression in equation (2.11) results in equation (2.25), which is highly dependent on the flow through the last restriction of the seal.

$$\dot{m} = A \cdot \psi_n \cdot \sqrt{p_0 \cdot \rho_0} = A \cdot \frac{p_{n-1}}{p_0} \cdot \psi_1 \cdot \sqrt{p_0 \cdot \rho_0} \tag{2.24}$$

$$\dot{m} = \frac{A}{\sqrt{\tilde{R} \cdot T_0}} \cdot p_{n-1} \cdot \sqrt{\frac{2\gamma}{\gamma - 1} \cdot \left[\left(\frac{p_n}{p_{n-1}} \right)^{\frac{2}{\gamma}} - \left(\frac{p_n}{p_{n-1}} \right)^{\frac{\gamma+1}{\gamma}} \right]} \tag{2.25}$$

The major unknown in the equation above is the pressure inside last cavity which has to be calculated iteratively.

2.2.9 St. Venant - Wantzel Equation - Flow Through a Single Restriction

Saint-Venant and Wantzel, as summarised by Vennard [68], derived the equation (2.30) in 1839 based on even earlier work by Torricelli. The St. Venant-Wantzel equation can be derived from Bernoulli Equation (2.26) in its stationary and compressible form, applied along a streamline (Figure 2.32) as shown by Vennard [68]. With isentropic relation (2.9) and assumption of neglectable height change the Bernoulli Equation is integrated between inlet and restriction conditions into equation (2.27). The St.Venant-Wantzel Equation is based on the assumption of isentropic flow conditions (equation 2.23) and it is also assumed that potential energy effects and kinetic energy anywhere other than through the seal restrictions are negligible. The equitation is given in its velocity form (2.28). Substituting this equation into the mass flow continuity equation (2.29) gives the mass flow leakage rate version of the St. Venant-Wantzel Equation (2.30). This relatively simple equation has to be used with care as it assumes complete kinetic energy dissipation into heat energy without pressure gain in following cavity.

$$\int_1^2 \frac{\mathrm{d}p}{\rho(p)} + \int_1^2 v \mathrm{d}v + \int_1^2 g \mathrm{d}z = const \tag{2.26}$$

$$\frac{v_2^2 - v_1^2}{2} - \frac{p_1}{\rho_1} \cdot \frac{\gamma}{\gamma - 1} + \frac{p_1}{\rho_1} \cdot \frac{\gamma}{\gamma - 1} \cdot \left(\frac{p_2}{p_1} \right)^{\frac{\gamma-1}{\gamma}} = const \tag{2.27}$$

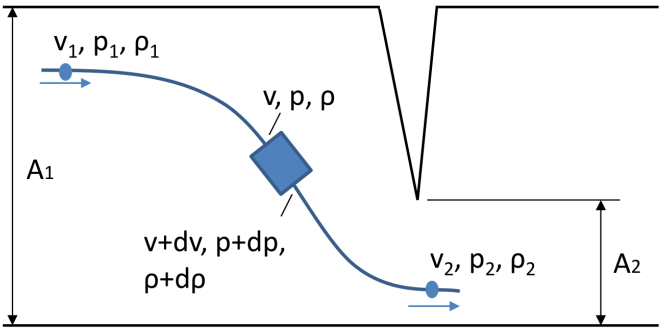

Figure 2.32: Energy Ballance On Differential Fluid Element Along A Streamline

$$v_2 = \sqrt{\frac{p_1}{\rho_1} \cdot \frac{2 \cdot \gamma}{\gamma - 1} \cdot \left[1 - \left(\frac{p_2}{p_1}\right)^{\frac{\gamma-1}{\gamma}}\right]} \tag{2.28}$$

$$\dot{m} = \rho \cdot A \cdot v \tag{2.29}$$

$$\dot{m}_1 = \dot{m}_2 = \frac{p_1 \cdot A_2}{\sqrt{\tilde{R} \cdot T_1}} \cdot \sqrt{\frac{2 \cdot \gamma}{\gamma - 1} \cdot \left[1 - \left(\frac{p_2}{p_1}\right)^{\frac{\gamma-1}{\gamma}}\right]} \tag{2.30}$$

2.2.10 Martin Equation - Multiple Restrictions

Martin [40] presented his leakage equation (2.31) for labyrinth seals 1908. His approach was purely analytical offering a single step method to calculate the leakage flow rate through the complete labyrinth of sealing fins. In his work, Gamal [19] described Martins approach as: "... determining the number of blades required to achieve a given pressure drop, then relating that number to the work done in dropping the pressure. The work done is then related to the flow rate through the kinetic energy of the fluid."

$$\dot{m} = \frac{p_{in} \cdot A_{sp}}{\sqrt{\tilde{R} \cdot T}} \cdot \sqrt{\frac{1 - \left(\frac{p_{out}}{p_{in}}\right)^2}{n - \ln\left(\frac{p_{out}}{p_{in}}\right)}} \tag{2.31}$$

Martins Equation assumes compressible flow with relatively small pressure change across each restriction-cavity arrangement which allows incompressible assumption to be used. Further, he assumes isothermal change of fluid conditions and subcritical

fluid velocity through the labyrinth. Since Martin's approach was designed purely analytically without validation against experimental results, his equation does not take into account kinetic carry over effects.

2.2.11 Neumann Equation - Multiple Restrictions

Neumann discovered in his experimental work that only a part of the kinetic energy of the fluid through a restriction is dissipated in the following cavity [10]. The remaining part of the kinetic energy, ε, is passed on into the following restriction-cavity arrangement (2.32). The ε-coefficient (2.33) is dependent on the geometry of the restriction-cavity arrangement and could vary between 0 and 1 with $\varepsilon = 0$ complete dissipation and $\varepsilon = 1$ total pass over of the kinetic energy. Further Neumann introduced a semi-empirical flow coefficient Cf (2.34) based on Chaplyn's Equation to account for jet contraction [62].

$$\dot{m}_i = Cf_i \cdot A_i \cdot \mu_i \cdot \sqrt{\frac{p_{i-1}^2 - p_i^2}{\tilde{R}T}} \tag{2.32}$$

$$\mu_i = \sqrt{\frac{n}{n \cdot (1 - \varepsilon_i) + \varepsilon_i}} \quad \text{with} \quad \varepsilon_i = \frac{1}{1 + 16.6 \cdot \left(\frac{H_i}{L_i}\right)} \tag{2.33}$$

$$Cf_i = \frac{\pi}{\pi + 2 - 5\beta_i + 2\beta_i^2} \quad \text{with} \quad \beta_i = \left(\frac{p_{i-1}}{p_i}\right)^{\frac{\gamma-1}{\gamma}} - 1 \quad \text{for} \quad i = 1...n \tag{2.34}$$

2.2.12 Derivatives of St.Venant, Martin and Neumann Equations

A number of researchers among others, Egli [18], Hodkinson [33], Vermes [69], Zimmerman and Wolff [72] have attempted to correct Martins (2.31), St.Venant [68] and Neumann's [10] equations by introducing empirical or semi-empirical kinetic energy carry over coefficients and flow correction factors.

Based on Eglis [18] work, Equation 2.35, Hodkinson [33] developed a semi-empirical coefficient, Equation 2.36, based on an assumption that the jet exiting a restriction created by a labyrinth fin is expanding conically into the following cavity as shown in Figure 2.33. With part of the kinetic energy being dissipated and the rest being

carried into next restriction. Hodkinson also noted that if the restrictions generated by the labyrinth fins are too wide, the jet would pass underneath and the seal would than act as one with just a single restriction. Additionally, he also noted that at seal conditions approaching critical conditions, the leakage is defined by the last restriction.

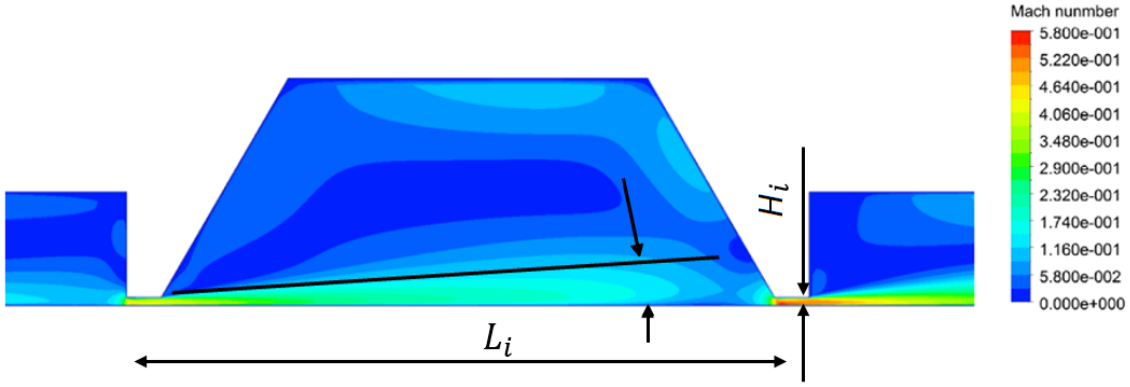

Figure 2.33: Conical Jet Expansion After a Tight Restriction Formed Between a Labyrinth Fin Tip and Rotor Shroud Surface

$$\dot{m} = \mu_i \cdot \frac{p_{in} \cdot A_{sp}}{\sqrt{\tilde{R} \cdot T}} \cdot \sqrt{\frac{1 - \left(\frac{p_{out}}{p_{in}}\right)^2}{n - \ln\left(\frac{p_{out}}{p_{in}}\right)}} \tag{2.35}$$

with

$$\mu_i = \sqrt{\frac{1}{1 - \left(\frac{n-1}{n}\right) \cdot \left(\frac{H_i/L_i}{(H_i/L_i)+0.02}\right)}} \tag{2.36}$$

2.3 Summary

A selection of a conventional rotating seal designs have been presented, starting with non-contacting seal designs such as labyrinth seals through to contacting seals, which are designed to have an interference fit with the rotor, such as brush and leaf seals. Strengths and weaknesses have been discussed, as well as the performance differences. Brush and finger seals were found to be able to reduce leakage flow rates up to 90% of a corresponding labyrinth seal design. Further, previous research on fluidic seals

have been reviewed revealing a limited amount of publications in this area. The majority of ideas on fluid sealing are published in form of patents, with only few actual performance evaluations and comparisons to conventional seals. In recent years some studies have been conducted by Curtis et al. [14], Hogg and Ruiz [34] and Auld et al. [5]and Hilfer et al. [31] including, showing improvements which can be made by incorporating fluidic sealing with conventional seal designs. Previously published models for prediction the leakage flow through labyrinth seals have been reviewed and discussed.

Having illustrated the potential of fluidic sealing and the previous analytical work the next chapter describes the seal concept development in this thesis.

Chapter 3

Fluidic Seal Concept Developed During this Study and its Experimental Validation

3.1 Fluidic Seal Concept

Much of the recent research in turbine sealing has focused on developing new types of contacting seal designs such as brush seals, leaf seals etc. These types of seal aim to achieve much lower leakage flow than a labyrinth seal for the same nominal clearance, by employing some form of deformable physical barrier to flow (i.e. a flexible bristle pack in the case of brush seals), that can conform to rotor excursions during operation. Physical barriers are particularly vulnerable to wear during transient operation as well as particle impact damage and therefore are limited in possible turbo-machinery applications due to the challenge of achieving acceptable design life.

Fluidic (or fluid-curtain) seals have been recognized for some decades to have the potential for development as high performance turbine seals, and they are now starting to receive some research attention. Fluidic seals employ aerodynamic flow features to create blockage/loss and reduce leakage, rather than relying on physical barriers to flow such as brush seal bristle packs etc. They are therefore potentially much more robust than many other types of advanced new turbine seal.

3.1.1 Fundamental Concept of Fluidic Sealing

In principal, a fluidic seal is an additional fluid supply introduced into a leakage channel to create a cross-flow that generates primary blockage in the form of a fluid

jet curtain as shown schematically in Figure 3.1.

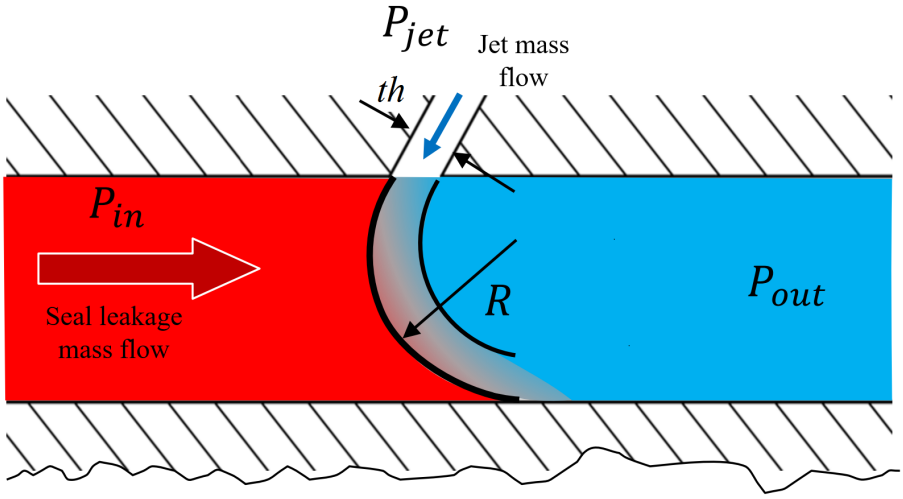

Figure 3.1: Idealized Jet in a Cross-Flow with Red Arrow Indicating Leakage flow Direction and the Blue Arrow the Fluidic Jet Flow Direction

In order to turn the momentum of the jet flow towards the direction of the main leakage flow, a static pressure drop across the curtain has to be present. The difference in pressure varies dependent on the radius R of the turning of the jet as well as the momentum or the energy of the jet as shown in the simplified Equation 3.1 for thin jets which is derived later in this chapter. Equation 3.1 uses some simplifying assumptions for example, widening of the jet, which will initiate immediately after it enters the cross-flow, is neglected, as well as the assumption of a circular turning path of the jet, which in a real flow will have a parabolic characteristic. Further, a constant gradient velocity distribution on the exit of the jet is assumed.

$$p_{in} - p_{out} = \frac{\rho {v_{jet}}^2}{2} \cdot \left[\frac{R^2}{(R - th)^2} - 1 \right] \tag{3.1}$$

Equation 3.1 shows that, at constant jet momentum, the pressure drop across the jet curtain increases with decreasing turning radius R, with constant turning radius the pressure drop increases with increasing momentum of the jet. This simple consideration is important for an optimal fluidic seal design.

The current work shows that Fluid-curtains can be used in combination with other types of aerodynamic seal to achieve performance gains in excess of those reported by Curtis et al [14]. This is based on the realisation that it is often more beneficial

to design the fluid-curtain to reduce the pressure drop across (and therefore leakage flow through) an auxiliary sealing element, rather than to design the fluid-curtain as the principal seal feature causing blockage to oppose leakage flow.

3.1.2 Definition of Pressure Ratio PR

A pressure ratio coefficient PR is used consistently throughout this work when defining the operating conditions for fluidic seals. PR is the difference between the total pressure of the jet supply fluid p_{0jet} and the exit static pressure p_{out} after leakage flow has mixed out downstream, divided by the total to static pressure drop across the leakage channel $p_{0in} - p_{out}$, as defined in Equation 3.2.

$$PR = \frac{p_{0jet} - p_{out}}{p_{0in} - p_{out}} \tag{3.2}$$

Figure 3.2 shows the flow through an idealised leakage channel that features an inclined jet with some downstream (II) and upstream (I) restrictions, where for constant leakage channel pressure drop $p_{0in} - p_{out}$, increasing pressure ratio PR means an increase in jet supply total pressure p_{0jet}.

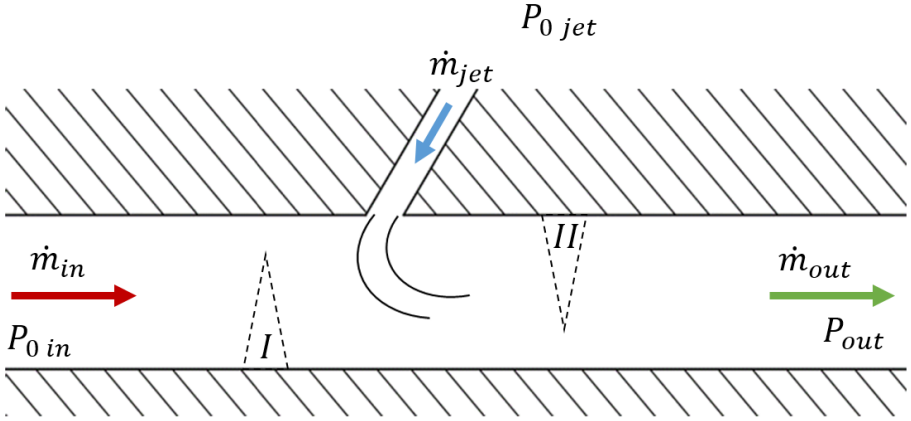

Figure 3.2: Idealized Fluidic Jet Seal

3.1.3 Leakage Mass Flow Rate Evaluation

Compared with other seal designs the fluidic type seal has a clear trade-off because some flow which could otherwise be expanded through the turbine blades to produce useful shaft work has to be taken from upstream of the seal to form the fluid curtain

$\dot{m}_j$. In gas turbine applications the impact can be reduced by using existing cooling flows to form the fluid curtain. The results by Curtis et al [14] as well as results presented in this work show conclusively that net overall leakage reduction (jet curtain flow $\dot{m}_j$ plus leakage inlet flow $\dot{m}_{in}$) can be achieved relative to the baseline leakage flow without a jet or curtain present. In Figure 3.2 $\dot{m}_{jet}$, $\dot{m}_{in}$ and $\dot{m}_{out}$ are shown. During the seal optimisation process a reduction of leakage path outlet mass flow rate $\dot{m}_{out}$ is the principal aim (3.3).

$$\dot{m}_{out} = \dot{m}_{in} + \dot{m}_{jet} \tag{3.3}$$

3.1.4 Kinetic Energy Carry Over Considerations

The kinetic energy carry over can be defined as the portion of the undissipated kinetic energy of the fluid transmitted from a seal restriction past the following restrictions and into the next cavity. In a labyrinth seal the kinetic energy carry over was recognized as a factor contributing to the reduction of the seal efficiency and was accounted for in the methods by Neumann [10], Hodkinson [33] and others by a carry over coefficient in the seal leakage flow rate calculation, Section 2.2.11. In a fluidic seal, the jet and leakage flow mixing immediately after the seal jet is injected and turned into the direction of the leakage flow can result in a jet of fluid with high kinetic energy approaching the first downstream restriction (see Figure 3.2). Furthermore, for any fixed pressure drop along the leakage channel ($p_{0in} - p_{out}$), the kinetic energy or dynamic pressure of the jet flow will increase with PR according to the Equation 3.4.

$$p_{dyn,jet} = p_{0jet} - p_{out,jet} = \frac{1}{2}\rho v^2 \tag{3.4}$$

In a fluidic seal assembly with a downstream restriction such as, for example one, or more labyrinth fins, as shown in Figure 3.3, the kinetic energy carry over from the fluid jet has to be considered.

In order to reduce the negative impact of the kinetic energy carry over into the downstream restrictions the fluidic seal geometry can be modified by introducing a kinetic energy stopper or blocker, (IIIa) and (IIIb) in Figure 3.3, with a distance

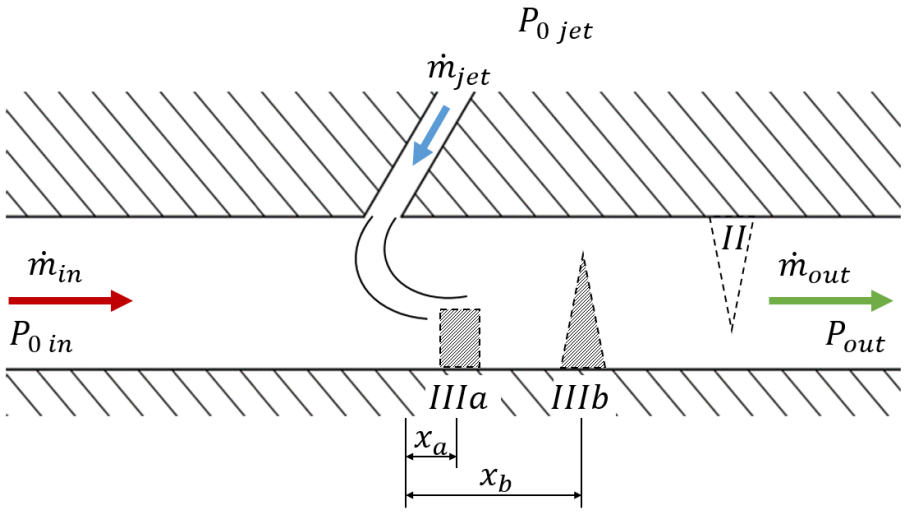

Figure 3.3: Idealized Fluidic Jet Seal with Kinetic Energy Blocker and Downstream Restriction

(x_a, x_b) downstream of the location of the jet curtain on the opposing wall. The main functions of the kinetic energy blocker are:

- Deflection of the jet away from impinging directly on the clearance underneath the following restriction.
- Increase of the travel of the jet increasing the time available to dissipate the jet kinetic energy and to ensure a greater spreading of the jet before it starts to interact with the following restriction.
- Interaction with the blocker itself changes the pressure field creating additional losses and increased dissipation of the kinetic energy.

3.1.5 Fluidic Seal Modes

Three different modes of seal flow can be observed during operation of fluid curtain seals, depending on conditions of the jet after it has turned into the leakage flow direction. As previously described the characteristics of the jet seal are dependent on the seal pressure ratio PR .

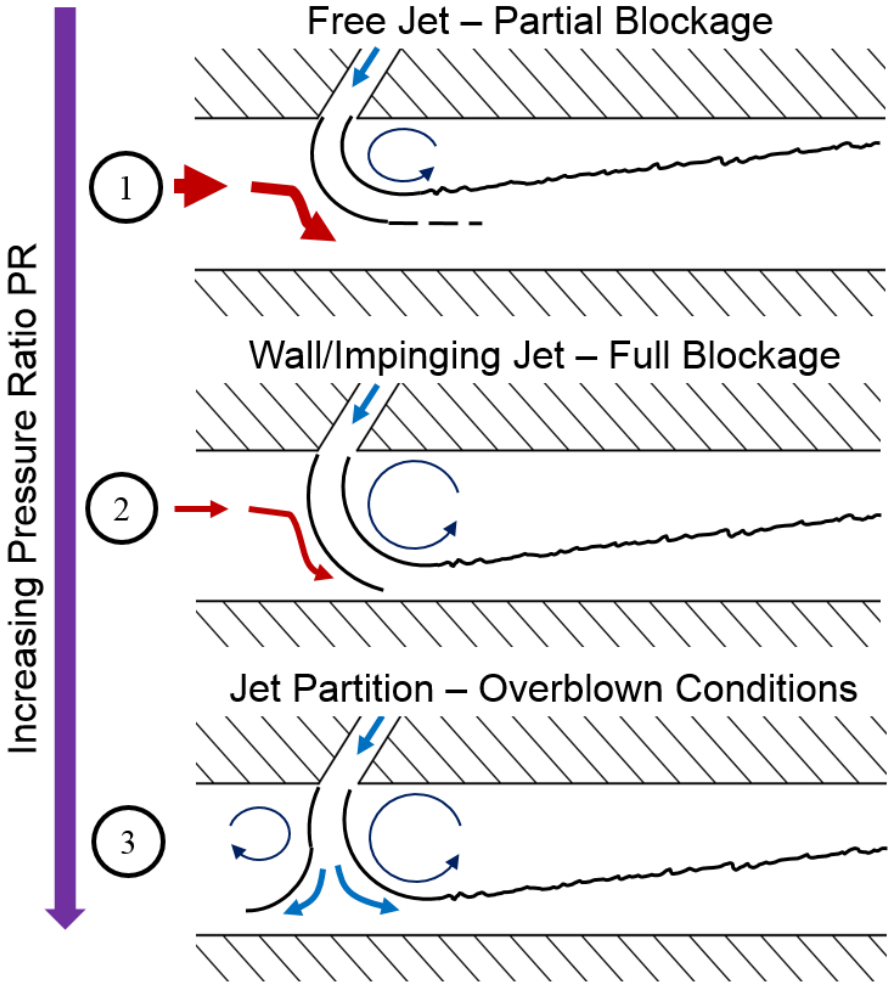

Figure 3.4: Modes of Operation: (1) Free Jet in Cross-Flow, (2) Impinging Jet, (3) Over-Blown Conditions

3.1.5.1 Mode (1): Free Jet in Cross-flow

As shown in Figure 3.4(1), the free jet is formed when jet pressure ratio PR is not sufficient for the fluid jet to cross the entire leakage channel hight, before it is turned creating a free jet condition in the wake. In this case, the seal inlet flow is diverted underneath the partial blockage of the jet as well as being incorporated into the jet by entrainment due to turbulent mixing. Turbulent mixing is an important part of interaction between jet and cross flow, contributing to spread and decay of the jet as well as the actual shape of the bending of the jet. As pressure ratio PR increases the blockage effected of the jet flow increases and the effect of the entrainment be-

comes more dominant due to increase in jet velocity and decrease of the throat area underneath the jet. The entrainment effect is described further in Section 3.1.6.

Similarly to labyrinth seals, the accelerated flow in the gap between the jet and the wall creates a high kinetic energy flow, which has to be dissipated. A kinetic energy blocker or stopper can be employed to do this as described in Section 3.1.4. The variable radial position of the free jet for mode (1) depending upon pressure ratio PR, makes positioning an effective blocker difficult.

3.1.5.2 Mode (2): Impinging Jet in Cross-flow

At higher pressure ratios the jet crosses the full channel and impinges on the opposite wall, resulting in a wall-jet in the wake, Figure 3.4(2). For an impinging jet, the blockage of the leakage path is maximised with the majority of the leakage flow combining with the jet flow through entrainment. As described in Section 3.1.4, a kinetic energy blocker should be employed so that during mode (2), the jet is increasingly deflected by the kinetic energy blocker leading to an increase in distance the jet has to travel, increasing the dissipation of the kinetic energy, before the flow gets to the next downstream restriction.

3.1.5.3 Mode (3): Over-Blown Fluidic Jet Seal

If the pressure ratio is increased still further, the momentum of the leakage flow is not sufficient to turn all of the jet flow resulting in a reversing of the leakage flow in leakage channel inlet region. This is identified as mode (3) in Figure 3.4. In this thesis, mode (3) is also referred to as the 'overblown' seal condition.

3.1.6 Entrainment

As introduced in Section 3.1.5 entrainment contributes to the leakage flow transport in a fluidic seal system and has to be taken into account. Entrainment is the incorporation of leakage fluid into the jet flow. Entrainment is a highly complex flow phenomena with many factors contributing to the process and consequently the entrainment rate, describing how fast the surrounding fluid is mixed into the jet flow. A large amount of work has been undertaken in recent decades to quantify entrainment rates of jets such as that by Ricou and Spalding [53], who carried out experiments

to investigate the sensitivity of entrainment ratio to various parameters over a range of Reynolds numbers. They derived the empirical expression shown in Equation 3.5 from their study, where m is the streamwise mass flow rate of the jet, x is the distance from the jet origin along the jet, M is the excess momentum flux of the jet, ρ is the density of the surrounding fluid and K is the entrainment constant.

$$\frac{m}{x\sqrt{M\rho}} = K \tag{3.5}$$

A similar expression will be used to determine entrainment rate in the analytical model of the fluid curtain seal, that will be developed in the next section.

3.2 Analytical Model of a Fluid Curtain Seal

In an idealised fluidic seal, blockage is created by a jet of high momentum fluid, entering the flow at an angle α of between 0 and 90 degree relative to the direction of the leakage flow and in the opposite direction to it, as shown in Figure 3.5.

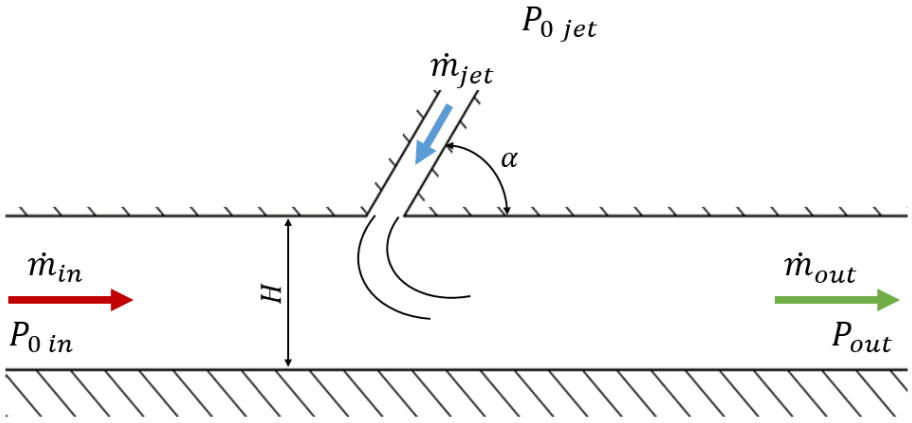

Figure 3.5: Idealized Fluidic Jet Seal: α = Jet Angle, H = Leakage Channel Hight

In principle, the high momentum fluid jet introduces a cross-flow, which creates a blockage. In order to turn the momentum of the jet flow into the direction of the main leakage flow, a static pressure drop is needed across the jet. This pressure drop acts to effectively reduce the pressure gradient in the inlet and outlet regions of the seal, thereby reducing the amount of leakage flow through the seal. This fundamental fluidic seal concept can be combined with essentially any other seal technology, including labyrinth seals, to enhance the performance of these seal types.

In the model developed in this study, a constant jet width and constant turning radius are assumed until the jet is turned parallel to the main seal flow in order to calculate the jet and seal mass flow rates through the basic fluidic seal. The jet experiences a transverse pressure gradient which causes a variation in velocity across the jet as shown in Figure 3.6. The Figure 3.6 shows a velocity magnitude contour plot from CFD calculations carried out as described in Section 3.5.

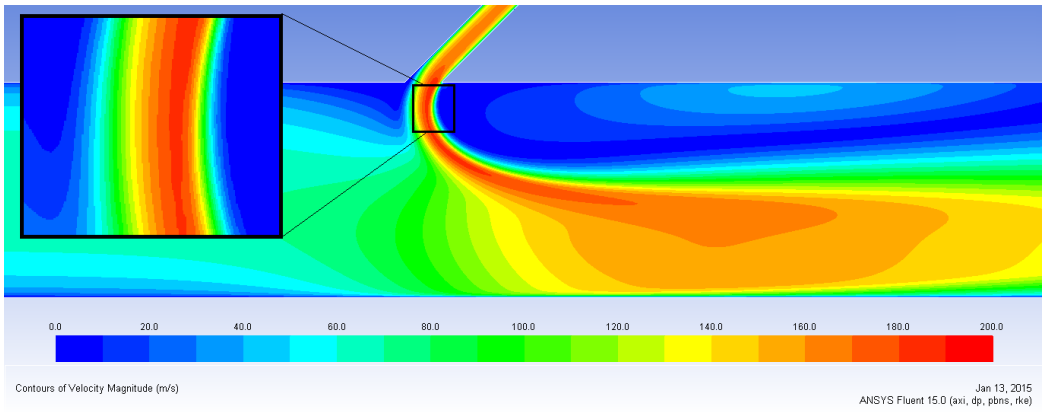

Figure 3.6: Plot of Velocity Magnitude in Basic Fluidic Jet Cross-Flow

The velocity distribution can be described as a potential free vortex according to Equation (3.6) as shown in Figure 3.7(b). The free vortex is selected for the model, due to its close representation of the velocity profile inside the jet curtain in radial direction, as shown in Figure 3.7(a). The match is not exact, since for the free vortex a velocity increase between inner and outer diameter is expected, whilst in the real flow, a decrease in velocity towards the edge of the jet is expected, due to viscous effects, as also shown in Figure 3.7(a).

$$v = \frac{(v_1 r_1)}{r} \tag{3.6}$$

where v_1 is the velocity at $r = r_1$.

Assuming steady, inviscid and incompressible flow Euler's equation can be used to described the relationship between the velocity and the pressure fields around a stream line. Neglecting the effect of conservative body forces the Euler equation can be written as in (3.7)

$$\vec{v} \cdot \nabla \vec{v} = -\frac{1}{\rho} \nabla p \tag{3.7}$$

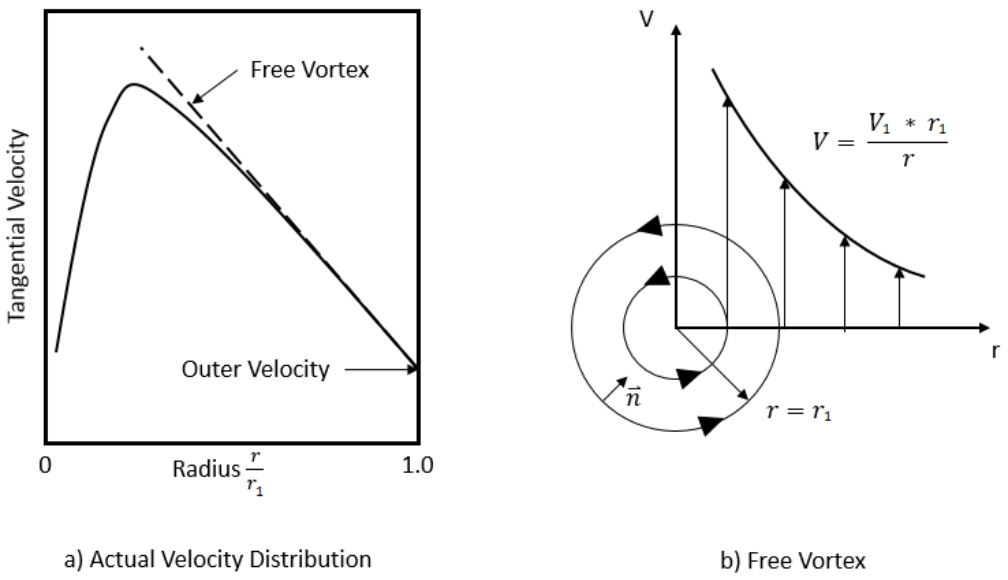

Figure 3.7: Free Vortex Tangential Velocity Distribution

Using stream line coordinates as shown in Figure 3.8 with $\hat{s}$ in flow direction, $\hat{n}$ normal to flow direction and $\hat{l} = \hat{s} \times \hat{n}$ the nabla operator is written

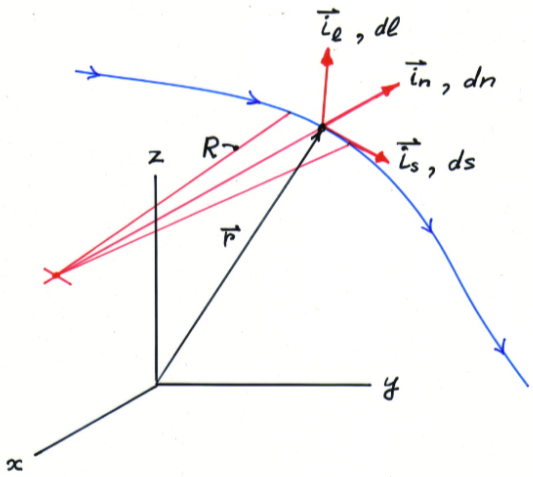

Figure 3.8: Stream Line Coordinates

$$\nabla = \hat{s}\frac{\partial}{\partial s} + \hat{n}\frac{\partial}{\partial n} + \hat{l}\frac{\partial}{\partial l} \tag{3.8}$$

which results in pressure gradient in streamline coordinate

$$\nabla p = \hat{s}\frac{\partial p}{\partial s} + \hat{n}\frac{\partial p}{\partial n} + \hat{l}\frac{\partial p}{\partial l} \tag{3.9}$$

As per definition, no flow can cross a streamline hence (3.10), where v is the magnitude of vector $\vec{v}$

$$\vec{v} = \hat{s}v \tag{3.10}$$

Combining (3.8) and (3.10) gives.

$$\vec{v} \cdot \nabla = v\frac{\partial}{\partial s} \tag{3.11}$$

Substituting (3.10) and (3.11) into (3.7) gives.

$$(\vec{v} \cdot \nabla)\,\vec{v} = v\frac{\partial}{\partial s}(v\hat{s}) = \hat{s}\frac{\partial}{\partial s}\left(\frac{v^2}{2}\right) + v^2\frac{\partial \hat{s}}{\partial s} \tag{3.12}$$

$d\hat{s}$ is the change in orientation along a streamline as shown in Figure 3.9 and described in Equation 3.19

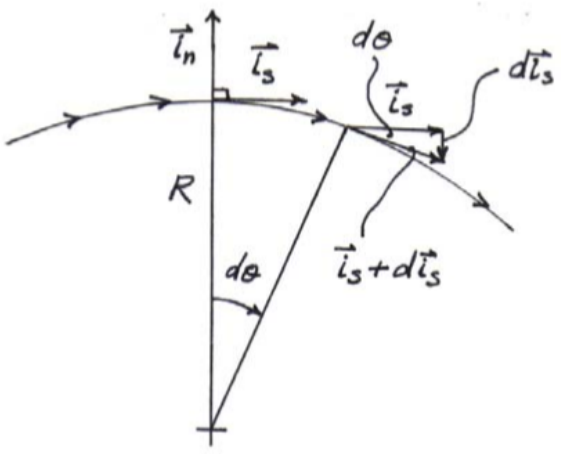

Figure 3.9: Stream Line Coordinates

$$d\hat{s} = -\hat{n}d\phi = -\hat{n}\frac{ds}{r} => \frac{\partial \hat{s}}{\partial s} = -\frac{\hat{n}}{r} \tag{3.13}$$

Substituting into Equation 3.12 leads to Equation 3.14 for convective acceleration

$$(\vec{v} \cdot \nabla)\,\vec{v} = \hat{s}\frac{\partial}{\partial s}\left(\frac{v^2}{2}\right) - \hat{n}\frac{v^2}{r} \tag{3.14}$$

Substituting Equation (3.14) and (3.9) into (3.7) equation and assuming two dimensional flow, results in the equation of motion in streamline coordinates for steady, invicid movement along the streamline

$$\frac{\partial}{\partial s}\left(\frac{v^2}{2}\right) = -\frac{1}{\rho}\frac{\partial p}{\partial s} \tag{3.15}$$

and in the perpendicular direction,

$$\frac{v^2}{r} = \frac{1}{\rho}\frac{\partial p}{\partial n} \tag{3.16}$$

Equation (3.16) can be rewritten for a free vortex system using

$$\partial n = \partial r \tag{3.17}$$

Giving Equation (3.18), the radial equilibrium equation for pressure inside a vortex flow,

$$\frac{\partial p}{\partial r} = \frac{\rho v^2}{r} \tag{3.18}$$

which can be integrated from r to r_1 to give Equation 3.19, where the pressure decreases as radius decreases since $\partial p/\partial r > 0$.

$$\Delta p_{jet} = p_1 - p = \frac{\rho {v_1}^2}{2}\left(1 - \left(\frac{r_1}{r}\right)^2\right) \tag{3.19}$$

In the equation 3.19 p_1 refers to the jet upstream static pressure, which is also the stagnation pressure in the stagnation region upstream of the jet inlet, as shown in Figure 3.6. The Equation 3.19 shows the direct relationship between the radius of the jet turning and the pressure difference across the jet as shown in Figure 3.10, where $\Delta p_I < \Delta p_{II}$.

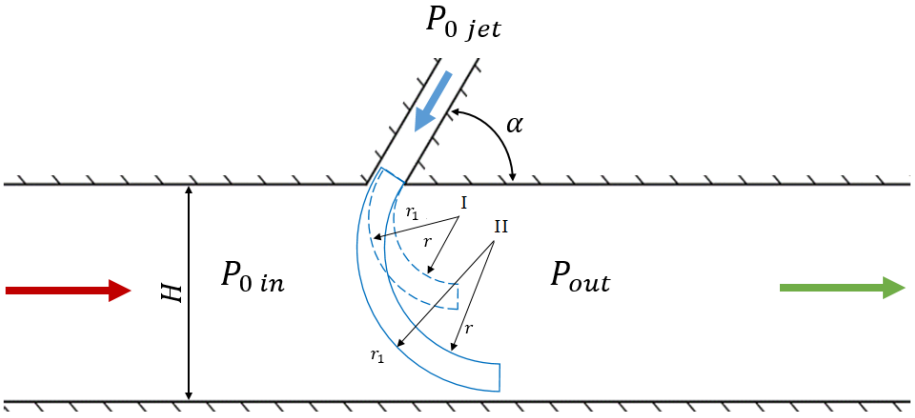

Figure 3.10: Jet Turning Radius Dependent on Pressure Difference

$$r = r_1 - th \tag{3.20}$$

The kinetic energy of the jet flow can be expressed in terms of the dynamic pressure for the jet according to Equation (3.21) .

$$p_{0jet} - p_1 = \frac{\rho {v_1}^2}{2} \tag{3.21}$$

Combining Equation (3.20), (3.21) and (3.19) gives Equation (3.22), which is used to relate the turning radius of the jet to the static pressure drop across it.

$$r_1 = \frac{th}{1 - \frac{1}{\sqrt{1 - \frac{\Delta p_{jet}}{p_{0jet} - p_1}}}} \tag{3.22}$$

3.2.1 Jet Mass Flow Rate Calculation

The mass flow rate of the jet can be calculated from continuity according to

$$\dot{m}_{jet} = A_{jet} \cdot \rho_{jet} \cdot v_{jet} \tag{3.23}$$

As was shown in Figure 3.6 and 3.7 for a free vortex, the velocity of the jet decreases from the jet inner radius r toward the outer radius r_1. The jet mass flow rate calculation is simplified in the current model by assuming that, the velocity distribution across the jet is linear, with the maximum velocity calculated from dynamic pressure on the inside radius r at static pressure p

$$p_{0jet} - p = \frac{1}{2}\rho_{jet} v^2 \tag{3.24}$$

and the minimum velocity on the outside radius r_1 at pressure p_1

$$p_{0jet} - p_1 = \frac{1}{2}\rho_{jet} {v_1}^2 \tag{3.25}$$

The jet area is calculated from Equation 3.26 for the frustum lateral surface area through which the jet issues, where D is the diameter of the housing.

$$A_{jet} = [2D + th \sin \alpha] \pi th \tag{3.26}$$

Combining Equation (3.23) , (3.24), (3.25) and (3.26) gives Equation (3.27), which is used to calculate jet mass flow rate .

$$\dot{m}_{jet} = \sqrt{\frac{(p_1 + p)}{\tilde{R}T_{jet}} \frac{1}{4}} \cdot [2D_H + th \sin\alpha] \pi th \cdot \left(\sqrt{p_{0jet} - p_1} + \sqrt{p_{0jet} - p}\right) \tag{3.27}$$

3.2.2 Leakage Inlet Mass Flow Rate

The leakage inlet mass flow rate is based on the calculation of the leakage flow through the restriction created by the fluidic jet and the calculation of the inlet flow incorporated into the fluidic jet by entrainment (for Mode 1). In a case the fluidic jet is impinging upon the opposing surface and therefor creating complete blockage of the leakage area (Mode 2), only the entrainment of the leakage fluid into the jet flow is calculated.

The current mode of operation is defined by:

- **Mode (1)** for $H > (r_1 - th)\cos\alpha + r_1$.
- **Mode (2)** for $H \cong (r_1 - th)\cos\alpha + r_1$.
- **Mode (3)** for $H < th(r_1 - th)\cos\alpha + r_1$.

Where H on the left side of the equations is the height of the leakage channel and the right side represents the hight of the leakage channel covered by the jet curtain.

3.2.2.1 Part 1 - Leakage Inlet Mass Flow Rate Through the Fluidic Jet Restriction

This model is used to calculate the seal leakage inlet mass flow rate through the restriction created by the fluidic jet, as shown in Figure 3.11 for the jet mode 1. The leakage inlet mass flow rate can be calculated using the continuity Equation similar to (3.23) and the jet downstream static pressure P_{out}, as shown in Figure 3.11. P_{out} is equal to the static pressure inside the 'Nozzle' flow created between the jet outer surface, defined by the radius r_1, and the surface of the shroud from the point, where the jet is turned to be parallel to the leakage flow as indicated by the broken line in Figure 3.11. The leakage inlet mass flow calculation described below applies only for the jet mode (1), where the jet is turned into the leakage flow direction building a

free jet in the wake. The position of the jet after turning and therefor the size of the 'Nozzle', can be calculated as shown in Figure 3.11 using α and Equation (3.22) to determine jet turning radius r_1.

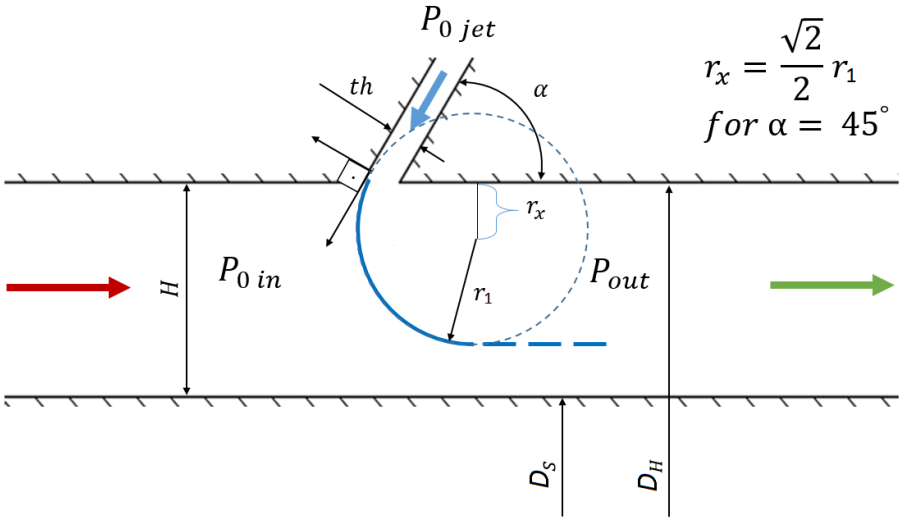

Figure 3.11: Jet Position After Turning

The vertical distance r_x (Figure 3.11) is calculated using the assumption that the jet leaves the jet slot tangential to the turning circle of its outer radius r_1. The maximum possible size of r_x is restricted by manufacturing constraints, but could reach theoretically $r_x = r_1 - th$ when the jet inlet angle reaches $\alpha = 0$.

$$r_x = (r_1 - th)\cos\alpha \tag{3.28}$$

The dynamic pressure inside the nozzle is

$$p_{0in} - p_{out} = p_{dyn} = \frac{1}{2}\rho v^2 \tag{3.29}$$

To calculate the seal flow rate a flow rate equation (3.30) is used.

$$\dot{m} = C_d A_{throat}\sqrt{2\rho(p_1 - p)} \tag{3.30}$$

With discharge coefficient $C_d = 0.8....1$ and throat area

$$A_{throat} = \frac{\pi}{4}(D_H - (r_1 + r_x))^2 - \frac{\pi}{4}(D_S)^2 \tag{3.31}$$

3.2.2.2 Part 2 - Entrainment Calculation

The entrainment of the surrounding fluid into the seal jet is approximated by treating it as with entrainment of fluid into a turbulent free planar jet. The jet is considered turbulent for Reynolds numbers higher than 3000, which is the case in a majority of the fluidic seal applications. Laminar jets only occur in the initial phase (low pressure ratios PR) and are not relevant for continuous seal operation. A large body of theoretical and experimental work is available in the literature describing entrainment in axisymmetric turbulent jets. Morton et al. [44] introduced in their work on axisymmetric turbulent jets a concept of entrainment coefficient, 'Gaussian' coefficient, αg, which is the ratio of lateral velocity of the fluid being incorporated into the flow, to the jet mean flow velocity. The 'Gaussian' entrainment coefficient was obtained from experimental data, where the jet velocity was measured and a Gaussian function fitted. The Gauss function can be fitted to the velocity distribution of a free jet in the fully developed flow zone (Figure 3.12), where the distance from the jet source $z/th > 4$ (z is the distance along the jet path and th the source width (Figure 3.13)).

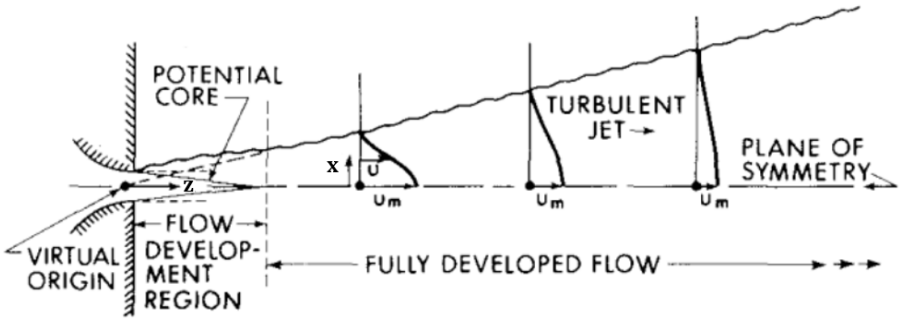

Figure 3.12: Free Turbulent Jet, Rajaratnam [52]

Planar turbulent jets, as noted by Paillat and Kaminski [48], have not been the subject of as many comprehensive studies. In their work Pailat and Kaminski [48] compared available experimental results for the 'Gaussian' entrainment coefficient αg for round and planar jets, concluding that for planar jet with Reynolds numbers up to 2000, the entrainment coefficient averages around $\alpha g \approx 0.072$. For jet Reynolds numbers beyond 3000, the entrainment coefficient reduces to $\alpha g \approx 0.035$ and remains close to this value at high Re.

Furthermore, no comprehensive literature could be found on planar turbulent jets injected into confined spaces (channels) with a strong cross flow present, so the entrainment calculation in this thesis is, as mentioned above, approximated with entrainment in a free planar jet with αg between 0.072 and 0.03. Further, since the jet surrounding fluid originates from the leakage path inlet, the entrained fluid is added to the inlet leakage flow rate $\dot{m}_{in}$ calculated in the Section 3.2.2.1 for mode 1. In case of mode 2, the calculated entrained fluid is equal to the leakage inlet flow.

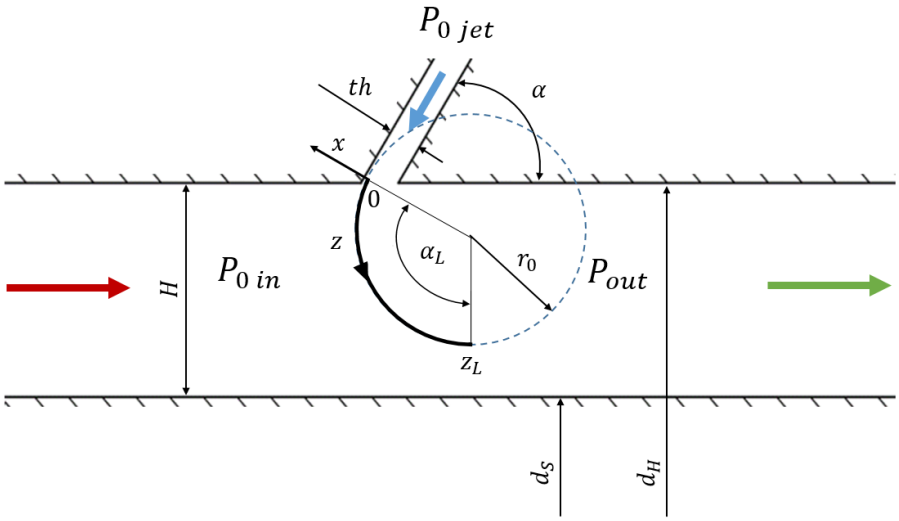

Figure 3.13: Jet Position after Turning

As shown in previous studies (Morton et al. [44] and others), the jet velocity distribution $v(x, z)$ in a planar jet is well described by a Gauss function at a distance from the jet source $z > 4th$. This function is widely used in the literature but does not fully represents the velocity profile of the jet in a cross flow, where the Gauss function is skewed to the inside radius of the deflected jet (Figure 3.7(a)), however the approximation is sufficiently accurate.

$$v(x, z) = v_m(z) e^{-\left(\frac{x}{b_m(z)}\right)^2} \tag{3.32}$$

where b_w is the $1/e$-width of the Gauss function and v_m is the maximum velocity on the jet axis. The mass and momentum conservation equation in a planar jet can be written as

$$\frac{d}{dz}(b_w v_m) = 2 \cdot \alpha g \cdot v_m \tag{3.33}$$

and

$$\frac{d}{dz}(b_w {v_m}^2) = 0 \tag{3.34}$$

and solved to

$$b_w = b_{w0} + 4\alpha g z \tag{3.35}$$

and

$$v_m = \frac{v_{m0}}{\sqrt{1 + 4\alpha g \frac{z}{b_{w0}}}} \tag{3.36}$$

where v_{m0} and b_{w0} are conditions at the jet origin ($z = 0$). The entrainment of the jet is calculated along the jet path up to the point where the jet is parallel to the leakage path flow z_L, Figure 3.13, with the arc length z_L defined by

$$r_1 \alpha_L = z_L \tag{3.37}$$

with

$$\alpha_L = \pi - \alpha \tag{3.38}$$

In order to calculate the jet volume flux $Q(z)$ per unit length the Gauss function is integrated as defined in Equation (3.39) where the integral is multiplied by 0.5 to calculate only the entrainment on the side facing incoming cross flow. Since any fluid entering the leakage path originates from the leakage path inlet and the jet inlet, the downstream side of the jet curtain is only incorporating the fluid from the leakage path inlet and the jet inlet and does not need to be taken into account.

$$Q(z) = \frac{1}{2} \int_{-\infty}^{+\infty} v(x, z) dx \tag{3.39}$$

With (3.32), (3.35) and (3.36) in (3.39) for $z = z_L$ we get

$$Q(z) = \frac{1}{2} \int_{-\infty}^{+\infty} \frac{v_{m0}}{\sqrt{1 + 4\alpha g \frac{z_L}{b_{w0}}}} e^{-\left(\frac{x}{b_{w0} + 4\alpha g z_L}\right)^2} dx \tag{3.40}$$

The amount of entrained fluid is the difference between the jet flow rate at the source $Q(z = 0)$ and the calculated jet volume flux $Q(z = z_L)$

$$Q_e = Q(z = z_L) - Q(z = 0) \tag{3.41}$$

To calculate the entrained fluid mass flow rate the volume flux is multiplied by the circumference of the leakage path and the fluid density.

$$\dot{m}_e = Q_e \cdot \rho \cdot \pi D_H \tag{3.42}$$

3.2.3 Mass Flow Rate Calculation Procedure

Figure 3.14 shows a flowchart, which illustrates the sequence of the steps used to calculate the mass flow rates through a fluidic seal assembly using the analytical model equations described in the previous sub-sections.

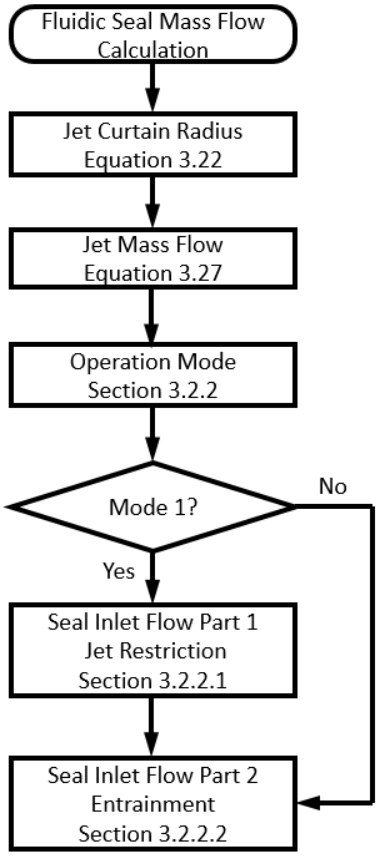

Figure 3.14: Fluidic Seal Mass Flow Calculation Flow Chart.

As shown in Figure 3.14, the first step is to calculate the turning radius of the jet curtain using the jet upstream and downstream pressures. Next, the jet mass flow is calculated using same jet upstream and downstream pressures. The fluidic seal mode of operation is then deduced by using the calculated jet turning radius. If the mode of operation is 1, then the seal inlet flow rate through the restriction created by the fluidic jet and subsequently the entrainment of the inlet flow into the jet are calculated. If the mode of operation is 2, then only the entrainment of the seal inlet flow into the jet is calculated, since the seal jet spans the entire leakage path and so none of the seal inlet flow is squeezed underneath the deflected jet in this operating mode.

These analytical models provide a simple description of the fluid flow in a fluidic seal and can be used for preliminary design work.

3.3 Experimental Validation of the Fluidic Seal Concept

In order to experimentally validate the fluidic seal concept described above, a new blow down test facility and seal concept demonstration test rig were constructed.

3.3.1 Durham Blow Down Test Facility

The Durham Blow Down Facility is a transient open flow facility, which requires a large upstream air receiver to be charged before each test. The receiver is charged from atmospheric air using a commercial compressor unit. During a test, compressed air from the receiver is expanded through a test section. The run time available for a test varies from few seconds to up to several minutes, depending upon the mass flow rate and operating pressure needed for the test.

Figure 3.15 shows a schematic diagram of the initial Durham Blow Down Facility configuration. As shown in Figure 3.15 a control valve throttles the flow to the test section to provide a constant operational pressure on the inlet of the test section. The maximum test time is achieved when the pressure in the air receiver reaches the pressure required at the inlet of the test section.

Upstream of the control valve, the blow down facility includes a fast response isolation valve, which was used to isolate the test section from the compressed air in

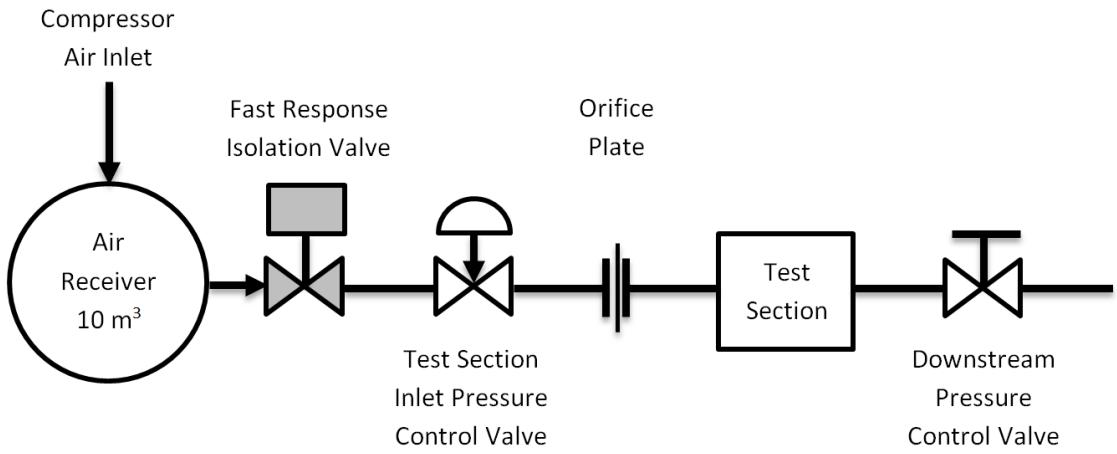

Figure 3.15: Sketch of the Initial Durham Blow Down Facility Configuration

the receiver immediately in case of malfunction or emergency. An orifice plate was situated downstream of the control valve, which is used to measure the overall mass flow rate of the air leaving the receiver. The test section is situated downstream of the orifice plate. Finally, a hand-operated valve is included on the exhaust side of the test section to control back pressure.

3.3.2 Durham Blow Down Test Facility Components and Controls

The hardware components below are common to all experiments.

- **The Air Receiver** has a volume of 10 m^3 and is rated up to a maximum pressure of 30 bar. The air receiver was connected to a compressor capable to deliver pressures up to 15 bar. At maximum pressure of 15 bar the receiver contained 175 kg of air.

- **The Fast Response Isolation Valve** can be actuated automatically in the case of an emergency stop, or can be switched manually for rapid start-up or shut-down. The isolation valve is also used in combination with the control valve to ensure double isolation (both valves closed) of the air receiver from the test section, when testing is not in progress.

- **The Test Section Inlet Control Valve** forms a control loop consisting of the valve, a pneumatic actuator, a PID Controller and a pressure sensor. The

pressure sensor is located directly downstream of the control valve and delivers a pressure signal to the PID Controller, which can be used to control to a specified pressure level and pressure ramp-up procedure.

- **The Orifice Plate** is custom made to ISO 5167-1:2003 and ISO 5167-1:2003 standards with Corner Taps and interchangeable plates. The selection of the plate size depends on the mass flow rate needed for a test. The orifice plate upstream and differential pressures are measured using the transducers described later and shown in Table 3.1.

3.3.3 Experimental Method

The following general procedure was used when performing tests, with any additional steps for specific test campaigns given in the chapters describing them.

- **Warming Up Procedure** was performed at least 30 minutes before every test, where all the electrical equipment was switched on and a health test of the measurement equipment was carried out.

- **Quick Pre-Calibration** was performed after the warming up procedure by evacuating all the pipes and components to ambient pressure and measuring and logging all the relevant signals. Then, the pipework and the test section were gradually pressurized to the operating conditions and the signals logged at intervals during the pressurisation. From the measured values, a table for later use as datums was compiled and used to correct the measurements from the test campaigns.

- **Test Campaign** was carried out after the quick pre-calibration, with up to 4096 measurements carried out for each operational point at a logging frequency of 800 Hz -1200 Hz. The data was logged and post-processed using Durham Software for Wind-tunnels and specialized scripts written in Matlab.

- **Quick Post Calibration** was carried out to ensure no damage to the measurement equipment was administered during test campaign. This was performed the same way as the pre-calibration.

3.3.4 Experiment Logging and Post-Processing Software

Durham Software for Wind-tunnels (DSW) was used to log all data and to carry out partial post-processing. DSW is a standard in-house software suite, which was designed to control and carry out measurements and post-processing on a variety of wind tunnels in the School of Engineering and Computing Sciences at Durham University. For the operation and measurement at Durham Blow Down Facility it was only partially suitable, even though it was used to carry out all but ScaniValve logging tasks, additional scripts had to be written to carry out major part of post-processing. The post processing scripts included a script to perform a datum correction from the datum table created during the quick pre-calibration and a script to iterate the mass flow rate calculation from the orifice plate measurements.

All the probe and transducer voltage outputs were connected to USB-6018 National Instruments data acquisition device which, with use of DSW, performed the logging and storage of the measured voltage data in a table for later post processing. In the case of the ScaniValve DSA3217 Pressure Scanner, the data was acquired and post processed and saved in form of engineering units.

3.3.5 Probes, Transducers and Error Analysis

The systematic error of the measurement system was corrected for by carefully calibration of the equipment, probes and transducers. Special attention was given to the calibration of the pressure probes and transducers in the reduced band of pressure levels, which were expected during each set of tests. For this purpose, a new high pressure calibration rig was developed with a set of standard high precision pre-calibrated analog gages, which were used to calibrate every transducer before each major test campaign. A high precision digital pressure transducer was also used to carry out quick calibration and verification checks during test campaigns. The calibration rig was operated with nitrogen and was also used to calibrate the ScaniValve DSA3217 Pressure Scanner.

3.3.5.1 Tank Temperature and Pressure

The pressure in the air receiver tank was measured using a Sensor Technics CTE 8016 pressure transducer with an uncertainty of 0.1% FSO. The temperature in the

receiver was measured using a T-type thermocouple probe with grounded junction and a class 1 tolerance of 0.4% uncertainty over the measured temperature range.

3.3.5.2 Orifice Plate

Custom made orifice plates were used to measure mass flow rates at up to 3 locations in the test facility. The orifice plates were designed to ISO 5167-1:2003 and ISO 5167-2:2003 standards and featured corner tapings situated in a corner groove as shown in Figure 3.16.

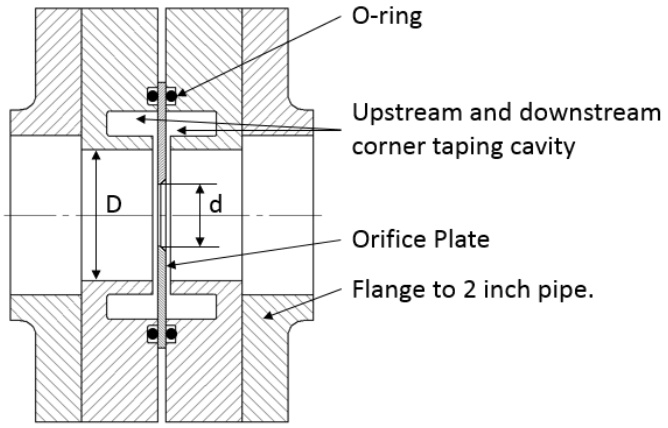

Figure 3.16: Custom Orifice Plate Assembly Featuring Corner Tapings.

Two pressure transducers were used on each of the orifice plates with a Spirax Sarco EL2600 pressure transmitter measuring the orifice plate upstream absolute pressure and a Sensor Technics BTE5002 measuring the differential pressure across the plate. The transducers specifications are given in Table 3.1. A K-type thermo couple was used to measure the orifice plate inlet temperature, which was then correlated to give the total temperature measured inside the pressurized air receiver (time constant of the thermocouple ¡ 0.1 seconds). For the duration of the measurement the flow through orifice plates is assumed to be steady.

The mass flow rate through the orifice plate was calculated using Equation 3.43 from ISO 5167-1:2003, where diameter ratio β is defined in Equation 3.44. A Matlab script was written to carry out the iterative calculation needed to determine the mass flow rate. The iteration process is also described in ISO ISO 5167-2:2003. In the ISO standard, the practical working Equation 3.45 for calculation of uncertainty of mass flow through orifice plate is given. The uncertainty in the mass flow rate

Table 3.1: Specifications of the Transducers Used for measuring Mass Flow Rates.

Spirax Sarco EL2600	
Pressure Range	0-16 bar
Accuracy	$\leq 0.5\%$
Compensated Temperature Range	$-30°C - 100°C$
SensorTechnics BTE5002	
Differential Pressure Range	0-2 bar
Accuracy	$\leq 0.2\%$
Compensated Temperature Range	$0°C - 70°C$

calculation was evaluated using Equation 3.45 to be between 1% and 1.8%, with the uncertainty increasing with decreasing mass flow rate. Smaller size orifice plates were used at low flow rate conditions, in order to increase the accuracy of the mass flow rate measurements at these flows.

$$\dot{m} = \frac{C}{\sqrt{1-\beta^4}} \epsilon \frac{\pi}{4} d^2 \sqrt{2\Delta p \rho_1} \tag{3.43}$$

$$\beta = \frac{d}{D} \tag{3.44}$$

$$\frac{\delta \dot{m}}{\dot{m}} = \sqrt{\left(\frac{\delta C}{C}\right)^2 + \left(\frac{\delta \epsilon}{\epsilon}\right)^2 + \left(\frac{2\beta^4}{1-\beta^4}\right)^2 \left(\frac{\delta D}{D}\right)^2 + \left(\frac{2}{1-\beta^4}\right)^2 \left(\frac{\delta d}{d}\right)^2 + \frac{1}{4}\left(\frac{\delta \Delta p}{\Delta p}\right)^2 + \frac{1}{4}\left(\frac{\delta \rho_1}{\rho_1}\right)^2} \tag{3.45}$$

3.3.5.3 ScaniValve DSA3217 for Pressure Measurements

The ScaniValve DSA3217 Pressure Scanner used in the tests featured 16 temperature compensated high accuracy transducers. It was used to measure pressures inside the test section. The ScaniValve also featured an automatic zero offset correction. Half of the transducers were calibrated for low pressure range between 0 bar - 8 bar and the other half for high pressure range of 0 bar - 16 bar, both ranges featuring a maximum of 0.05% uncertainty. Each of the transducers was independently calibrated by the manufacturer. Different ranges were used according to expected operational pressures inside the test section.

3.4 The Fluidic Seal Concept Demonstration Test Rig.

The static fluidic seal test facility was initially designed by Messenger [42] for testing of different fluidic seal configurations and later modified to accommodate the seal geometries introduced in this thesis. The operational conditions of the equipment could also be modified with variable inlet, outlet and jet pressures. The aim of the investigations described in the present section was to validate the concept of a fluidic seal, and to investigate the fundamental flow physics by experiment and numerical investigations to back up the results obtained from the analytical model described earlier. The test facility does not feature any rotating parts. It is assumed that the shaft rotation has neglectable effect on leakage mass flow rates in many types of turbomachinery seal.

3.4.1 Rig Components

The design of the test rig consisted of six cylindrical/annular steel components each with equal outer diameter, stacked axially as shown in Figure 3.17. Between the ring components, o-rings were used for sealing . The six concentric metal rings were held together by 12 threaded steel bars which were circumferentially uniformly spaced around the cylinder. An additional central metal tube was inserted to represent rotor shroud or the surface of a shaft. The fluidic seal insert components shown in Figure3.17 and Figure 3.18, were manufactured to produce a clearance of 1 mm between the shaft/shroud and the seal components forming the leakage channel. Later modifications were made to the fluidic seal components to accommodate various other seal designs, such as the labyrinth seal design shown in Figure 3.18. The design of the seal inserts ensured that the clamping force between jet seal components was independent of the operational pressures, and therefore a constant jet gap size could be maintained throughout the experiments.

In the configuration shown in Figure 3.18, the fluidic jet thickness/clearance between part 1 and part 2 was controlled by placing shims between part 2 and part 3 of the assembly.

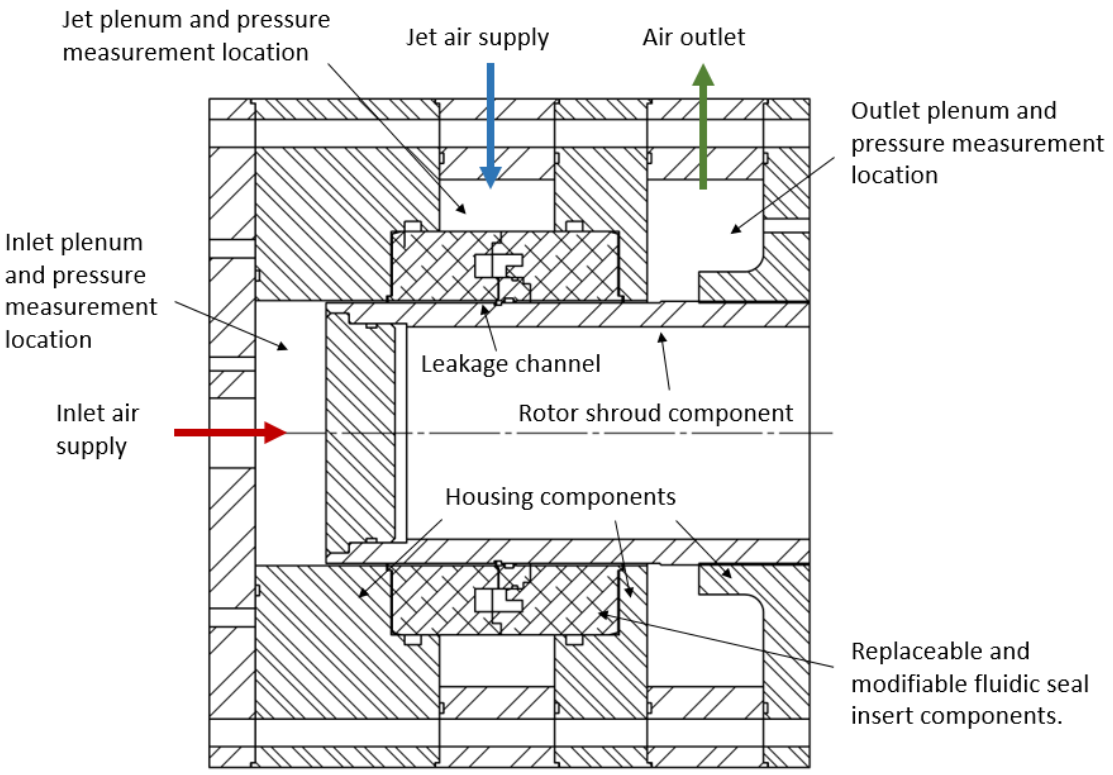

Figure 3.17: Cross View of the Stationary Rig Design, Including Fluidic Seal Insert

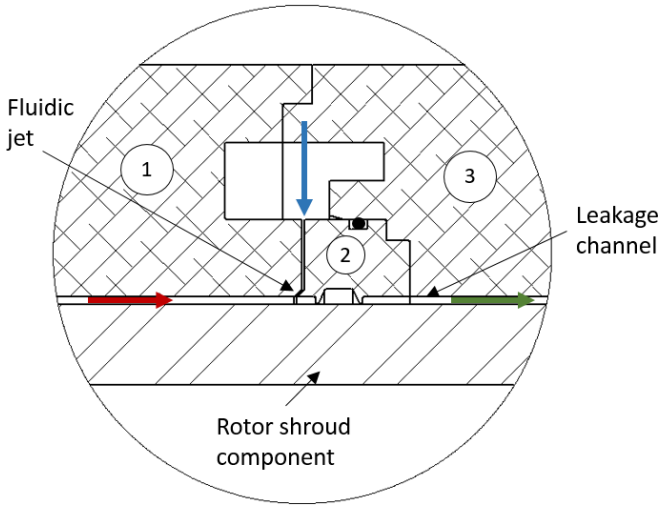

Figure 3.18: Detail View of the Fluidic Seal Insert Components 1,2 and 3

3.4.2 Durham Blow Down Test Facility Set up and Instrumentation

The test rig was integrated into the Durham Blow Down Facility as shown schematically in Figure 3.19. The inlet mass flow rate to the test section was measured using

Orifice Plate 3. An Inlet Valve positioned after orifice plate 3 was used to control inlet pressure to the rig. The seal mass flow rate was controlled by the Jet Inlet valve and was measured using Orifice Plate 2. The outlet pressure was controlled by Valve 3 and measured by Orifice Plate 1.

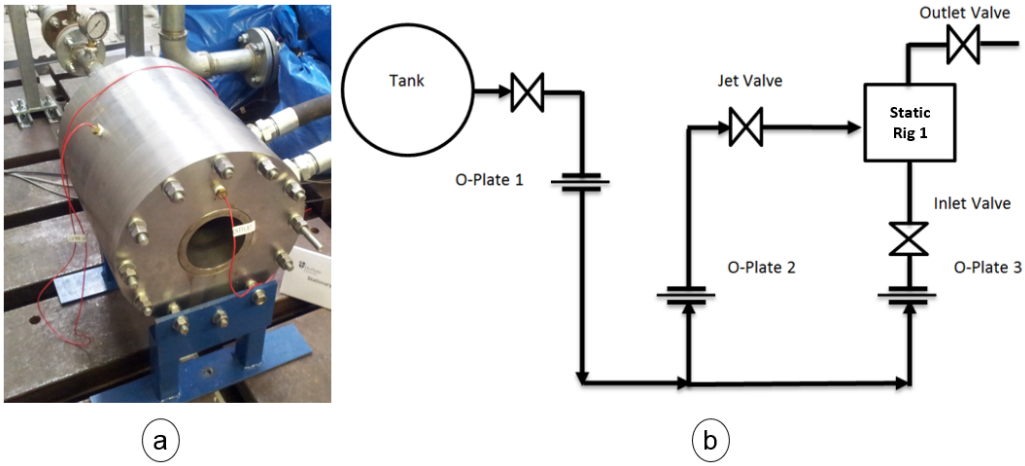

Figure 3.19: Schematics of Durham Blow Down Facility Including Static Test Rig

3.4.3 The Fluidic Seal Geometry Tested.

The geometry tested is shown in the diagram in Figure 3.20. It consisted of a 45° inclined jet opposing the direction of the leakage flow along the channel. The jet entered the leakage channel upstream of a labyrinth geometry consisting of two labyrinth fins with one expansion cavity between them. A wire 'blocker' is attached to the shaft surface between the axial location of the jet and the first labyrinth restriction. This feature was included to minimise the kinetic energy 'carry-over' from the jet flow into the flow through the first restriction. The main geometric dimensions are given in the Table 3.2.

The kinetic energy 'blocker' or 'stopper' was build by machining a groove into the rotor/shroud surface at the required axial location, setting the selected diameter copper wire into the grove and fixing the wire with an aluminium tape as shown in Figure 3.21. The result of this arrangement was a smooth surface over the top of the stopper. This shape was taken into account during the CFD investigations described later.

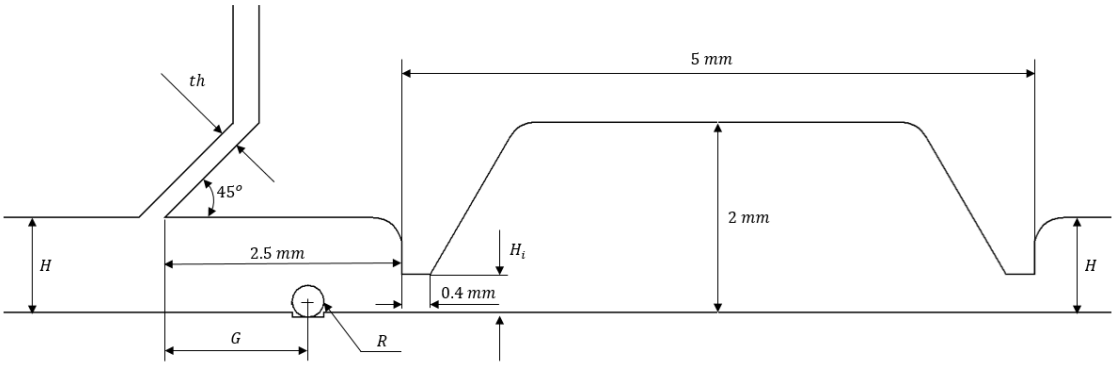

Figure 3.20: Diagram of the Static Test Rig Geometry.

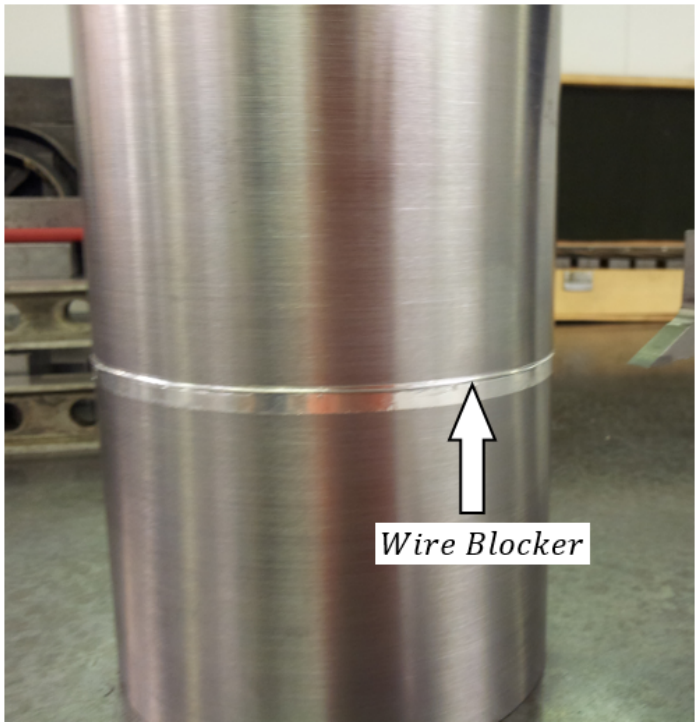

Figure 3.21: Picture of the Wire 'Blocker' Fixed to the Rotor Surface Using Aluminium Tape.

In one sequence of tests, the copper wire was removed leaving the aluminium tape in position to cover the grove and smooth the surface. This allowed the effect of the presence of the copper wire blocker on the leakage flow through the seal to be investigated.

Table 3.2: Key Dimensions as Depicted in Figure 3.20 and Choke Test Results.

Position	Description	Design Dimension [mm]	Choke Test Dimension [mm]
R	Wire Radius	0.41	n/a
th	Jet Gap	0.14	0.13
H	Leakage Path	1.00	n/a
H_i	Labyrinth Fin Clearance	0.5	0.44
G	Distance to Blocker	1.62	n/a
D_a	Leakage Clearance Outer Diameter	101.01	n/a
D_i	Rotor Diameter	100.01	n/a

3.4.4 Test Set-up and Procedure

The tolerances on the manufactured components could have a significant impact on some of the dimensions shown in Table 3.2. This could result in a large percentage error between the design values and actual values achieved in the assembled test rig e.g. jet width. A series of chocked flow tests were carried out at different pressure conditions to experimentally determine values for the jet width and the clearance underneath the labyrinth teeth.

In a choked flow, the mass flow is governed by the flow conditions upstream of the choked area. Equations 3.46 for chocked flow Massey [41] was uses to determine the choked area through the jet clearance area and the clearance area underneath the labyrinth teeth. A vertical shock was expected to appear in the jet clearance creating a truncated cone surface from which the jet thickness can be calculated using Equation 3.47. Equation 3.48 was used to calculate labyrinth fin clearance from the choked results. The resulting evaluated areas and clearances were later adopted in CFD calculations and are presented in Table 3.2.

$$\dot{m}_{jet} = A_{choked}\sqrt{\gamma p_{0jet}\rho_{jet}\left(\frac{2}{\gamma+1}\right)^{\frac{\gamma+1}{\gamma-1}}} \tag{3.46}$$

$$th = \frac{\sqrt{\left(\frac{D_a}{2}\right)^2 \pi^2 + \frac{\sqrt{2}}{2} A_{choked}\, \pi} - \left(\frac{D_a}{2}\right) \pi}{\frac{\sqrt{2}}{2}} \tag{3.47}$$

$$H_i = \sqrt{\frac{A_{choked}}{\pi} + \frac{{D_i}^2}{4}} - \frac{D_i}{2} \tag{3.48}$$

The experimental results were subsequently normalized by standard flow conditions as shown in Equation 3.49.

$$\dot{m}_{norm} = \dot{m} \frac{p_{0s}}{\sqrt{T_{0s}}} \frac{\sqrt{T_0}}{p_0} \tag{3.49}$$

3.4.5 Experimental Results

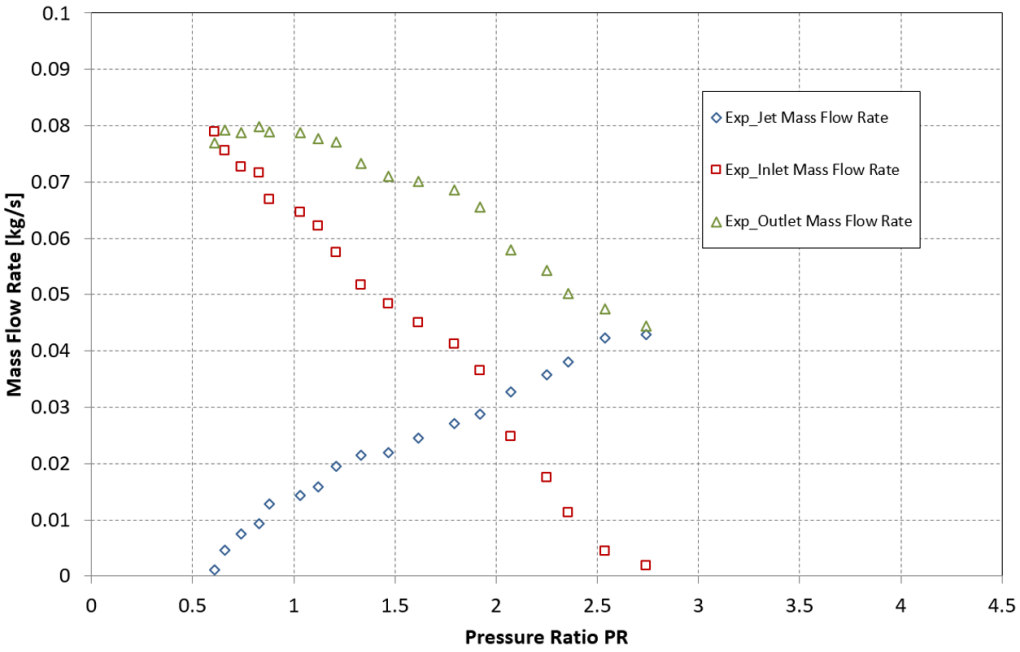

Figure 3.22: Experimental Mass Flow Rates against Increasing Pressure Ratio for Tests with Kinetic Energy Blocker in Place

The initial tests were carried out on the geometry described above and summarized in Table 3.2 with the jet kinetic energy blocker in place. In Figure 3.22 the jet mass flow rate is indicated by the blue diamonds, the seal inlet mass flow rate by the red squares and the seal outlet mass flow rate is indicated by the green triangles. The air was supplied to the inlet of the experiment at a nominal test pressure of 265 kPa and the outlet pressure was regulated to a nominal value of 190 kPa in all

tests. All experimental results presented in Figure 3.22, Figure 3.23 and Figure 3.27 are normalized by these standard conditions to reduce scatter in the data. The jet inlet pressure was stepwise increased, with measurements carried out after each jet pressure increase for values up to the PR values where the seal becomes overblown (see Section 3.1.5).

The experimental results in Figure 3.22 show a seal outlet flow rate reduction of up to 43% with the jet seal flow switched on. The demonstrated reduction of the seal outlet flow is the distinct experimental proof of the functionality of the fluidic jet seal in shown configuration.

The outlet mass flow rate reduction of up to 43% is calculated from the 'no jet' outlet flow rate of $\dot{m}_{PR=0.6} = 0.079kg/s$ and the reduced outlet mass flow rate of down to $\dot{m}_{PR=2.65} = 0.045kg/s$ at a pressure ratio of $PR = 2.65$ Beyond the pressure ratio of $PR = 2.65$ the seal is overblown (Mode (3) in Section 3.1.5) and a reversal of the seal inlet flow is seen from that point for further increases in pressure ratio.

The seal outlet mass flow rate is the main metric to categorize the effectiveness of the fluidic seal. Without the jet seal switched on, the flow through the leakage path is only restricted by the labyrinth seal. After the jet flow is switched on, with increasing jet pressure ratio, additional blockage is created by the fluidic jet, reducing the seal outlet flow until the seal becomes overblown.

Without the jet switched on, the pressure ratio of $PR = 0.6$ is measured (as shown in Figure 3.22). At this point the leakage path pressure is measured inside jet cavity. The initial pressure ratio without jet switched on is a function of the leakage path geometry and additional pressure drops in the inlet and outlet regions of the leakage path.

In the Figure 3.22 a relatively constant outlet mass flow rate between pressure ratios of PR = 0.6 and 1.0 can be observed. Beyond PR=1.0 two distinct outlet mass flow rate reduction gradients can be observed up to the over-blown condition PR=2.65. In the pressure ratio interval from PR 1.0 up to 1.9 the experimental results show a shallower mass flow rate reduction gradient, and between PR of 1.9 and PR 2.6, a steeper one. It is assumed that the steeper gradient is a result of increasing interaction between the fluidic jet and the kinetic energy blocker.

A constant reduction of inlet mass flow rate is shown in Figure 3.22 between the pressure ratios of 0.6 and 1.9. Beyond the PR of 1.9 a greater gradient of inlet mass flow rate reduction is observed.

The jet mass flow rate in Figure 3.22 increases faster between pressure ratios of 0.6 and 1.0 compared to a relatively lower increase between PR of 1.0 and the over blown condition. In the PR interval of 0.6 and 1.0, any reduction of seal inlet mass flow rate is compensated by approximately equal increase of jet mass flow rate, which results in a relatively constant outlet mass flow rate in this PR range.

A second series of tests were carried out on the geometry without the kinetic energy blocker present, these results are shown in Figure 3.23. The overall outlet mass flow rate reduction has been greatly reduced by removing the blocker to only 17% lower than the 'no jet' flow, compared to 43% reduction with the blocker present.

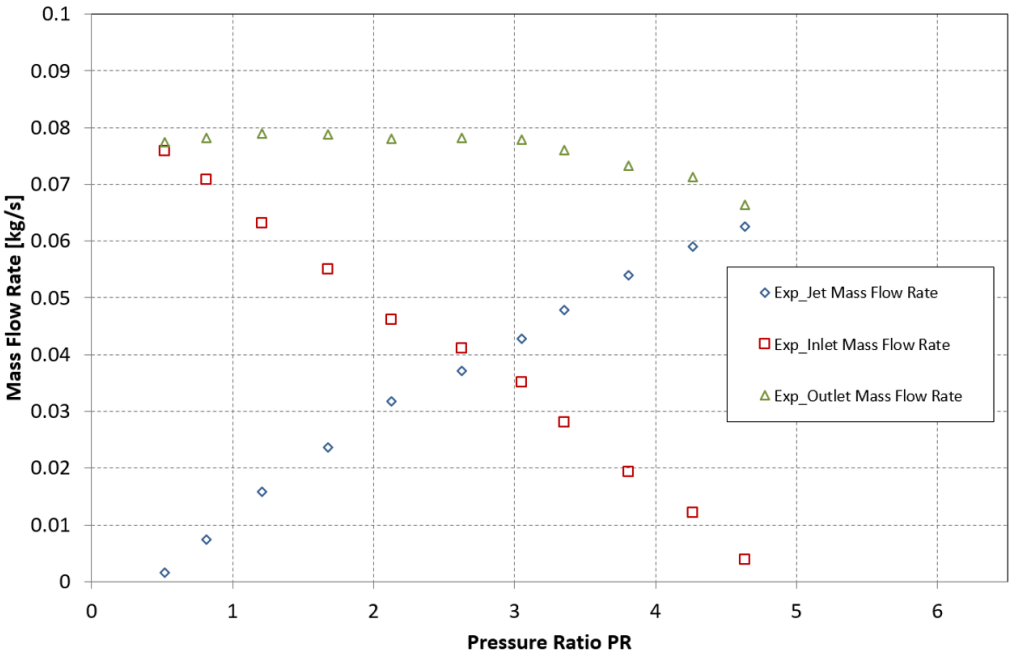

Figure 3.23: Experimental Mass Flow Rate for Configuration Without Kinetic Energy Blocker

In Figure 3.23, the over blown condition is reached at a much higher pressure ratio (PR= 4.9) compared to the case with the kinetic energy blocker present. With the majority of kinetic energy passing the downstream situated labyrinth seal unimpeded, due to the absence of the kinetic energy blocker, the downstream situated labyrinth seal is not contributing to the pressure reduction in which case the fluidic jet is

experiencing a lower pressure downstream of the jet slot compared to the results shown in Figure 3.22. With lower pressure downstream of the jet and the same pressure upstream of the jet, a higher jet inlet pressure is necessary for the jet to traverse the leakage path and to impinge upon the opposing wall creating a full blockage. The inlet mass flow rate in Figure 3.22 shows a constant decrease. The jet mass flow rate shows a slightly greater increase up to PR of 2.9 following a lower increase up to over blown seal condition. A combination of the inlet and jet mass flow rates up to a PR of 1.9 results in a small increase in outlet mass flow rate up to this pressure ratio.

3.5 Comparison of Experimental Data with Numerical and Analytical Results

3.5.1 The Numerical Method Used

The tools described in this section were used throughout the study to carry out Computational Fluid Dynamics (CFD) calculations.

3.5.1.1 Meshing

All the grids were generated using Pointwise V17. Generally, hybrid meshes were created employing for most parts structured blocks with a few unstructured blocks around complicated geometries. The grid generation was designed to be fully scripted to carry out calculations on a wide range of geometry variations. Throughout the CFD investigations, the density of the meshes was adjusted, when necessary, to resolve specific flow features. All meshes were designed to feature a wall boundary layer resolution with y+ around 30, with the y+ of 30 being the optimal near wall resolution for the turbulence model and wall functions used in the study. y+ is the non-dimensional wall distance to the first grid node. It is defined in Equation 3.50, where y is the distance to the wall, υ is the local kinematic viscosity, τ_w is wall shear stress and ρ the local fluid density . The cell growth factor was selected to be less than 1.2 in all meshes.

$$y+ = \frac{y}{\upsilon}\sqrt{\frac{\tau_w}{\rho}} \tag{3.50}$$

For all cases, a mesh dependency study was carried out and the optimal grid resolution was selected, which delivered a grid independent result with the least number of cells.

The numerical domain and the mesh used for CFD calculation of the case with the kinetic energy blocker present, as described in Section 3.4.3, is shown in Figure 3.24. The mesh consists mainly of a high quality 2D structured grid, except around the kinetic energy blocker, where the mesh is unstructured to enable automated meshing for further cases studied.

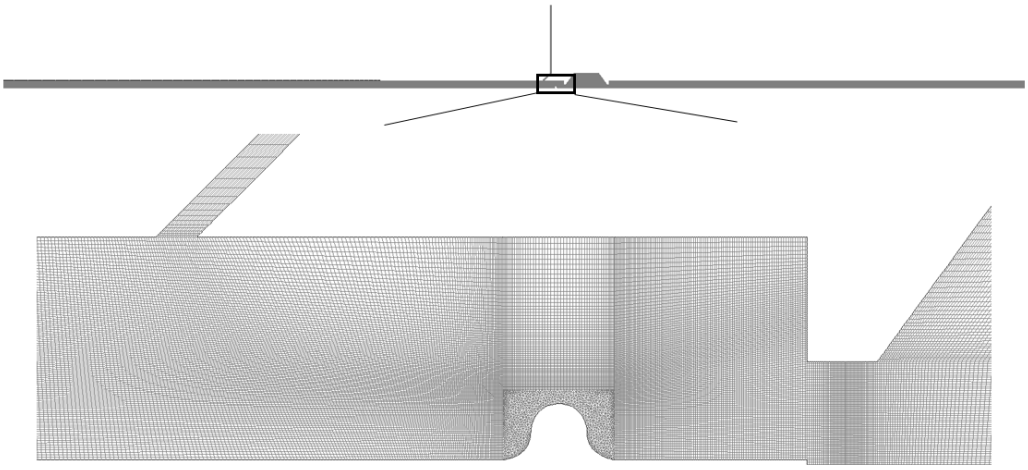

Figure 3.24: Computational Domain and Mesh for the Case with Kinetic Energy Blocker Present.

3.5.1.2 CFD

ANSYS Fluent V14.5 and later Fluent V15.0 double precision solver were used to carry out all CFD calculations (no difference in results was observed between both releases). In all cases, a steady, pressure based solver in a 2D axisymmetric geometry was used. The realizable k-epsilon model as defined in Fluent Theory Guide [1] was used with standard wall functions. The realizable k-epsilon model is a modification of a standard k-epsilon model using an alternative formulation of turbulent viscosity compared to the standard model it shows an improvement over the standard k-epsilon model in areas with strong flow gradients, including strong streamline curvatures, vortices and rotation. The standard wall function is the default option in ANSYS Fluent and is based on work by Launder and Spalding [37], [38]. Further, the energy calculation model was used in all calculations.

A pressure inlet boundary condition was used on the inlet of the domain, where gauge total pressure was specified with a flow direction vector. A pressure outlet condition was used at the outlet, where guage static pressure was specified. On the inlet and outlet (for cases where inflow was present across the exit boundary) turbulence was specified using turbulence intensity and length scale with 5% turbulence intensity being selected for every calculation and the turbulence length scale was calculated based on the assumption of the length scale ranging between 5% and 7% of the channel hight.

SIMPLE, a pressure-velocity coupled solution method was selected with high order term relaxation, which is the default solution method in ANSYS Fluent. In the first step a CFD solution was usually obtained using first order upwind discretization to increase convergence speed and stability. Following first order solution, second order upwind discretization was selected and a final solution obtained. Lower under relaxation factors were set in order to increase the stability of the computation, reducing some of the factors by 60%. The reduction of under-relaxation factors usually stabilized the solution allowing to reduce the residuals even further, but at the same time increase the computational time.

Solution initialization was performed in all instances using the hybrid initialization method offered by ANSYS Fluent, where boundary variables such as temperature, turbulence and others are automatically patched based on domain averaged values and velocity and pressure field are calculated by solving simplified equations.

Each calculation was run until the highest residual fell below a scaled absolute value of $1 * 10^{-5}$. Further, the mass flow rate across the inlets and outlet were calculated in real time, which provided a secondary convergence criteria, based on the residual error in mass continuity through the calculation domain.

3.5.1.3 Post-Processing

The initial Post-processing of the CFD results was carried out using ANSYS Fluent post processing tools. After the initial post-processing, the Fluent solutions were exported to ANSYS Post, where the majority of contour plots and graphs were created. The comparison of CFD and experimental results was carried out using spread sheets and Matlab automated scripts.

3.5.2 Comparison of Experimental and Numerical Results

The solid markers shown in the Figure 3.25, represent results from CFD calculations carried out on a 2D axisymmetric geometry, as described in the previous section, and the open markers show mass flow rate results from the experimental measurements. Overall it can be observed, that both the numerical calculation and experimental results show a good agreement in the reduction of the outlet mass flow rate. The numerical results in Figure 3.25 show a somewhat lower outlet mass flow rate reduction of 40% compared to experimental seal outlet mass flow rate reduction of 43%.

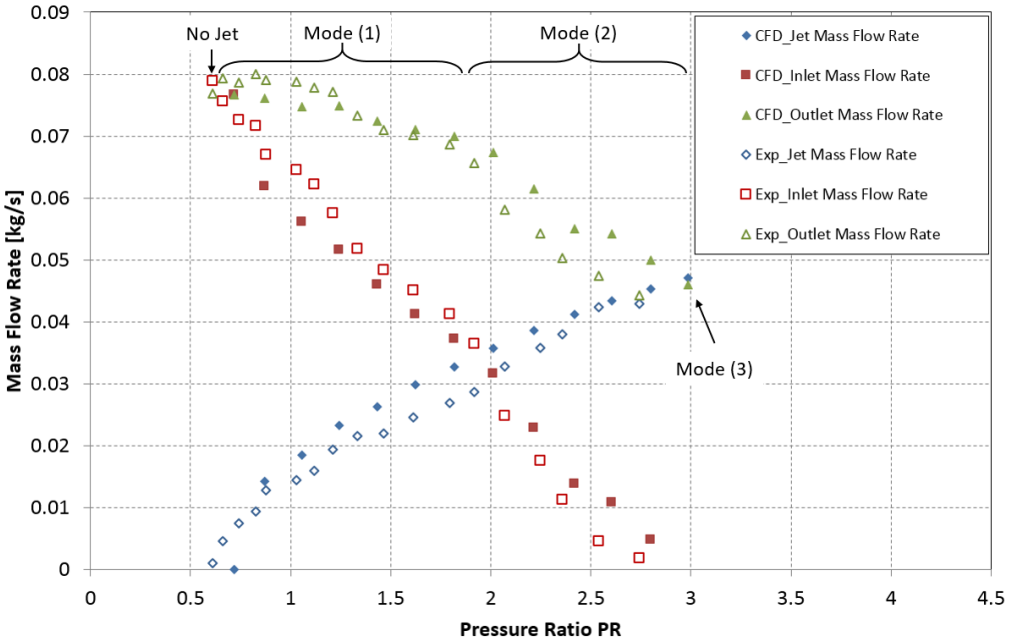

Figure 3.25: Mass Flow Rate, Experimental and Numerical Results

Further it can be seen, that in numerical simulations, the leakage mass flow rate for the case without a jet flow present, corresponds to the pressure ratios PR around 0.6, similar to that found in the experimental result. In a supplementary CFD simulation where the labyrinth part of the seal was removed and replaced with smooth wall with remaining dimensions of the seal kept the same, the initial (no jet) pressure ratio dropped to $PR = 0.5$. The pressure ratio difference between the smooth wall and labyrinth seal is due to the presence of the pressure drop across the labyrinth seal. The pressure ratio PR shifts upward toward $PR = 1$ in cases where the jet slot is situated upstream of a restriction in an otherwise unrestricted channel.

Between the pressure ratios PR of 2.6 and 3.0 both numerical and experimental results in Figure 3.25 reach overblown conditions, with extrapolation suggesting that the experimental results reaching overblown conditions (Mode (3)) at a PR value of 2.7 and CFD results reaching overblown conditions at a PR of 2.9. The increase of Mode (3) pressure ratio in CFD could be a result of geometrical uncertainty associated with manufacturing tolerances on several components, such as the diameter of the kinetic energy blocker or the axial distance between the blocker and the first labyrinth restriction, as well as the shape of the first labyrinth fin.

Two distinct outlet mass flow rate gradients can be observed in the CFD results, similar to the trends already observed in the experiments. A shallower gradient between the pressure ratios of 0.6 and 1.9 and a steeper gradient between the pressure ratios of 1.9 and 2.5. In the area of a shallow gradient ($PR = 0.6 - 1.9$) examination of the flow structure in the CFD solutions (Figure 3.26) reveals that a free jet in the cross flow is formed, not impinging upon the opposing wall and only partially blocking the leakage path. In this pressure ratio interval the fluidic jet flow and leakage inlet flow are barely influenced by the kinetic energy blocker and the seal is considered to be in Mode 1 as discussed in Section 3.1.5, where the jet is not impinging on the opposing wall and is not significantly influenced by the kinetic energy blocker. In Figure 3.26(1) a Mach number contour plot of the CFD results for the pressure ratio $PR = 0.9$ is shown, with the jet creating a partial leakage path blockage.

Beyond $PR = 1.9$, the jet flow starts to increasingly interact with the kinetic energy blocker and the opposing wall. In Figure 3.26(2) a Mach number contour plot for the pressure ratio of $PR = 2$ is shown. Further it can be observed, that the kinetic energy stopper is working even at low pressure ratios before the jet is fully impinging upon the opposing wall, deflecting the flow away from the shroud surface and preventing a formation of a wall jet on the shroud surface, which would otherwise maximise the kinetic energy carry-over of jet momentum under the first labyrinth fin. From $PR = 1.9$ where the jet starts to increasingly interact with the kinetic energy blocker and a steeper gradient of outlet flow reduction is observed, the seal is considered to be in Mode 2. From $PR = 2.5$ the jet starts to impinge upon the opposing wall creating a complete leakage path blockage. An increase in pressure ratio, beyond $PR = 3.0$ in CFD, results in a reversed seal inlet flow, as shown

in contour plot in Figure 3.26(3), at which point the seal is in Mode 3 (over-blown condition).

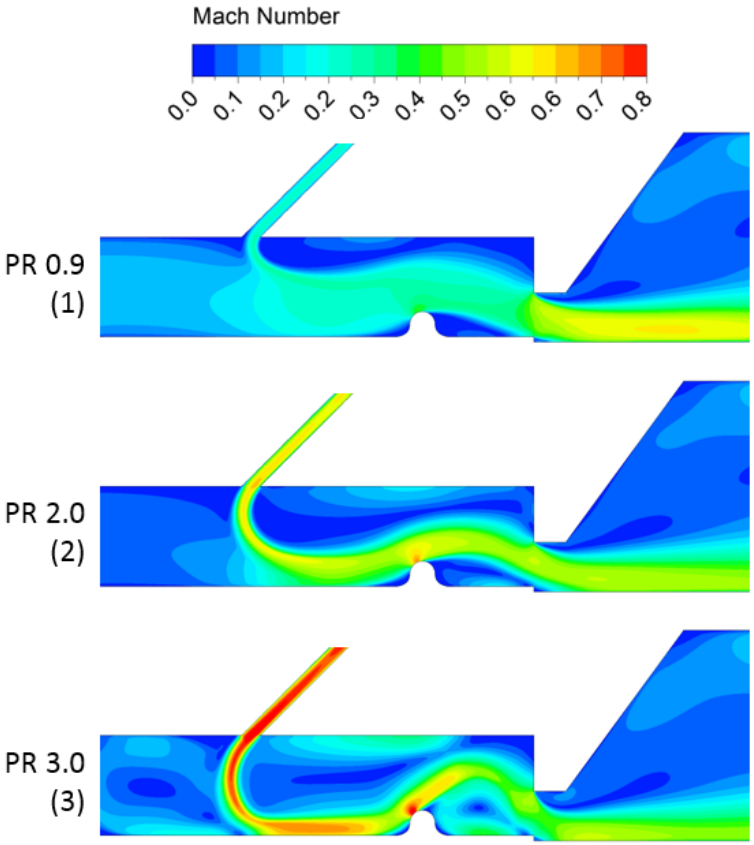

Figure 3.26: Mach Number Contour Plots Extracted from Numerical Results as Shown in Figure 3.25

A series of CFD calculations were also carried out on the geometry without the kinetic energy blocker present, as shown in Figure 3.27 where this data is compared to the experimental measurements for this case. The overall outlet mass flow rate reduction in the CFD predictions was around 12% compared to the experiment results of 17%. It is observed that overblown condition in the CFD predictions was reached at a similar pressure ratio, to that found in the experiments, at around $PR = 4.9$. Overall the CFD results show a reasonable agreement with the experimental results.

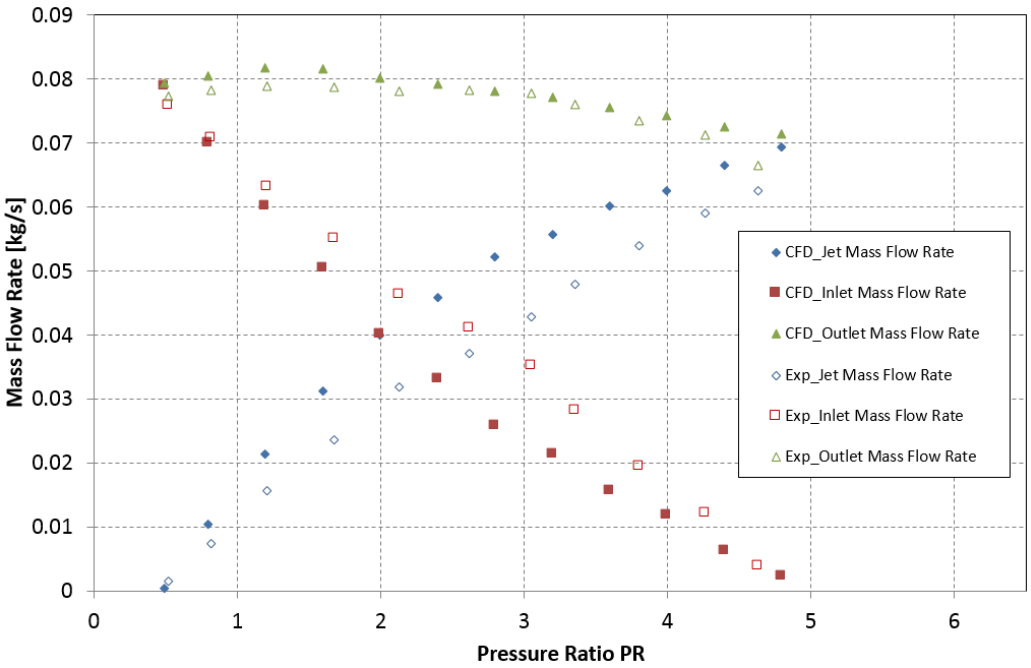

Figure 3.27: Mass Flow Rate, Experimental and Numerical for Configuration Without Kinetic Energy Stopper

3.5.3 Validation of the Analytical Model against the Experimental and CFD Results

Results obtained using the analytical model described in Section 3.2, are presented alongside the experimental and numerical results in Figure 3.29. The analytical mass flow rates were calculated based on the pressures extracted from numerical results at the positions shown in Figure 3.28. The pressure downstream of the jet inlet into the leakage path is additionally dependent on the downstream labyrinth seal restriction. The effect of the labyrinth seal geometry is taken into account here, by using the pressures from the CFD calculations at positions as indicated in Figure 3.28.

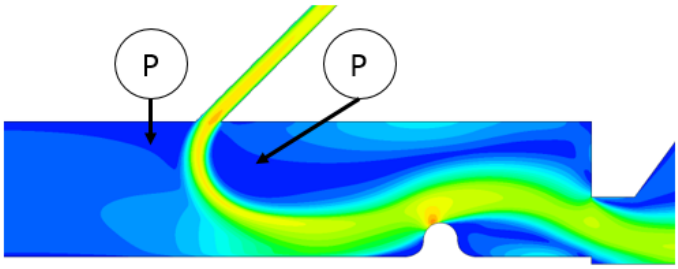

Figure 3.28: Pressures Positions Extracted from CFD for Analytical Calculations

The analytical mass flow rate calculation of the jet flow shows an excellent agreement with the jet mass flow rate observed in CFD results above $PR = 1.2$ (Figure 3.28). Similar to the jet flow, the inlet mass flow rate calculated using analytical model, shows a good agreement with CFD and experimental results above $PR = 1.2$. Below this pressure ratio, the analytical model over-predicts the inlet flow rate. Essentially, below the pressure ratio of 1.2, the jet breaks down soon after leaving the jet slot and before forming a blockage as calculated using the analytical model, in which case less of the leakage passage is blocked.

Further, a jet flow Reynolds number increase and the inlet flow Reynolds number decrease and with it associated change in Gaussian coefficient αg for the entrainment calculation and discharge coefficient C_d is not incorporated into the analytical model and could be an additional cause of uncertainties in the inlet flow mass flow rate calculation. The Gaussian entrainment coefficient is greatly dependent upon the jet Reynolds number as shown in Section 3.2. In Figure 3.30 the change in jet and inlet flow Reynolds numbers are shown.

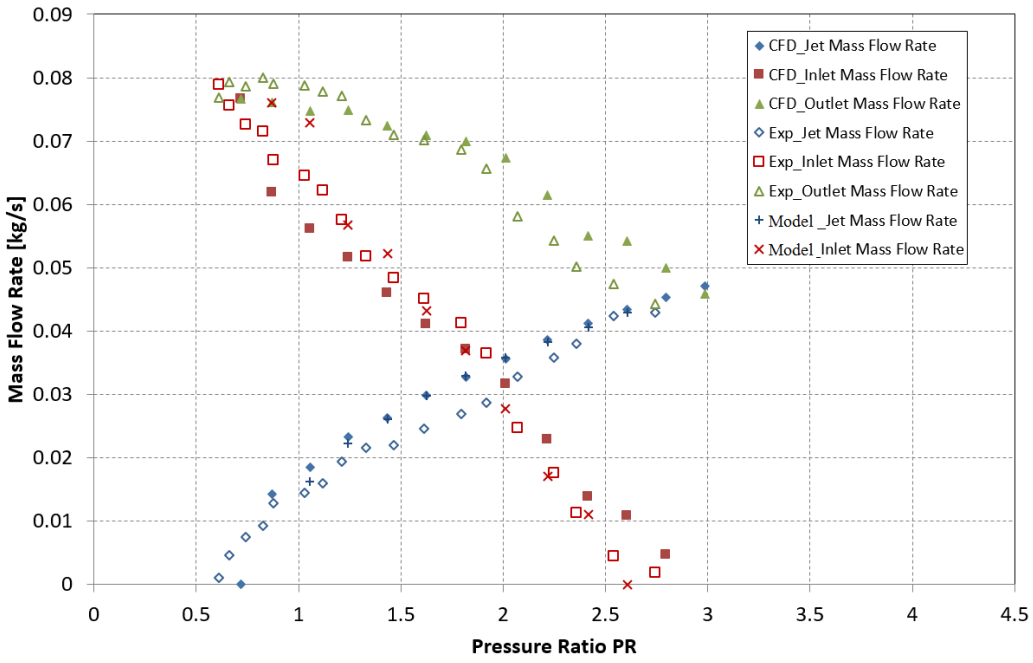

Figure 3.29: Mass Flow Rate, Experimental, Numerical and Analytical Results

As mentioned in Section 3.2 the entrainment factors are usually based on empirical investigations. In the fluidic seals, where the jet transits from being a week

jet in strong cross flow to a strong jet in week cross flow, additional investigations (experimental and numerical) are needed to evaluate the Gaussian entrainment factor change, since there is little published data available on planar jets in confined spaces in a cross flow.

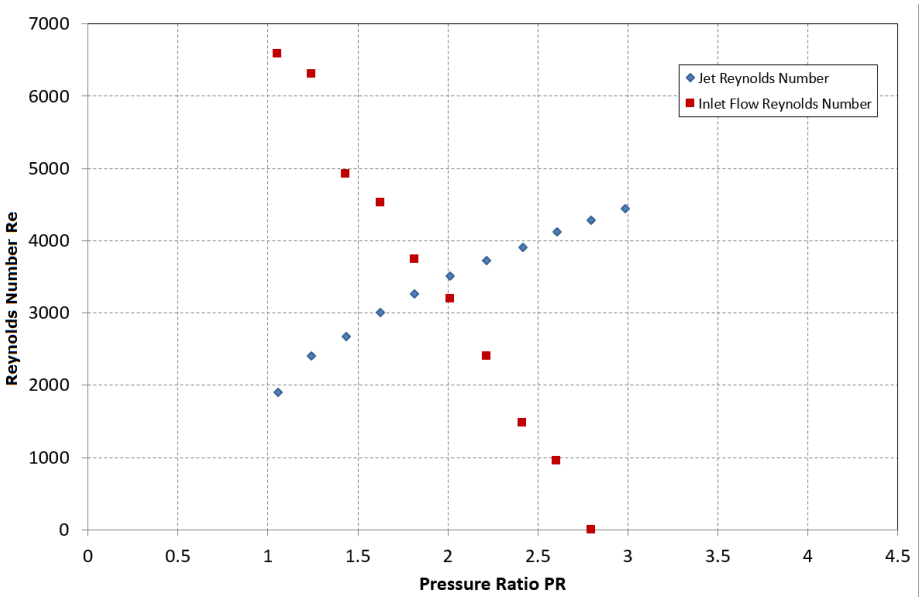

Figure 3.30: Jet and Inlet Flow Reynolds Numbers

3.6 Conclusion

Concluding, this chapter can be summarised by the following points:

1. A new type of seal device for improving the performance of all types of turbomachinery seal has been described.

2. The concept has been validated and demonstrated by experiment.

3. 2D RANS-CFD and predictions obtains using an analytical model described in this chapter, show a reasonable agreement with the experimental results.

4. Using 2D RANS-CFD key flow features of the fluidic seal have been modelled and successfully identified.

5. The results show that leakage flow reductions of over 40% can be achieved by using fluid jets to decrease the pressure drop across standard turbomachinery seals, in the manner described in this chapter.

6. The ideas described in this chapter were registered for a patent. The description of the patent is presented in Appendix A.

7. The CFD methods and blow down test facility described in the chapter will be used to carry out the predictions and experiments throughout the studies described in this thesis.

Chapter 4

Design of a Fluid Curtain Seal to Reduce Rotor Tip Leakage on a Single Stage Turbo Expander Unit

4.1 Project Introduction

The investigations in this part of the thesis were carried out in a collaboration with the Cummins Turbo Technologies. The objective of the collaboration was to redesign the original single stage rotor tip seal geometry to incorporate the fluid curtain type seal technology described in the previous chapter into the turbo expander unit, with the aim of increasing the expander unit efficiency. A fluid curtain type seal is created by a jet introduced into a leakage channel along the circumference to create a cross-flow that generates primary blockage in the form of a fluid curtain.

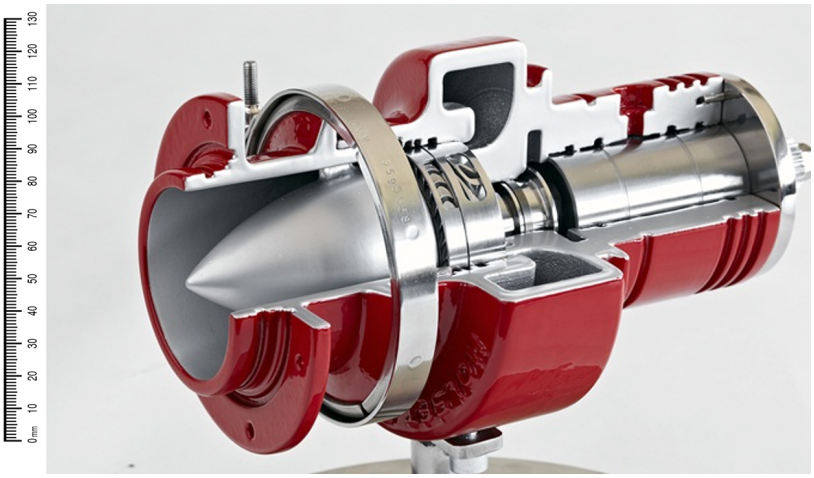

Figure 4.1: Cut-Through Cummins Waste Heat Turbo Expander Unit [27].

Figure 4.1 is a cut-through of the unmodified turbo expander unit. The turbo expander was developed for use as the power take-off in an organic Rankine cycle waste heat recovery system, to capture what would otherwise be lost heat energy from a number of sources on their large automotive diesel engine units. The system is designed to recover up to 25 kW of mechanical and electrical energy, that can be used to reduce the vehicle specific fuel consumption by up to 8%. [27]. The fluidic seal design for the turbo expander unit described in this chapter has also been published in an ASME conference paper Auld et al. [5].

4.2 Initial Test Geometry and Numerical Methods Used

The modified rotor tip seal incorporating a fluidic jet for the Turbo Expander unit was designed and optimised in a series of two dimensional axis-symmetrical CFD calculations. The optimisation process was based on a permutation of main seal geometrical features, including the axial position of the jet, angle of the jet and the jet width. The investigation was carried out utilizing fully automated Matlab scripts and an automated computational grid generation process in Ansys ICEM 14.5. For each permutation of allowed geometries, the mesh was generated and calculations carried out for a range of jet pressure ratio (PR) values. The optimised design was selected by analysing the matrix of calculation results obtained in this way.

4.2.1 Original Rotor and Tip Seal Design

The original Turbo Expander tip seal configuration is shown in Figure 4.2, where the red arrows indicate flow paths. The main flow enters the turbine before the volute (1), where the flow is turned and distributed equally to the inlet of the stator nozzles (2). The fluid exiting the nozzles of the stator (4) has a high swirl angle of around 80 degrees.

The turbine was designed to operate at high stage pressure ratios, so the flow through the stator nozzles is choked. The nozzle exit flow is deflected by a rotor with 34 buckets. The stage design is low reaction with the reaction ranging between 3% and 10% and so most of the turbine shaft power was generated by converting energy from the swirl momentum of the flow entering the rotor (4). The rotor tip shroud

flow (5) enters the leakage path with the same high levels of swirl momentum that was present at nozzle exit.

Careful accounting for shroud shear forces is important when optimising fluidic seal designs for turbine applications and it will be described later in the chapter. The over-tip leakage flow re-enters and mixes with the stage exit flow (3) immediately downstream of the rotor, before being exhausted from the turbine in the axial direction. The additional leakage path between the rotor and stator centre-body (6) into the bearing chamber (bearing chamber not depicted in Figure 4.2) was excluded in current CFD investigations. The major turbine design parameters are given in Table 4.1.

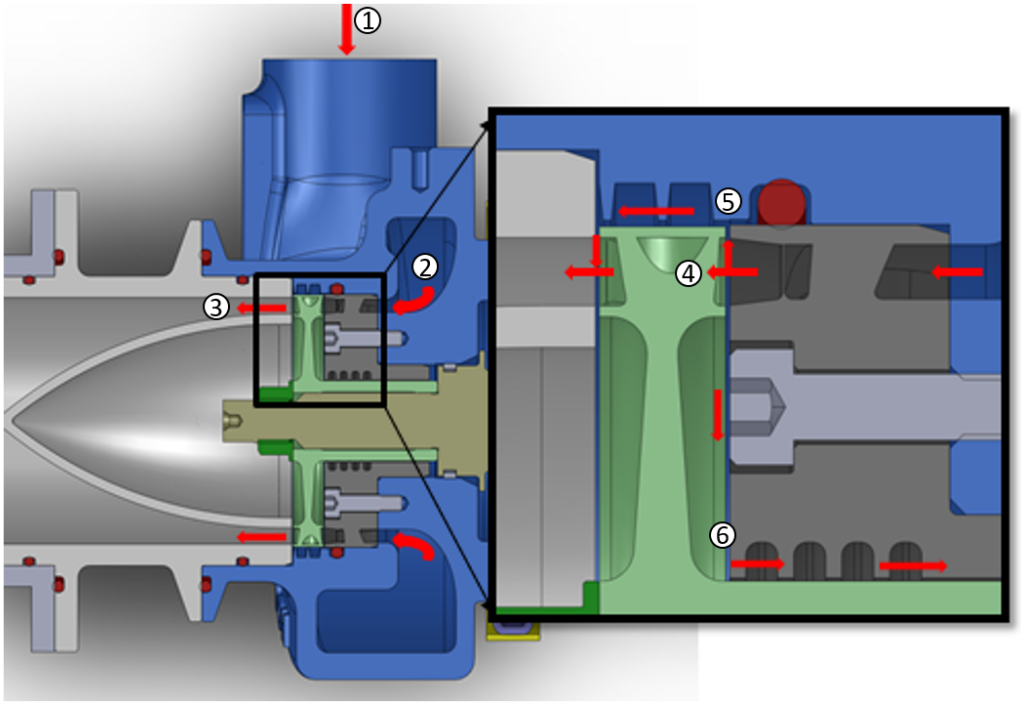

Figure 4.2: Cut-Through the CAD Model of the Original Turbine and Tip Seal Design.

The original rotor tip seal design, is shown in Figure 4.3. It features three radial restrictions and two radial expansion chambers with a radial restriction clearances of 0.35 mm. In addition to the radial restrictions, the tip seal also featured tight axial clearances of 0.25 mm, in the inlet and exit regions of the tip seal cavity. Density effects determine that the greatest pressure drop is carried by the last restriction in any multi-restriction seal system. The axial clearance in the exit region of the shroud seal therefore exerted the greatest influence on the leakage flow through the rotor tip

Table 4.1: Turbine Design and Operating Parameters.

Turbine Type	Impulse
Rotor Diameter	63 mm
Nominal Operational Speed	50,000 RPM
Rotor Blade Height	4.1 mm
Shroud Axial Length	8.0 mm
Nominal Reaction	3%
Nominal Pressure Ratio	2
Power Output	up to 25 kW
Working Fluid	R245fa

seal cavity. The red dashed line in Figure 4.3 indicates modified tip leakage path geometry, where the radial expansion chambers have been replaced by a constant hight annular channel, with radial clearance now equal to 0.35 mm all along the shroud. In the new design, the tight axial inlet and outlet restrictions have been maintained.

4.2.2 CFD and Optimisation Methods Used to Design the Fluidic Seal

Figure 4.4 shows a typical 2-D axisymmetric CFD mesh used in the design optimisation calculations. The domain shown is for the modified constant height leakage path geometry with a single continuous circumferential inclined fluidic jet applied through the casing wall. The main stage flow through the the blade passages is not included in the calculation domain. The jet is angled, so that it entered the tip seal with a component of its momentum opposing the leakage flow through the seal. The inlet and outlet areas were extended in the radial direction toward rotational axis partially covering rotor inlet and exit flow areas as shown in Figure 4.4. The extension of the domain in axial direction upstream of the rotor inlet plane covered part of the nozzle location. The nozzle was not modelled explicitly in the calculations, instead the nozzle outlet total pressure, temperature and swirl angle were applied at the inlet boundary and constant static pressure set at the outlet boundary. The flow rate through the jet inlet was varied by changing the jet inlet total pressure at

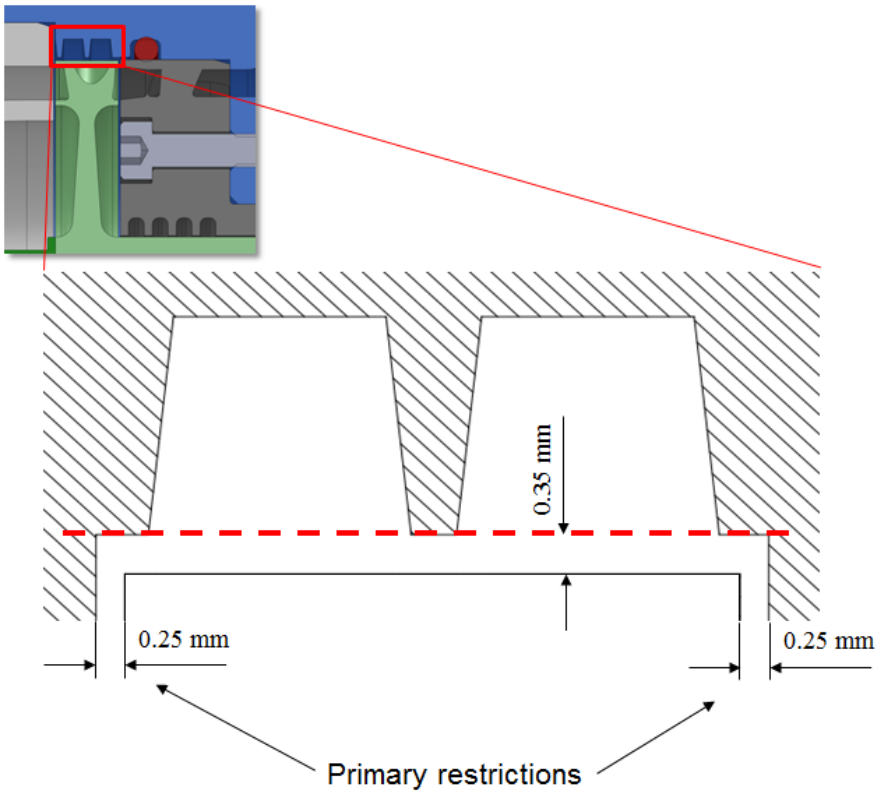

Figure 4.3: Original Seal Design and Modification.

the jet inlet boundary. The rotor tip surface was set to rotate at 50,000 RPM. The CFD calculations were carried out using Ansys Fluent 14.5. All calculations used the SIMPLE pressure-correction solver and a high quality structured mesh shown in Figure 4.4. A mesh study confirmed that the mesh density was sufficient to ensure mesh-independent solutions. The $\kappa - \epsilon$ turbulence model was used throughout the investigations. Refrigerant R245fa is used as a working fluid for CFD calculations in this chapter. In this application the gas is superheated at the inlet of the turbine and due to the expansion in the dry region the working fluid is also superheated at the outlet of the turbine [51].

Further settings and considerations used in all the numerical investigations were discussed earlier in Section 3.5. The boundary conditions used as well as the turbine operating parameters are summarised in Table 4.2.

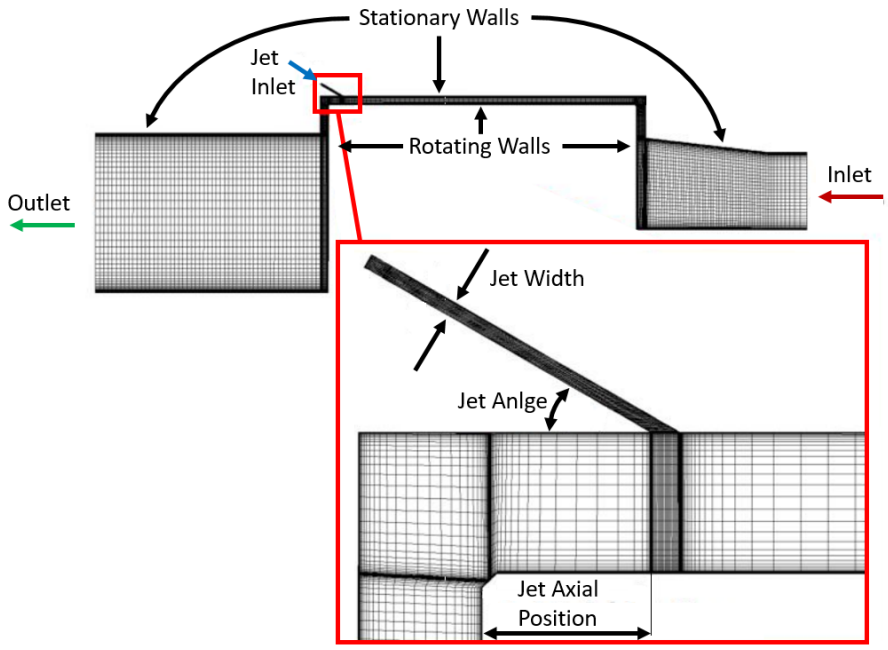

Figure 4.4: Example of a Grid Used for CFD Calculations in this Chapter.

Table 4.2: CFD Boundary Conditions.

Rotor Inlet Total Pressure	4.67 bar
Rotor Inlet Swirl Angle	80°
Rotor Outlet Static Pressure	4.14 bar
Rotor Speed	50,000 RPM
Rotor Inlet/Outlet Turbulent Intensity	5%
Rotor Inlet/Outlet Turbulence Length Scale	0.096 mm
Jet Inlet Turbulent Intensity	5%
Jet Inlet Turbulence Length Scale	0.00245 mm
Jet Inlet Total Pressure	Variable
Working Fluid	R245fa

4.2.3 Results of Leakage Path Modification to the Baseline (i.e. no-jet) Seal.

The original seal design was modified to feature a constant height channel in order to accommodate a fluidic jet. The modification to the baseline tip seal design had essentially no effect on leakage mass flow through the rotor shroud seal cavity, because

the axial shroud clearances were controlling the leakage flow and these have not been changed. This is illustrated by the CFD results for static pressure shown in Figure 4.5. The pressure drops across the axial restrictions at the inlet and exit of the shroud seal are essentially unchanged by the modification to the tip seal design. The red arrows indicate the flow direction through the seal. The calculated leakage mass flow rates for the two designs are included in Figure 4.5. The design modification can be seen to have less than 1% effect on the calculated mass flow through the tip seal.

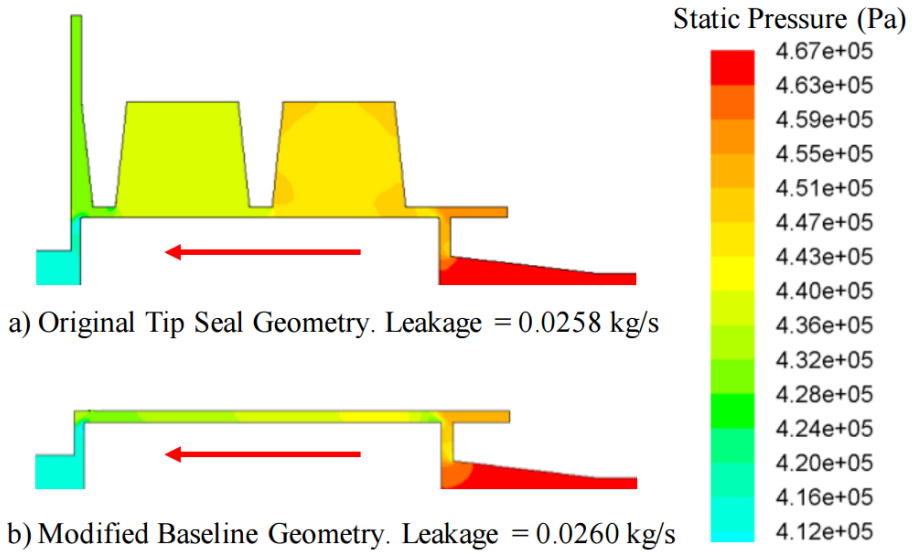

Figure 4.5: Static Pressure Distribution and Leakage Mass Flow Rates for the Original and the Modified Tip Seal Geometry.

In the following section, the leakage mass flow reduction calculated for flows with a fluid jet introduced into the constant height tip seal leakage cavity shown in Figure 4.5(b) are calculated. The leakage flow reduction will therefore be the same as that compared to the original tip seal geometry in Figure 4.5(a).

4.2.4 Optimisation of the Fluidic Seal Design

The fluidic seal design was optimised by investigating the change of the turbine power output of changing the design parameters (α, b, c), as shown in Figure 4.6. The pressure ratio (PR) of the fluidic jet supply remains defined according to Equation 3.2. Optimisation calculations were carried out for values of PR starting from 1.0 and increasing in steps of 0.4 until the fluidic seal reached the over-blown condition (Mode 3).

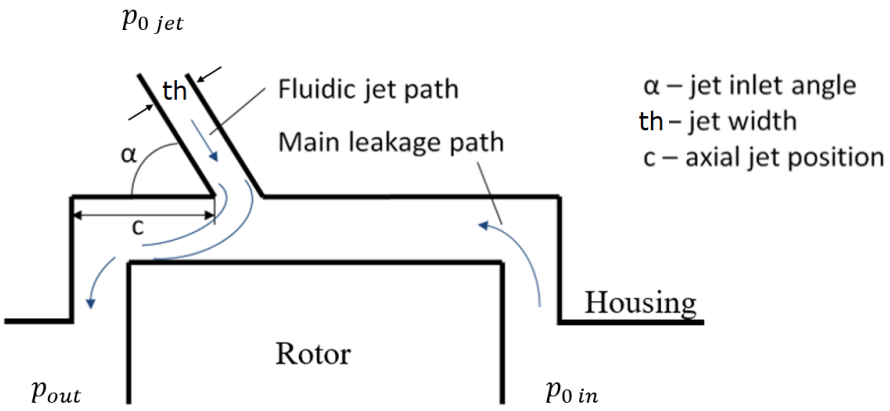

Figure 4.6: Fluidic Seal Optimisation Parameters

As shown in Figure 4.6, during the optimisation process the axial width of the jet (th), jet angle (α), axial distance from the corner (c) were varied. The angle was varied between 60°, 45 ° and 30 ° degrees. The distance from the corner was changed between 0.5 mm, 0.36 mm and 0.21 mm. The jet width investigated was varied in three steps between 0.035 mm and 0.064 mm. The jet inlet pressure p_{0jet} was varied to change PR whilst maintaining the leakage path inlet pressure p_{0in} and outlet pressure p_{out} constant. The complete permutation matrix is shown in Table 4.3.

Table 4.3: Fluidic Seal Permutation Table.

	Min		Max
Jet Angle (α)	30°	45°	60°
Distance from Corner (c)	0.21 mm	0.36 mm	0.5 mm
Jet Width (th)	0.035 mm	0.044 mm, 0.053 mm	0.062 mm

4.2.5 Results Extraction

The results were extracted from the CFD calculations using Ansys Fluent 14.5 and Ansys Post 14.5. The mass flow rates were calculated across the inlet and outlet boundaries for a full circumferential geometry. The effect of the jet on the power delivered by the turbine was also calculated for the full annular rotor.

4.3 Optimisation Results

4.3.1 Effect of Varying Jet Width (th) with Fixed Jet Angle (α) and Distance From the Corner (c)

Seal leakage mass flow rate predictions for a constant jet angle of 45° and a constant distance from the corner of 0.500 mm, are shown in Figure 4.7, for jet widths (th) in the range shown in Table 4.3 for increasing values of PR up to the point where the seal becomes overblown (i.e. onset of Mode 3 operation described in section 3.1.5). The leakage mass flow rate values in the Figure 4.7 are the seal outlet mass flow rates of the sum of the leakage flow through the inlet into the shroud seal from upstream of the rotor, plus the mass flow of the fluidic jet, that is the total leakage flow exiting the tip seal.

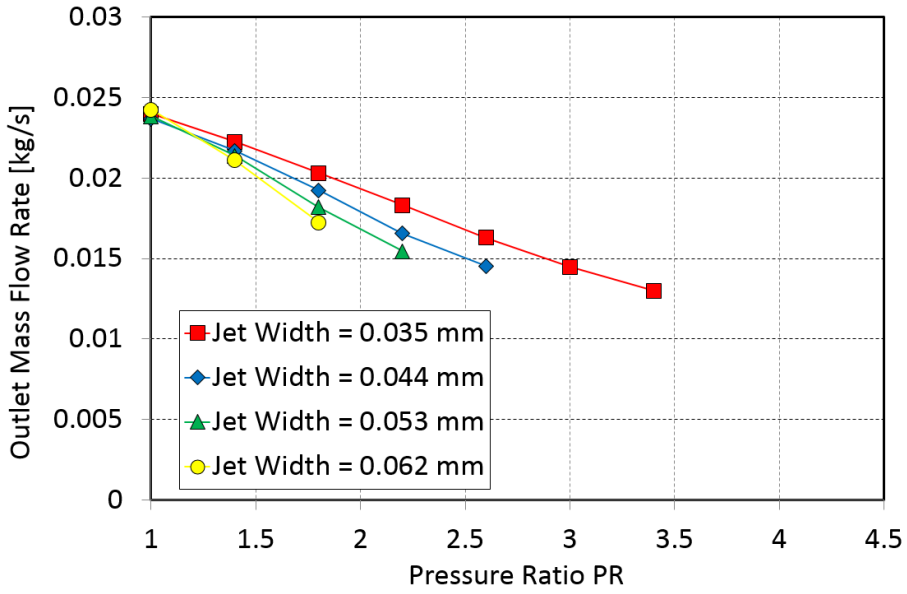

Figure 4.7: CFD Leakage Flow Predictions for Jet Angle 45° and Distance from Corner = 0.5 mm.

The results in Figure 4.7 show, that with narrower fluidic jet, a greater reduction in total leakage flow exiting the seal can be achieved (there is a higher jet flow momentum for a given mass flow rate as the jet is narrowed). The figure also shows that with narrower fluidic jet a higher jet pressure ratio being required in order to achieve a given reduction in leakage flow. It is also evident from the results, that greater leakage flow reductions can be achieved with narrower jets, before the over-blown seal condition

(Mode 3) is reached. For the narrowest jet examined (jet normal width = 0.035 mm), the results indicate, that a reduction in total leakage mass flow compared to the no-jet case of up to 50% is possible, for this jet angle and axial position.

Reducing the tip seal leakage flow resulted in a greater proportion of the stage flow passing through the rotor blade row, increasing the output power from the stage.

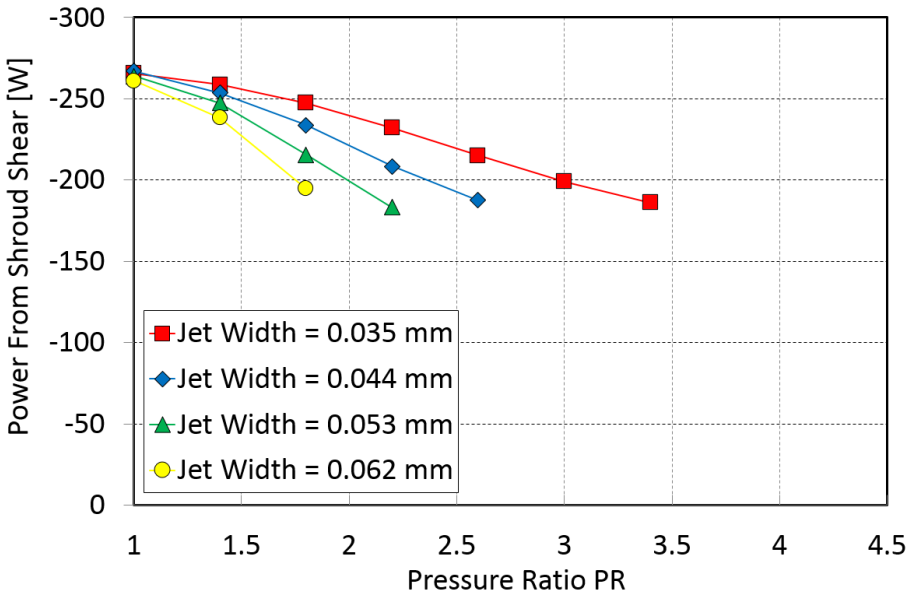

Figure 4.8: Predicted Rotor Power Change Resulting from Effect of Shroud Shear Forces for Jet Angle 45° and Distance from Corner = 0.5 mm

Values for the power loss due to the shear forces acting on the blade tip shroud outer surface (the total shear force in the circumferential direction multiplied by the shroud surface linear speed), are shown in Figure 4.8. The data plotted has been extracted from the CFD calculations used in Figure 4.7. Without a fluidic jet present, the shear forces acting on the shroud surface contributed approximately -270 W reduction in rotor power. When the fluidic jet is turned on, the mass flow rate through the leakage path is reduced, so the shroud work to maintain the swirl momentum in the leakage flow is reduced as well. The shroud shear power loss reduced to just over -190 W (i.e. an 80 W improvement) under the conditions that resulted in the greatest leakage mass flow reductions, as shown in Figure 4.7. Figure 4.9 shows the circumferential velocity profiles radially across the leakage flow at 50% axial shroud distance for the flow conditions without a jet and with a jet at pressure ratio of 3.4 and jet width of 0.035 mm, which is seen in Figure 4.7 to result in the maximum blockage.

Figure 4.9 shows a turbulent velocity profile with an average circumferential velocity below the circumferential velocity of the shroud. This shows, that for most of the distance along the shroud surface, shroud shear is putting work into maintaining the swirl momentum of the leakage flow, that is the rotor is doing work on the fluid. The Figure 4.9 was extracted from the data of the CFD calculations.

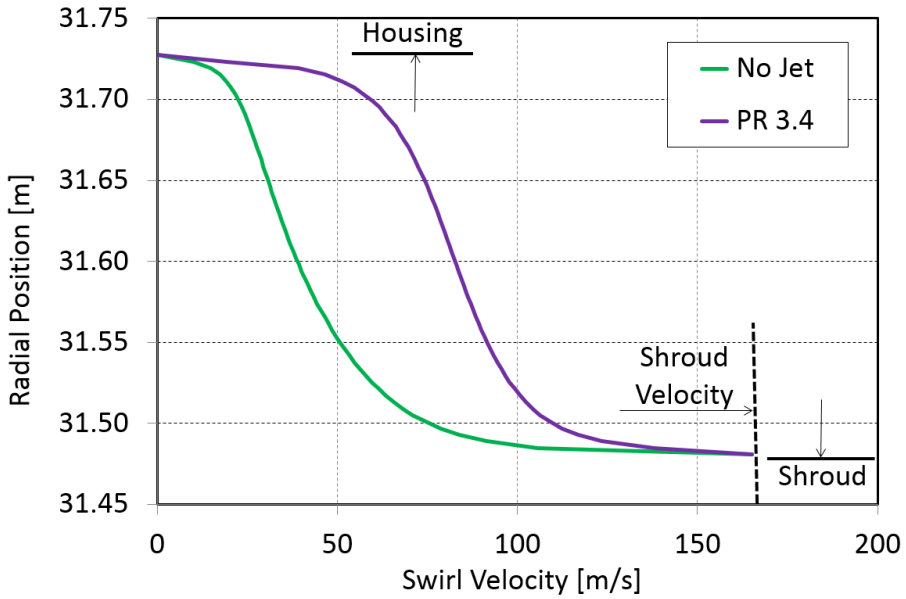

Figure 4.9: Radial Profile of Swirl Velocity Across the Leakage Path at 50% of the Axial Distance Along the Shroud.

The impact of shroud shear is significant when quantifying the performance benefit from the improved sealing. Figure 4.10 shows the total rotor power output improvement due to the fluidic seal, extracted from the same calculation data set as used for Figure 4.7.

The power gains shown in Figure 4.10 were calculated assuming, that a 1% reduction in stage flow leaking through the rotor tip seal, would yield a 1% improvement in stage power, without the power change due to the shroud shear force effects described above. Figure 4.10 shows that the conditions that produced the largest leakage mass flow reductions in Figure 4.7 resulted in a net increase in rotor power of around 450W for this application. This compares with a total rotor power output (no jet case) of approximately 12.5 kW. So, the shroud shear effect (80 W noted earlier) could increase the power gains from a fluidic seal by approximately 20%.

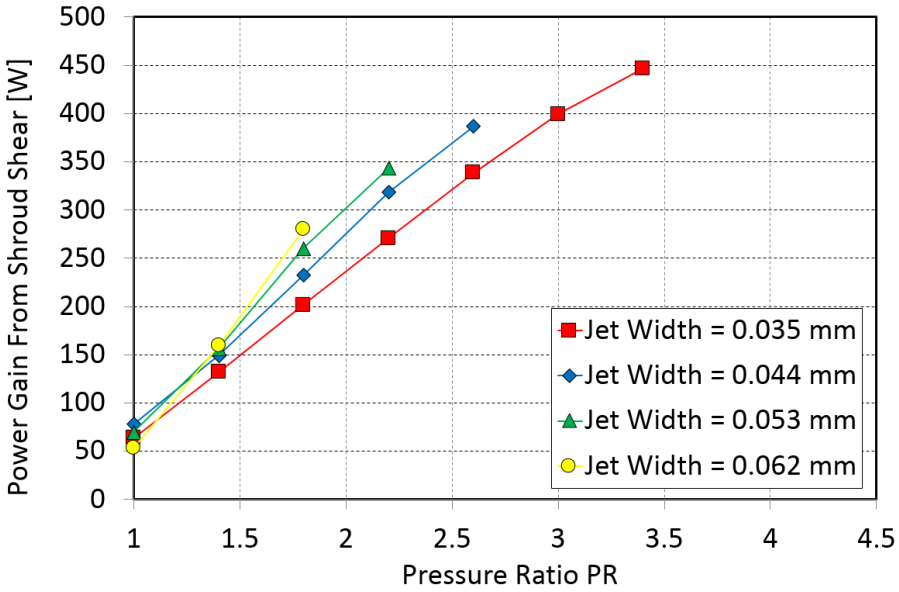

Figure 4.10: Net Power Gain (Extra Power due to Reduced Leakage plus Shroud Shear Forces) for Jet Angle 45° & Distance from Corner = 0.500 mm.

The data shown in Figure 4.10 was plotted as a percentage of the total stage power output from Figure 4.11. The figure shows, that the net power gain of 450 W translated to an improvement in output power of approximately 3.5% for the turbine design in this application.

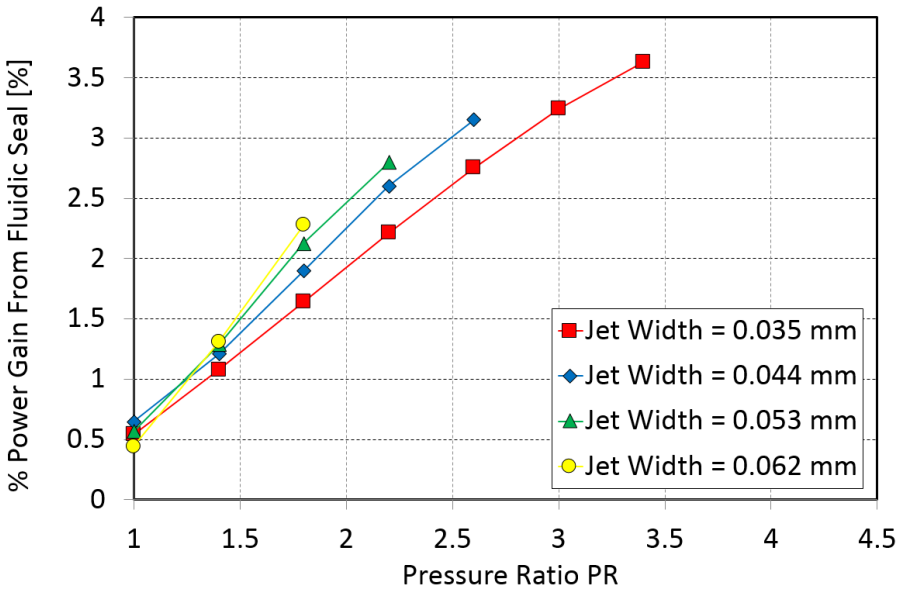

Figure 4.11: Net Power Gain from the Fluidic Seal as a Percentage of Turbine Power for Jet Angle 45° and Distance from Corner = 0.5 mm

4.3.2 Effect of Jet Angle and Location of Jet on the Performance of the Fluidic Seal

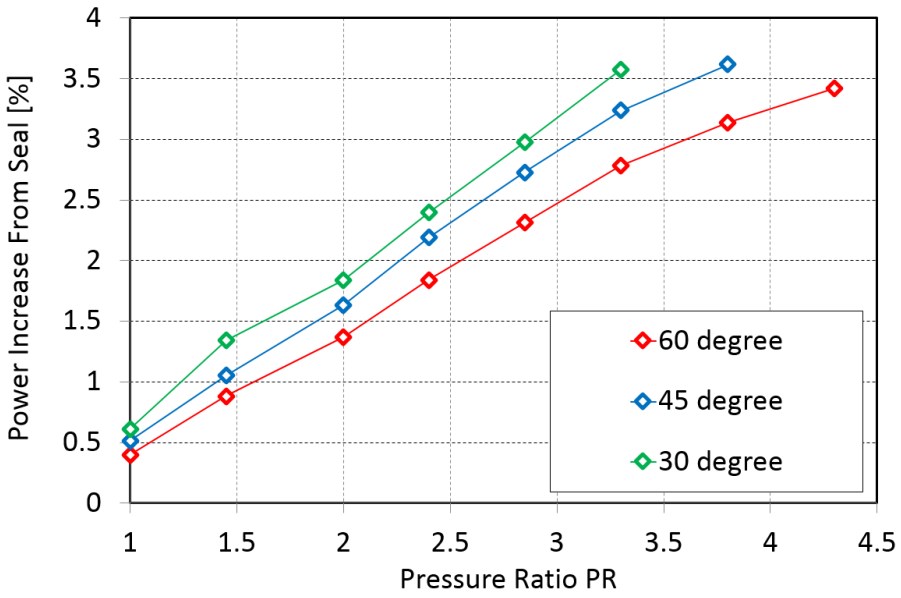

Figure 4.12: Effect of Jet Angle on Power Output for Jet Width = 0.035 mm and Distance from Corner = 0.5 mm

The effect of the jet angle on stage power output is shown in Figure 4.12 for the narrowest jet width calculated (0.035 mm) positioned 0.500 mm from the corner of the shroud cavity. Results are shown for the 3 values of the jet angle, given in Table 4.3. Once again, results are shown in Figure 4.12 for values of PR up to the jet pressure ratio where the seal becomes overblown (Mode 3). With decreasing angle (see Figure 4.6 for definition of angle) in the calculations, the proportion of the jet momentum directed against the shroud leakage flow increases. The increase of the momentum against the leakage flow, increases the effectiveness of the jet in creating a blockage, reducing the leakage mass flow rate and consequently increasing the turbine power output. The increase in the effectiveness of the jet to create a blockage with smaller jet angles at a similar pressure ratios is explained by the ability of the jet to traverse a greater part of the leakage passage in the radial direction, before being aligned with the leakage flow. In general, for any given jet pressure ratio, the improvement in power output from decreasing the jet angle from 60° to 45° was greater than that for the change from 45° to 30°. The results suggest diminishing returns for the benefits to be gained from designing very low jet angles, which were also likely to present greater

manufacturing challenges. The fluidic seal becomes overblown at a lower value of jet pressure ratio, as the jet angles decrease. The data in Figure 4.12 shows, that it was possible to achieve turbine power outputs improvements of approximately 3.5% with all of the jet angles calculated. So, moving to a lower jet angle of 30° does not improve the absolute performance benefit that can be gained in this application, it simply allows that improvement to be achieved at a lower jet supply pressure.

In the present application, the fluid supplying the jet is assumed to be extracted from upstream of the turbine stage and throttled down to the desired jet supply pressure. Therefore, the maximum jet supply pressure that is available in the current application is the turbine stage inlet pressure (i.e. no throttling of the flow supplying the jet). Under these conditions, the jet pressure ratio (PR), as defined by Equation 4.1, became approximately equal to the reciprocal of the turbine stage reaction (Equation 4.3, Figure 4.13) as shown in following Equations.

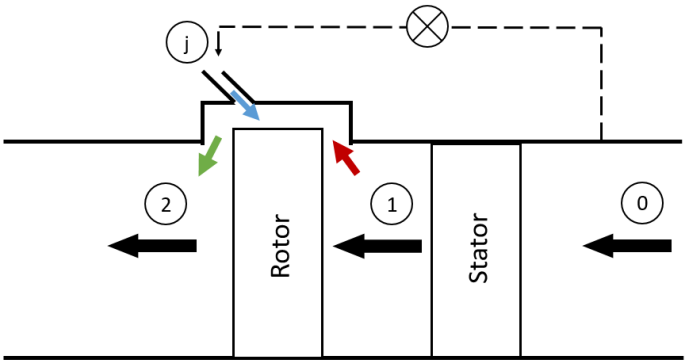

Figure 4.13: One Stage Turbine

$$PR = \frac{p_j - p_2}{p_1 - p_2} \tag{4.1}$$

$$R = \frac{h_1 - h_2}{h_0 - h_2} \tag{4.2}$$

If $p_j = p_1$ (no throttling case), then

$$PR = \frac{p_0 - p_2}{p_1 - p_2} = \frac{1}{R} \tag{4.3}$$

The turbine is a low reaction impulse design (nominal 3% reaction, see Table 4.1) and so it is possible to achieve values of PR that were several times greater (i.e.

$PR = 1/0.03 = 33$) than the maximum value 5 of PR shown on the horizontal axes in Figures 4.7 - 4.14. So, for this application, it was not necessary to minimise the value of PR at which the seal becomes over-blown, because it was possible to achieve values of PR much greater than required for this application. For these reasons, a jet angle of 45° was selected as the angle for the present design. This resulted in a slightly higher value of PR needed to achieve best overall leakage reduction, compared to that of a lower angled jet with a greater counter-leakage flow velocity component.

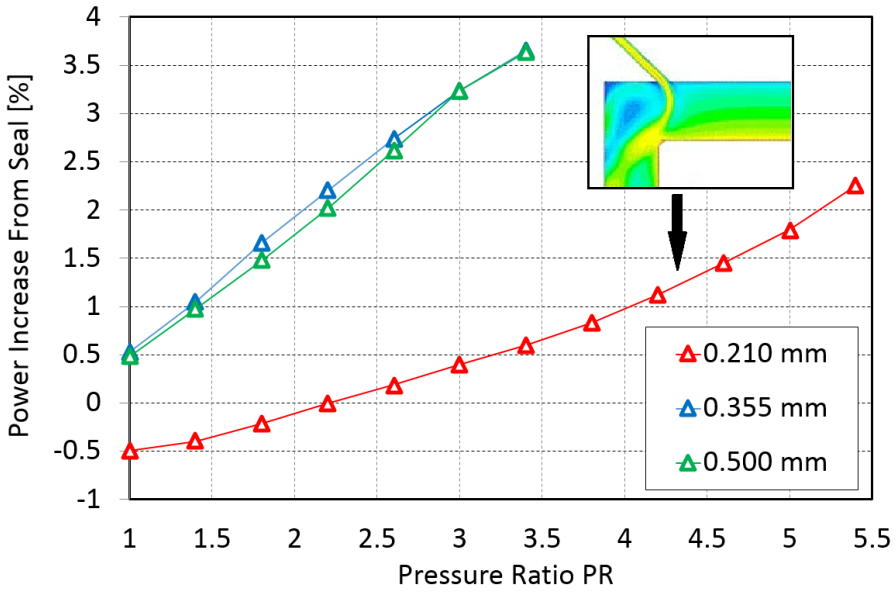

Figure 4.14: Effect of Jet Location (Distance from Corner of Leakage Cavity) on Power Output for Jet Width = 0.035 mm and Angle = 45 °

Figure 4.14 shows the influence of varying the axial distance (c) of the jet entry point relative from the downstream corner of the shroud seal cavity (see Figure 4.6). The results shown in Figure 4.14 were calculated for the narrowest jet width considered in the study (0.035 mm) and a jet angle of 45°. Three jet positions are compared in Figure 4.14 . The variation of the output power increase with pressure ratio (PR) is similar for the cases where the jet is positioned 0.355 mm and 0.5 mm axial distance from the corner.

Quite different results can be observed, when the jet is positioned closer to the corner (axial distance = 0.210 mm). The performance improvement from the fluidic seal is greatly reduced in this case. For this particular case, at low values of PR the fluidic seal has a negative impact on the performance of the turbine compared to

the no-jet case. At higher values of PR there is a net benefit from the fluidic seal, but much higher values of PR are required to achieve performance gains compared to the other jet axial positions. Also, the maximum achievable performance gain is significantly lower with the seal in the closest position to the corner, compared to what is possible with the other jet locations. The CFD results reveal the principal difference between the flow structure in the c=0.210 mm axial distance case, compared to the other cases. The predictions show that if the jet is positioned too close to the end of the tip shroud, the deflection of the fluidic jet in the shroud leakage flow is such, that the jet flow does not impinge on the rotor shroud, and instead mixes with the radial leakage flow exiting from the tip seal (see Figure 4.14). It is imperative, that the fluidic jet impinges onto the surface of the rotor shroud, in order for the jet to create maximum blockage and to achieve the best performance gains. As long as this was achieved, the performance gains were similar, as shown by the c=0.355 mm and c=0.5 mm axial distance results in Figure 4.14.

It was desirable to position the fluidic jet axially closer to the seal exit than the inlet, in order to minimize the work done by the shroud shear forces in accelerating the swirl velocity component of the jet fluid. There have been some variation in relative axial positioning between the rotor and the casing due to manufacturing and assembly tolerances during operation. This also needed to be taken into account when designing the seal. For these reason the axial position of c=0.500 mm was selected for the current design.

The finding from the CFD investigations on the distance of the jet from the corner (c) presented in this section are comparable to the results from the investigations of fluidic seal in Chapter 3. Where in Chapter 3 a kinetic energy blocker is used to reduce the kinetic energy carry-over and to stop the jet from entering the downstream situated labyrinth seal unrestricted, here the downstream axial restriction acts in similar function, also reducing the kinetic energy carry-over by turning the jet and creating additional blockage and recirculation. In the case of c=0.210, the jet is blown directly into the restriction carrying the majority of its kinetic energy downstream of the seal.

In summary, the optimization process resulted in the selection of the seal parameters shown in Table 4.4 for the fluidic seal design developed in this study. The jet

would be supplied with fluid bled from upstream of the stage and throttled to a maximum jet supply pressure ratio (PR = 3.0). This allows some margin before the seal became over-blown. Under these conditions, the CFD simulations indicated, that the fluidic seal would improve the output power from the turbine unit by just over 3%.

Table 4.4: Selected Parameters for Manufacturing.

Jet Angle (α)	45°
Distance from Corner (c)	0.5 mm
Jet Width (th)	0.035 mm

4.3.3 Turbo Expander Unit Modification

Using the design parameters from the optimisation process, the turbo expander unit was modified to accommodate fluidic sealing.

4.3.3.1 Modifications of Expander Unit Housing

The modifications of the Expander Unit housing were carried out on a lathe by widening the original seal geometry up to the outlet diameter, as shown in Figure 4.15. Additionally a jet supply cavity was machined into the housing to ensure continuous jet fluid supply. Further, an o-ring groove was added to create a seal between he housing and the fluidic seal insert. The fluid to the jet cavity was supplied through a port in the housing and with additional port the pressure inside the jet cavity was measured.

4.3.3.2 Fluidic Seal Inserts Design

The fludic seal inserts (H1 and H2 in Figure 4.16) were designed according to the specifications from optimisation effort described in sections above to fit the radial gap between the modified expander unit housing on one side and the rotor and stator on the other side and to re-create the original leakage path geometry without the labyrinth seal cavities. The jet gap was created between the inserts using shims of required thickness evenly distributed along the circumference on the jet gap surface

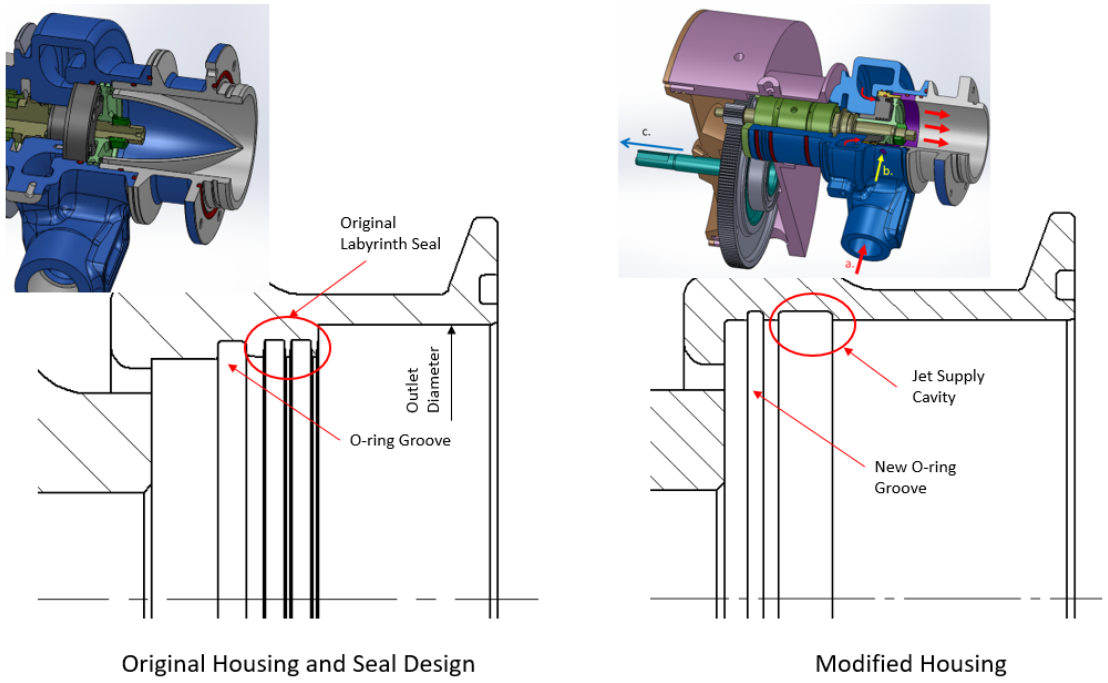

Figure 4.15: Modifications of the Original Housing and Seal Design

of the insert H1 (Figure 4.17). The inserts also featured o-ring grooves and with appropriate o-rings so that all parasitic flows inside the fluidic seal assembly were eliminated. The fludic seal inserts were also designed to be easily extracted in the axial direction for possible replacement or maintenance between the tests without the need of disassembling of the complete expander unit assembly. The smallest manufacturable jet angle of 45° was selected. Smaller angles were not possible due to the manufacturability constraints with the equipment available and the possibility of deformations during seal assembling and operation.

4.4 Conclusion

The design of a fluidic type seal for an application, as a rotor tip seal on a small high-speed single stage axial flow turbine, was described. The CFD methods were used together with automated scripts and automated mesh generation to optimize the design of the fluidic jet. The results showed that it was important to make the jet width as narrow as possible (manufacturing constraint) and that the performance gains yield diminishing returns as the jet angle became increasingly acute (45° is a

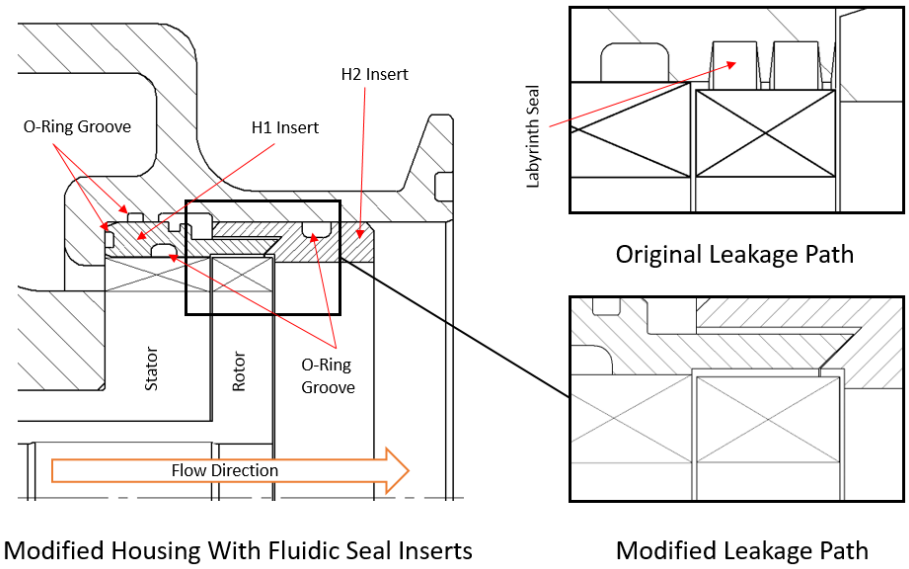

Figure 4.16: Fluidic Seal Inserts H1 and H2 in Modified Seal Assembly

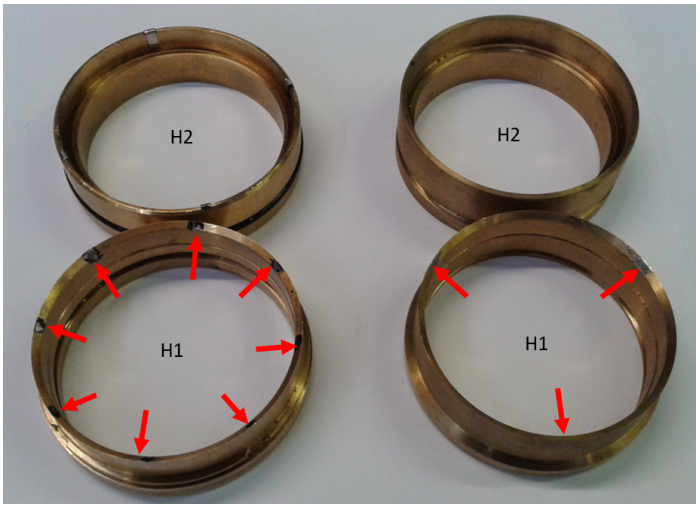

Figure 4.17: Fluidic Seal Inserts, Mk4 left and Mk3 right, with shim positions on the jet gap surface of insert part H1 indicated

good compromise). The jet was positioned axially towards the downstream end of the rotor shroud cavity, but not so close, so that the deflected jet fails to impinge on the rotor shroud. The CFD calculations showed, that the effect of the shroud shear forces was significant and must be taken into account when evaluating the net performance gain from the improved sealing. Overall for selected design parameters for the fluidic seal are shown in Table 4.4. The CFD calculations predicted an output power improvement of just over 3% from applying the fluidic seal including the effects

on shroud shear.

Using the fluidic seal parameters from the optimisation results, the original turbo expander unit was modified to incorporate the new fluidic seal design.

Chapter 5

Static testing of the Turbo Expander Fluidic Seal Design to Demonstrate the Leakage Reduction Potential - "Mosquito" Tests.

The aim of these experiments was to validate the selected fluidic seal design as described in Chapter 4 by directly measuring the effect of the fluidic jet on the leakage flow over the rotor shroud without the added complexity of rotation and all of the accompanying additional secondary leakage flow paths that are present in the Cummins Turbo Expander Unit. For this purpose a new experiment codenamed "Mosquito" was designed to include exact flow path geometries of the modified turbine (Section 4.3.3) and to accommodate the original rotor and stator as well as the new seal components excluding rotating motion. Further, the implementation of refrigerant supply system was not possible due to a need of complicated contamination system and the high refrigerant costs, therefore already existing blow down test facility operating with compressed air was used for this and following tests. The following work formed the basis of the ASME conference paper Hilfer et al. [31].

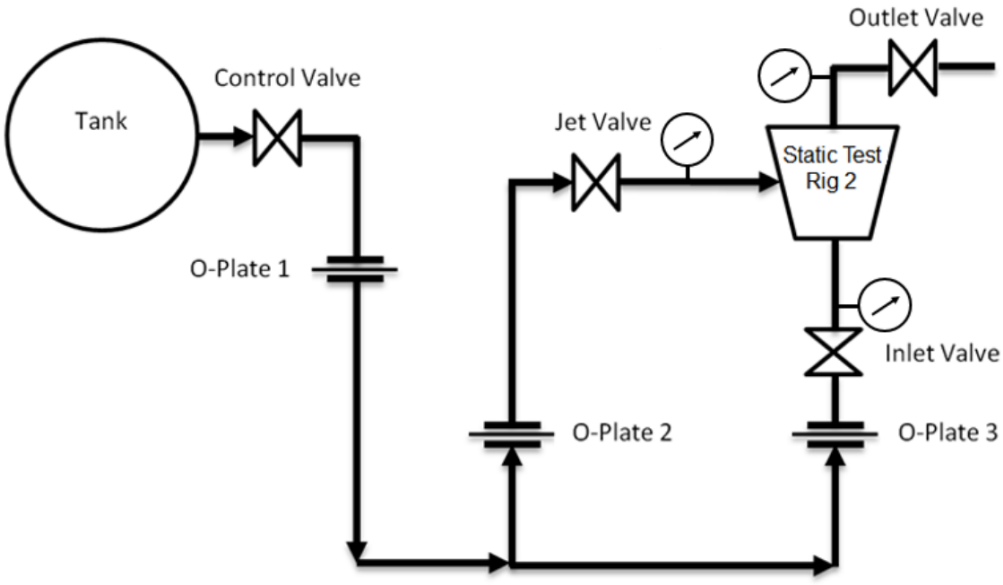

Figure 5.1: Position of Mosquito Experiment in Blow Down Facility

5.1 Static Rotor Stage Test Facility - "Mosquito" - Experimental Set up

As shown in Figure 5.1, the static rotor stage test facility (Mosquito), was integrated in the Durham Blow Down Facility (a description of the Durham Blow Down Facility is given in Section 3.3.1). The air flow to the turbine inlet was supplied through the Orifice Plate 3 (O-Plate 3) with following Inlet Valve controlling the turbine inlet pressure. The mass flow supply for the fluidic seal jet passed through the Orifice Plate 2 (O-Plate 2) with jet pressure controlled by the Jet Valve. The Mosquito outlet pressure was precisely controlled by the Outlet Valve. Additionally the combination of turbine inlet mass flow rate and jet mass flow rate was measured by the Orifice Plate 1 (O-Plate 1) and was considered the actual outlet mass flow rate.

5.1.1 Hardware

In Figure 5.2, a section view of the Mosquito experiment is shown with encircled P identifying the pressure measurement points. The Mosquito experiment was designed to accommodate both the original stator and rotor components of the Turbo Expander Unit and to exclude the rotational motion, making it comparable to the first static experimental rig as described in Section 3.4. The Mosquito hardware was designed to

be modular and to allow measurement of gaps and distances which were not accessible in a rotating facility.

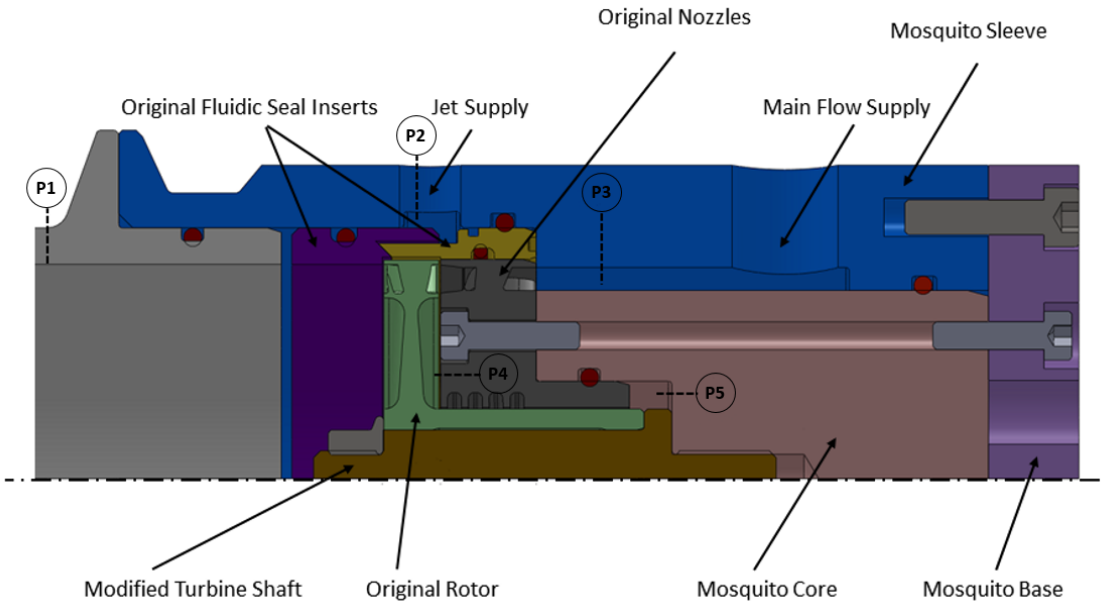

Figure 5.2: Section View of the Mosquito Experiment with (P) Indicating the Pressure Measurement Locations.

As shown in Figure 5.2, the Mosquito experiment consisted of the following components:

- **Mosquito Base** was the element of the hardware to which all other components were mounted. The Base additionally provided ports for temperature and pressure measurements between rotor and stator.

- **Mosquito Core** was precisely machined to ensure, in combination with the Modified Turbine Shaft, a precise axial gap of 0.25 mm between the Stator and Rotor shrouds. The Modified Turbine Shaft was located in the Core using a left handed thread, so that during the test, the forces generated by the flow passing through the turbine buckets, further tightened the shaft into the Core.

- **Mosquito Sleeve** Additionally to ensuring a precise location of the Fluidic Seal Inserts, the Sleeve was designed to ensure a continuous supply of the turbine inlet flow as well as the fluidic jet flow. The four ports for each of the supplies

(turbine inlet and fluidic jet) were located circumferentially equidistantly distributed at locations as identified in Figure 5.2. Furthermore, circumferentially distributed pressure tapings were located on the Sleeve for Jet Cavity pressure measurement and Stator Inlet Pressure measurement.

- **Modified Turbine Shaft** featured similar design to the original turbine shaft and was manufactured to minimise radial displacement of the rotor relative to the stator as well as to be able to precisely set the axial gap between the rotor and stator shrouds using shims between Base of the rotor and the Core.

- **Original Nozzle and Rotor** were the original expander unit components with original geometry supplied by the manufacturer.

- **Fluidic Seal Inserts** were build to create a jet with precise jet gap size and jet angle. Fluidic Seal Inserts are introduced in Chapter 6.

- **Pipe Connector** was, together with the Nozzle and Rotor, the original part supplied by the manufacturer and was used to connect the Mosquito experiment to the exhaust pipe. The whole experiment assembly was suspended from the Pipe Connector.

The pressures in the experiment were measured at 3 positions (Figure 5.2) employing 4 pressure tappings at each measurement position distributed equidistant along the circumference. The pressure tappings for the stator inlet pressure (P3) were located 3 cord lengths upstream of the nozzle leading edge. The tappings for the jet inlet pressure (P2) were located inside the jet cavity and the outlet pressure tappings (P1) were located more than 200 rotor cord lengths downstream of the rotor outlet, so uniform pressure distribution was warranted. Additionally Mosquito featured pressure ports for measuring pressure between the stator and the rotor (P4) and the pressure between the stator and Mosquito core (P5).

During the test run the desired inlet and outlet pressures were maintained using valves at the inlets and the outlet of the experiment in combination with high precision analog gauges.

5.1.2 Instrumentation

The general instrumentation of the Blow Down Facility is outlined in Chapter 2. Below, the Mosquito specific instrumentations are described.

- **Stator Inlet, Jet Inlet and Rotor Outlet Pressure Measurements** were carried out using ScaniValve "DSA3217 Pressure Scanner" [54]. The ScaniValve was accurate to 0.05% full scale for a range 0 bar to 6.8 bar. To minimise a random error, for each data point, 800 samples were taken and averaged at a sampling frequency of 400Hz. The ScaniValve module delivered values in engineering units.

- **Turbine Inlet Temperature** was measured as described in Chapter 2 in the upstream pressure receiver. **Turbine Outlet Temperature** was measured using a K-Type thermocouple situated next to the outlet pressure tapping. The thermocouple voltage was amplified and logged parallel to other measurements using National Instruments (USB6218) logging card and processed using Durham Software for Wind-tunnels.

- **Manual Pressure Gauges on Turbine Inlet/Outlet, Jet Inlet** are shown in Figure 5.1 and were used in combination with the manual globe valves to set required pressure on above mentioned locations.

5.1.3 Test Set-up and Procedure

For this and following tests the working fluid was switched from refrigerant to air. This greatly reduced the complexity of the fluid supply since no fluid containment and contamination prevention measures were needed for the experiment. The properties of refrigerant and air differ and so differences in turbine flow (e.g. rotor relative flow inlet angle) are expected. Changes to the flow structure through the turbine stage are not expected to have a significant impact on the performance of the rotor tip seal with the fluid curtain described in the previous chapter. The experiments described in this chapter feature the tip seal geometry from the previous chapter, but with a static rotor with axial rotor inlet flow in addition to the switch in working fluid to air. One of the aims of this tests is to validate the fluid curtain tip seal performance

Table 5.1: Carried out Test Runs with Number of Measurement Points in Each.

Experiment	Test Runs	Measurement Points
No Jet Test	5	up to 15
Normal Test	30	up to 30
Blocked Rotor Test	12	up to 15

under the different rotor flow conditions, further demonstrating that the tip leakage flow reduction achieved by applying the fluid curtain is relatively independent of the stage flow for this turbine design.

Three sets of experiments on the Mosquito test rig are presented in this chapter, they comprise of:

1. No Jet Test - the jet supply was turned off to provide a baseline performance comparison.

2. Normal Test - the jet supply was turned on and a range of data points measured for a range of jet pressure ratios (PR).

3. Blocked Rotor Test - the rotor was blocked to provide a direct comparison to the 2D CFD calculations used to design the fluidic seal, as described in Chapter 4.

For each set of experiments a number of runs was carried out with several measurement points for different jet pressure ratios taken during each run as highlighted in Table 5.1.

Initially the "Mosquito" experiment was designed to investigate the full turbine stage with nozzle and buckets included. During the investigations, the rotor inlet pressure at the blade tip in the shroud leakage flow inlet region needed to be accurately measured in order to calculate the pressure ratio parameter (PR as defined in Section 3.1.2), used to analyse the data. It was not possible to install a pressure tapping in the "Mosquito" experiment to directly measure the pressure at this location. The strong swirl in the flow between the rotor and the stator resulted in a radial pressure gradient across the rotor inlet flow which also indicated that the pressure measured

at the position (P4) in rotor disc cavity, shown in Figure 5.2, was different to the pressure at the rotor blade tip. Therefore, the stator was removed in all of the following "Mosquito" experiments described in this chapter. This enabled the static inlet pressure in the shroud leakage flow inlet region to be measured from the taping in the main inlet channel shown in Figure 5.2 upstream of the stator location.

The Turbo Expander Unit stage was a low reaction impulse type axial stage and therefor, most of the stage pressure drop occurred across the stator. With the stator removed it was only necessary to test at relatively low values of rotor pressure ratio (ca 8.5 kPa) in order to simulate realistic rotor pressure drop conditions. The air flows in the "Mosquito" experiments were therefore essentially incompressible. The selection of the rotor pressure drop was based on two assumptions: Firstly, assumed stage reaction of approximately 3% and secondly, that during a normal operation of the Turbo Expander Unit the nozzles had to be choked, which required a nozzle inlet/outlet pressure ratio of less than 0.528.

The CFD calculations carried out during parametric design as described in Chapter 4 predicted a reduction in rotor shroud leakage flow of up to 3% of the main stage flow, due to the effect of the fluidic jet seal. In the Mosquito experiment, it proved to be challenging to control and maintain constant stage inlet (P3) and exhaust pressures (P1) for different values of jet inlet pressure (P2), in order to validate flow reductions of this magnitude directly from the mass flow measurements. This was due to a very small pressure drop across the rotor relative to the high absolute inlet (P3) and outlet (P1) pressures which were set using manual valves and analog gauges.

A swallowing capacity or effective area A_{eff} parameter (defined below) was therefore used. This allowed the leakage reduction effect of the fluidic jet to be deduced from the experimental data collected in tests which had a range of inlet and outlet pressures.

5.1.4 Definition of Effective Flow Area (A_{eff})

The effective flow area A_{eff} is a measure of the total flow throat area through the rotor passages and the leakage passage combined.

Table 5.2: Flow Areas Determined From CAD Models.

Position	Area $[m^2]$
Single Rotor Passage	$7.01 \cdot 10^{-6}$
34 x Passages	$238.34 \cdot 10^{-6}$
Shroud Leakage Area	$49.28 \cdot 10^{-6}$
Rotor + Shroud Leakage	$287.62 \cdot 10^{-6}$

Effective flow area A_{eff} was defined as described in Equation 5.1. As discussed in the previous section, the flow in the "Mosquito" experiment was incompressible (with the stator removed). A_{eff} was therefore calculated by dividing the total mass flow exhausting from the test rig, by a constant flow density and a Bernoulli term for velocity. The effective flow area was normalized by a standard temperature and pressure inlet condition and a total discharge coefficient C_f was introduced in order to relate the effective flow area calculated from the flow measurements to the rotor geometry.

$$A_{eff} = \frac{\dot{m}_{outlet}}{\sqrt{2 \cdot \rho \cdot (p_{0in} - p_{out})}} \cdot \frac{1}{C_f} \cdot Norm \tag{5.1}$$

with

$$Norm = \frac{\sqrt{T_{0in}} \cdot p_{os}}{\sqrt{T_{os}} \cdot p_{0in}} \tag{5.2}$$

and

$$p_{os} = 400000 \quad [Pa] \qquad T_{os} = 300 \quad [K] \tag{5.3}$$

The geometrical flow area was estimated from CAD model of the Turbo Expander Unit rotor and casing. The throats of the rotor blade passages occurred at their trailing edges, as shown in Figure 5.3.

The rotor had a total of 34 blade passages. The area between the outer surface of the rotor shroud and the casing (Figure 5.4) was also determined from the CAD models. The areas deduced for the CAD models are shown in Table 5.2.

Three different types of investigation were carried out using "Mosquito". These are described briefly in each of the result sections below. The first set of tests was

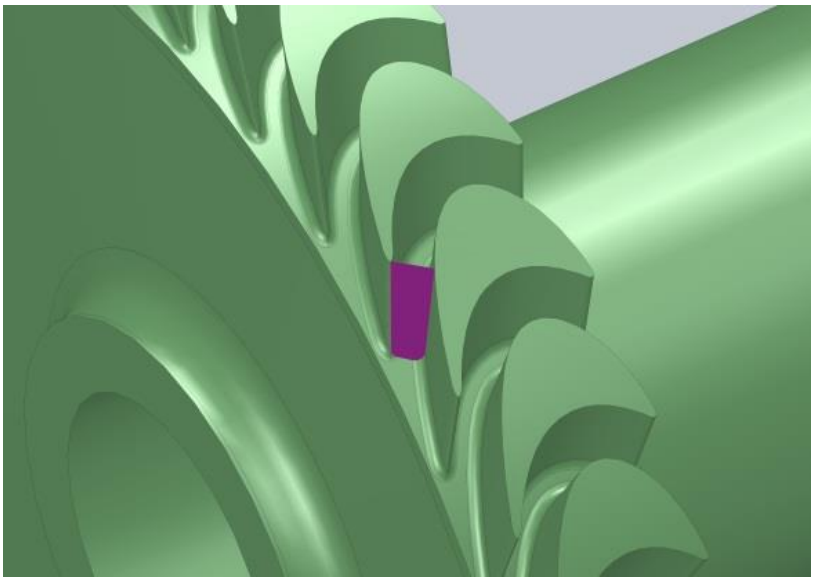

Figure 5.3: CAD Model of the Rotor Without Shroud Shown and Throat Area Indicated In Purple.

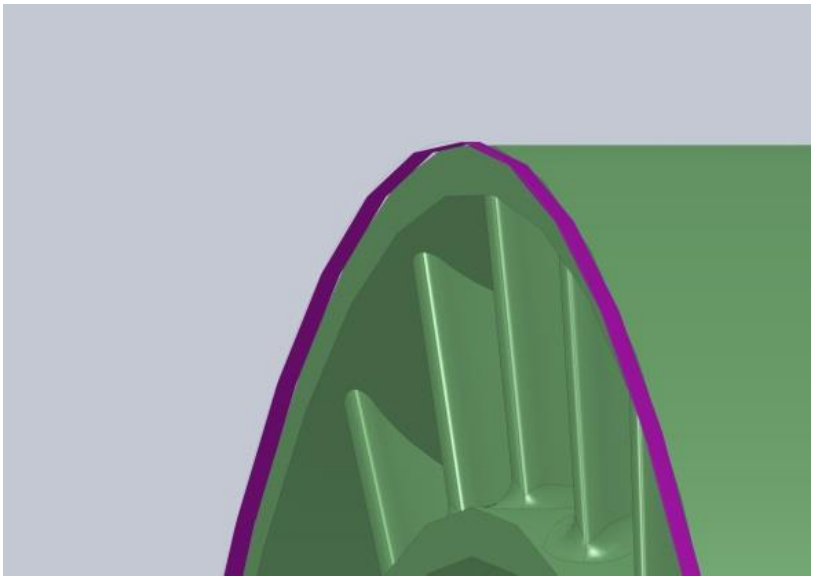

Figure 5.4: CAD Model of the Rotor With Shroud and Leakage Flow Restricting Area Indicated in Purple.

carried without any fluidic jet flow present. These tests allowed a value of C_f to be determined from the flow measurements, by matching the calculated value of A_{eff} to the flow area (Rotor + Shroud Leakage) calculated from the CAD models given in Table 5.2.

5.2 Experimental Results

5.2.1 No Jet Test

The fluidic jet was left turned off during the first set of tests carried out on the "Mosquito" experiment. The mass flow rate through the rotor was measured for a range of pressure drops across the rotor. These results were used to determine a value for C_f and to investigate, whether there was any variation in A_{eff} (in the ideal case A_{eff} would be constant) across a range of values of the pressure drop which was tested.

The Inlet pressure was kept constant during these tests and the pressure drop across the rotor was changed by varying the rotor outlet pressure by adjusting the outlet valve (see Figure 5.1).

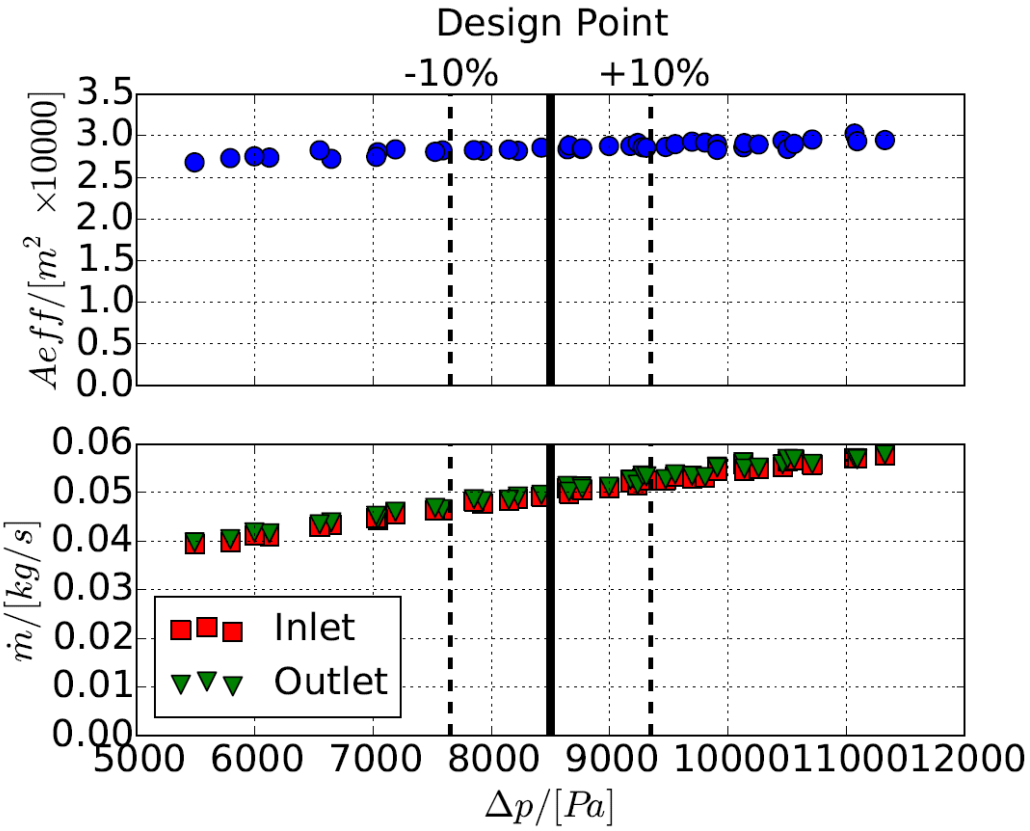

Figure 5.5: Result for No Jet Test with Effective Flow Area A_{eff} and Mass Flow Rates $\dot{m}$ plotted against a Wide Range of Rotor Pressure Drop around Design Point of 8500 [Pa].

The results obtained from the tests are shown in Figure 5.5. The pressure drop

(Δp) across the rotor at nominal design operating conditions was 8.5 kPa. Tests were carried out over a range of rotor pressure drops 5.5 kPa $< \Delta p <$ 10.5 kPa. The increase in mass flow rate through the rotor over this range of pressure drops is shown in the lower chart in Figure 5.5.

The flow coefficient, C_f , was selected so that $C_f = 0.58$ allowed the calculated value for A_eff to match the throat area value of $287.62 \cdot 10^{-6} m^2$ extracted from the CAD models and shown in Table 5.2. The comparable flow coefficients for a generic orifice plates at similar flow conditions ($C_f \approx 0.6$) ensured a confidence, that the values for A_{eff} calculated from "Mosquito" flow measurements were representative of the swallow capacity of the test rig. The upper chart in Figure 5.5 shows values for A_eff calculated from the test points across the range of Δp tested. Some variation in A_{eff} (indicating that C_f does vary slightly with Δp) can be seen in the data across the range, but this was small compared to the change in measured mass flow rate.

Results from tests carried out with the fluidic jet switched on are described in the next Section 5.2.2. For these tests the pressure drop across the rotor was kept within +/− 10% of the nominal design value ($\Delta p = 8.5$ kPa). The variation in A_{eff} across this range of Δp values is indicated in Figure 5.5. It can be seen that the variation in A_{eff} is of order +/− 2% across this reduced range of test conditions.

5.2.2 Normal Operational Conditions (Normal Test)

In this set a total of 253 tests were carried out and evaluated with the fluidic jet switched on. The measured mass flow rate data from all of these tests is plotted against the PR in Figure 5.6. The effect of the variation in Δp across the rotor can be seen from the considerable scatter in the inlet and outlet mass flow rate measurements. The data in the Figure 5.7 is a sub-set of the set of tests that has been filtered so that only tests where the rotor pressure drop was within +/− 3% of the nominal design rotor pressure drop have been plotted. Most of the scatter has therefore been eliminated in this reduced set of data. The chart in Figure 5.7 clearly shows, how the total mass rate through the test section (rotor inlet flow plus jet flow) falls as the strength of the fluidic jet is increased. This is the first experimental validation of the fluidic jet seal design described in Chapter 4 working and reducing the leakage over the Turbo Expander rotor shroud.

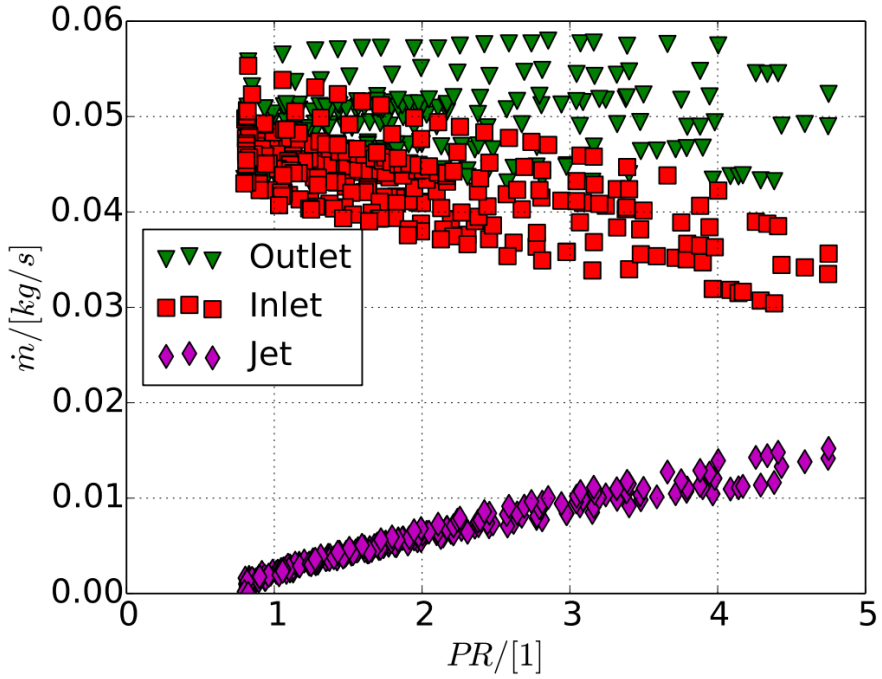

Figure 5.6: Mass Flow Rate During Normal Test For All Δp measured.

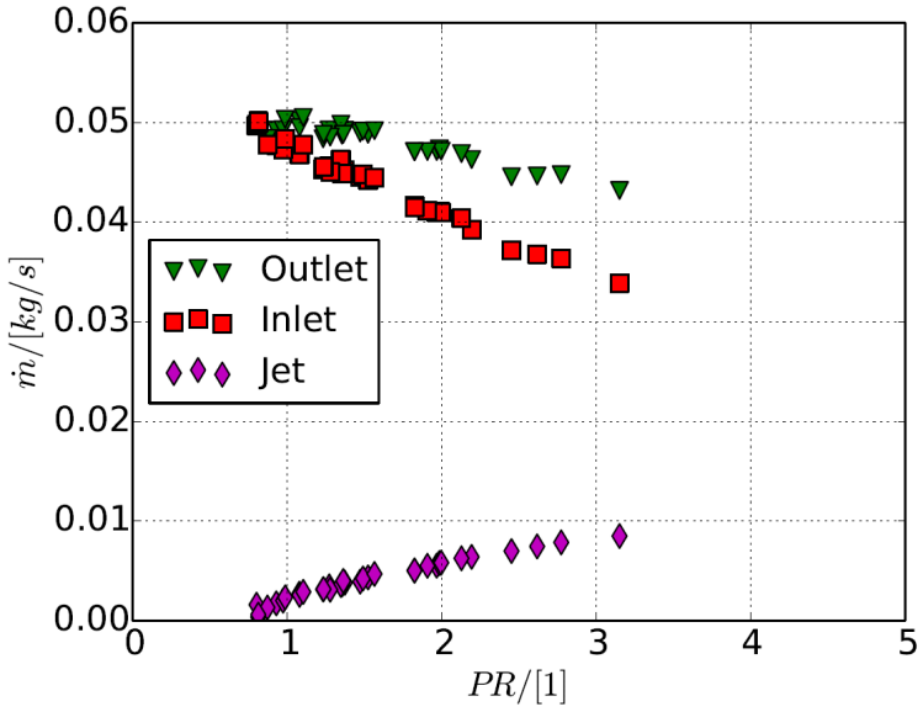

Figure 5.7: Mass Flow Rate During Normal Test For Δp Measurements Within 3% of 8500 [Pa].

The values for A_{eff} calculated from all 253 tests have been plotted against Pressure Ratio (PR) in Figure 5.8. As expected, plotting the data in this form brought about a significant reduction in the scatter compared to the results shown in Figure 5.6 and a clear trend of reducing A_{eff} with increasing jet strength (PR) is evident from the data. This provided further confirmation, that the fluidic jet acted to reduce seal leakage by creating aerodynamic blockage, which reduced the swallowing capacity of the test section. The reduction in A_{eff} from eliminating the shroud leakage path area given in Table 5.2 is indicated in Figure 5.8 by horizontal lines. This suggests that a jet pressure ration PR = 3.6 is need to reduce the swallowing capacity by this amount. This is likely though to be an over-estimation of the jet strength needed to reduce the shroud leakage flow to zero, because the true shroud leakage effective area will be influenced by the tight axial clearances at the inlet and exit to the shroud cavity and therefore a lower value would be expected than that calculated purely from a geometrical cross-section of the shroud leakage cavity given in Table 5.2.

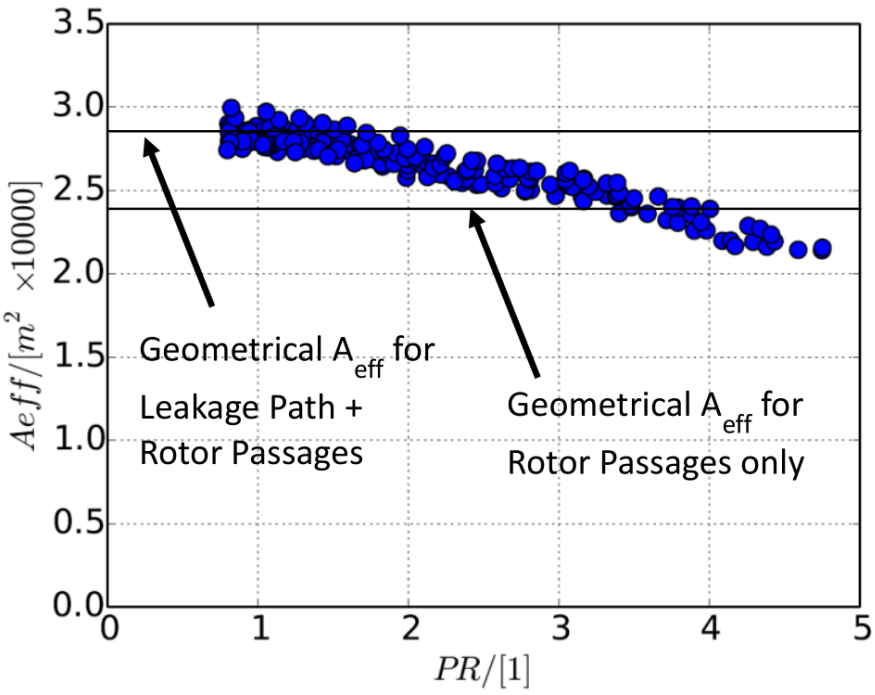

Figure 5.8: Effective Area Reduction During Normal Test.

5.2.3 Blocked Rotor Test

A final set of tests on Mosquito were carried out using a blocked rotor so that only shroud leakage flow was possible. The aim was to determine the value for jet pressure ratio (PR) at which the inlet flow into the shroud leakage channel was eliminated. The rotor in "Mosquito" was blocked using bees wax for the tests, as shown in Figure 5.9.

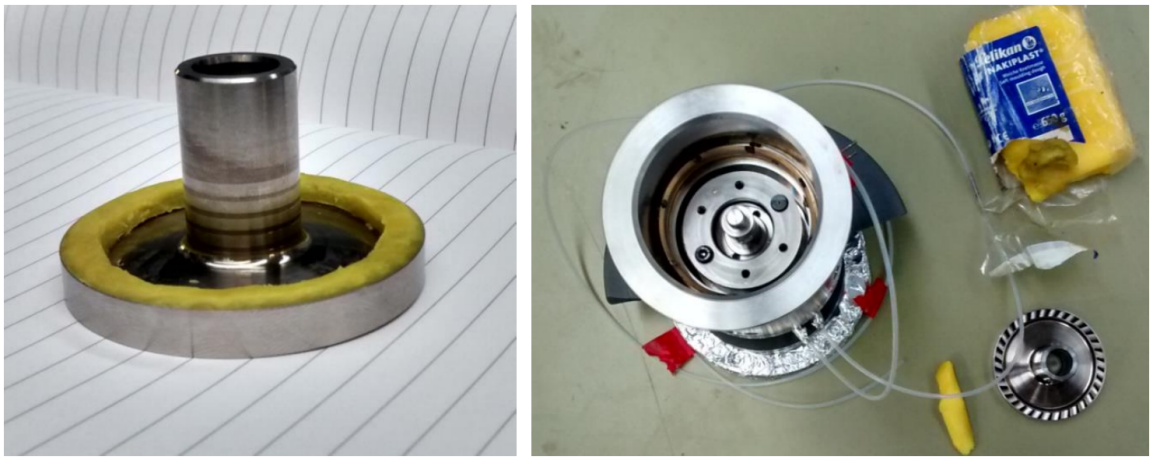

Figure 5.9: Blocked Rotor on the Left and Mosquito Assembly Without Stator on the Right.

The results from the tests are shown in Figure 5.10. Mass flow rate is plotted against pressure ratio PR. For any given rotor inlet total pressure and rotor exit static pressure, the static pressure at the inlet to the rotor tip shroud leakage path will be higher in the blocked rotor tests that it is when flow is allowed through the rotor due to the greatly increased flow velocity in the open rotor tests compared to the tests with the blocked rotor. This should be kept in mind when comparing the results in this section with those from the previous section with the open rotor.

The results in Figure 5.10 show a similar behavior to those described earlier in Section 3.4 (Figure 3.22 and Figure 3.23) for the first Static Test Rig experiments. The results in Figure 5.10 show the same initial gradual reduction in total (outlet) leakage flow as the jet pressure ratio increases, which then becomes a more rapid reduction with increasing pressure ratio PR at the high values tested. It is assumed that the same flow mechanisms are responsible for the trends observed in Figure 5.10 compared to the earlier tests, i.e. for low values of PR the jet is unable to penetrate

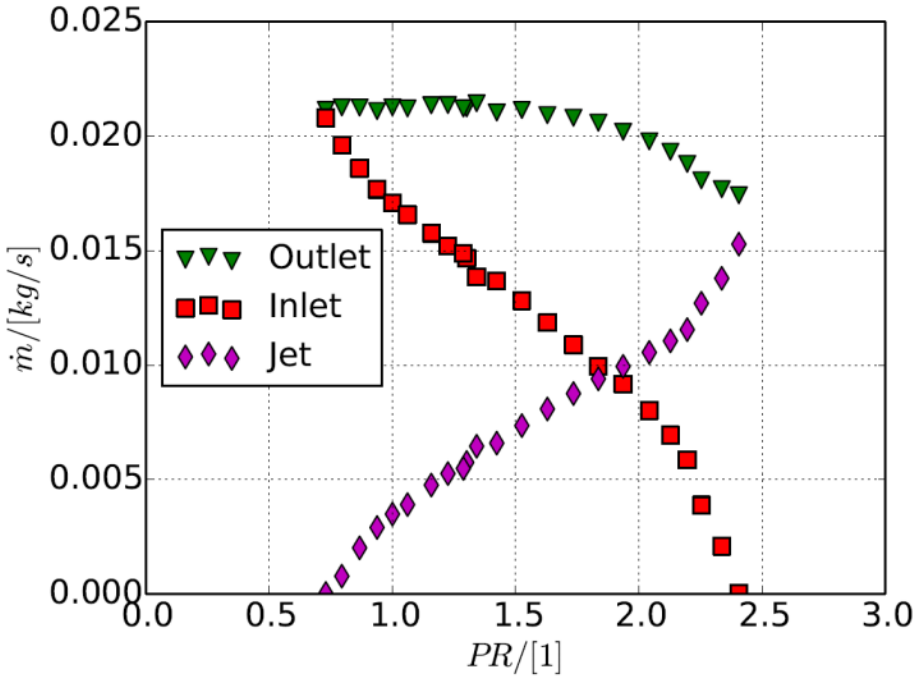

Figure 5.10: Mass Flow Rate During Blocked Rotor Test.

fully across the leakage flow and imping on the rotor shroud surface whereas in the higher PR tests this does happen and the effectiveness of the fluidic jet in creating blockage increases accordingly.

The shroud seal becomes over-blown (Mode 3) i.e. the inlet flow is reduced to zero and at the point of reversing at PR = 2.5. The experiments showed an overall net leakage flow reduction at this point of 25% less than the leakage with the jet turned off. The blocked rotor tests therefore provide further evidence of the effectiveness of the fluidic jet in delivering significant overall net leakage flow reduction when applied to the Turbo Expanders rotor shroud using the design that has been proposed in this study.

Furthermore the Figure 5.11,where the effective area (or swallowing capacity) A_{eff} of the blocked rotor test is plotted against jet pressure ratio PR, illustrates a reduction of a effective flow area A_{eff} of 32% corresponding to the net leakage flow reduction.

5.3 Conclusion

The curtain type fluidic seal as introduced in Chapter 4 has been designed and built for a single stage axial flow turbine. As a precursor to a full rotating tests a test

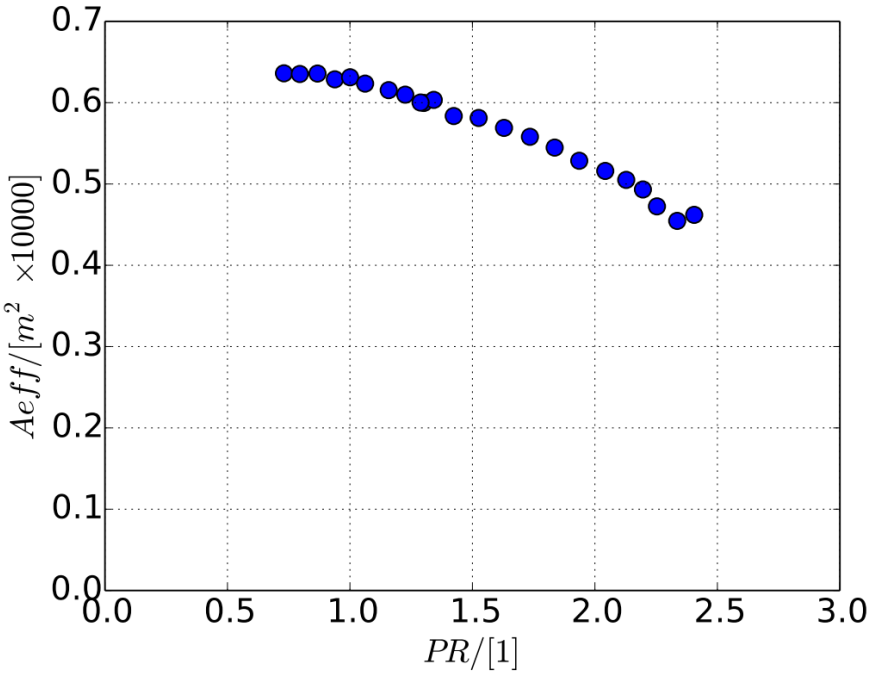

Figure 5.11: Effective Area During Blocked Test.

campaign on three simplifications of the turbine geometry have been conducted in the Durham Blow-down test facility operated with compressed air. These tests included:

- No-Jet test to validate the performance metrics, such as the flow coefficient C_f used to calculate effective area A_{eff}. The test showed with constant $C_f = 0.58$ only a relatively small variation in effective are A_{eff} across reduced range of test conditions around the operational point of $\pm 2\%$.

- Normal test, where the turbine geometry was tested excluding stator flow and without the rotation and the bearing chamber leakage flow. A range of tests at slightly different conditions were carried out and evaluated with results showing a 4% reduction in combined mass flow rate through the rotor and leakage path as well as 4% reduction in overall effective area up to a maximum jet pressure ratio where flow reversal occurs.

- Blocked rotor test to replicate the environment in which the seal was designed in Chapter 4. Here the leakage path mass flow rate was evaluated with jet supply switched off followed by gradually increase in jet seal flow. The experiment

showed an overall net leakage reduction of 25% similar to the results obtained in Chapter 4.

A performance metric: effective area A_{eff} was proposed to determine the success of the fluidic seal. This metric was shown to be largely independent of pressure drop across the turbine. The fluidic seal was shown to reduce the leakage flow-path area by up to 32%. This Chapter and associated publication Hilfer et al. [31] presented a first experimental validation of a curtain type fluidic seal design from Chapter 3 in a turbine geometry.

Chapter 6

Fluidic Seal Tests on a Rotating Facility.

One of the aims of the research project was to demonstrate the performance of a fluidic type seal in a full rotating test applied to a small commercial full scale Turbo Expander Unit as introduced in Chapter 4 and successfully tested on a static test facility "Mosquito" as described in Chapter 5. The new rotating test facility was designed and integrated into the Durham Blow Down Facility and operated with air as a working fluid.

6.1 Experimental Set-Up

Figure 6.1 shows a schematic diagram of the Rotating Rig integrated into Durham Blow Down Facility. The configuration shown differs compared to the Static Test Facility 2 "Mosquito" through introduction of rotation. Similar to the "Mosquito" experiment, the air supplying the turbine and generating the jet curtain was supplied operating the Blow Down Facility at different pressure levels up to a maximum of 15 *bar*. The mass flow rates measured were: Orifice Plate 1 (O-Plate 1 in Figure 6.1) the overall flow rate of air going into the engine, Orifice Plate 2 (O-Plate 2) the jet flow rate and Orifice Plate 3 (O-Plate 3) the overall mass flow rate leaving the engine.

6.1.1 Rotating Rig Hardware Components

The Cummins Turbo Expander Unit [27] used for this experiment was a prototype product for an application in an Organic Rankine Cycle system designed to extract

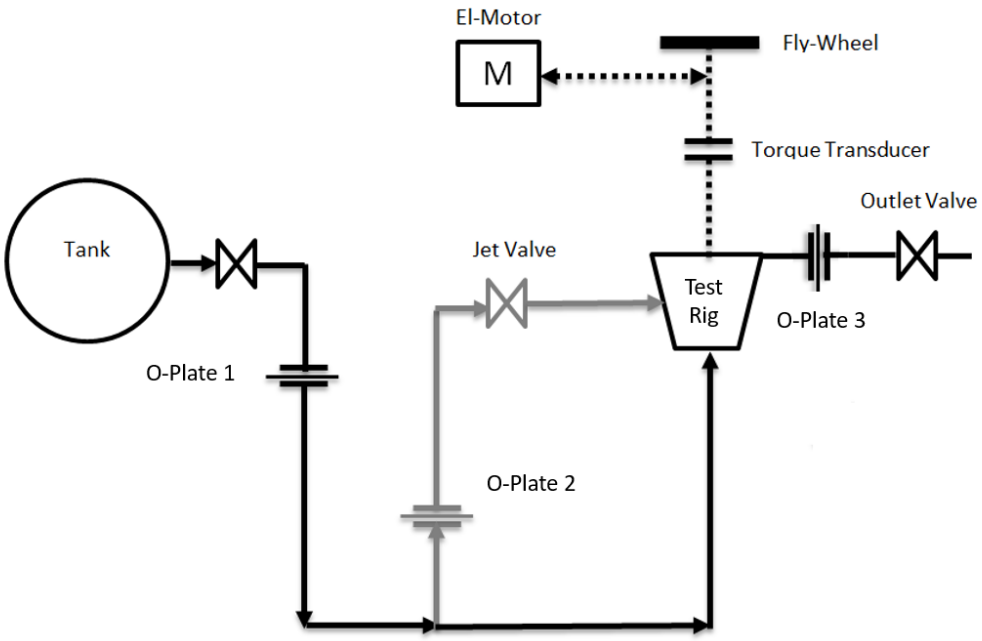

Figure 6.1: Schematic of the Rotating Rig Integrated in Durham Blow Down Facility.

residual heat energy from various sources in a vehicle. The turbo expander was a single stage impulse type axial turbine design.

As shown in Figure 6.2 the main flow was supplied into an inlet volute tangentially to the turbine exit flow direction (label 'a' in Figure 6.2). In the volute the flow was turned axially and evenly distributed circumferentially at the inlet to the nozzles. The flow was than subsequently accelerated and turned by the nozzles.

Under normal operational conditions the nozzles were choked, in which case the mass flow rate though the stage was governed by the pressure upstream of the nozzles. After leaving the stator nozzles the bulk of the high swirl and high impulse fluid was going through the rotor blade passages generating power. However, it was estimated that up to 3% of the fluid entered the leakage cavity between the rotor shroud and housing upstream of the rotor, bypassing the rotor but still influencing the power generation by a small amount through flow shear forces (Section 4.3.1). The leakage flow rate was estimated from results in Chapter 4 and Chapter 5 and turbine reaction test in Section 6.2.3. The power provided by the rotor was transmitted through a custom made 10:1 reduction gear box to the output shaft of the turbo expander / gearbox unit (label 'c' in Figure 6.2).

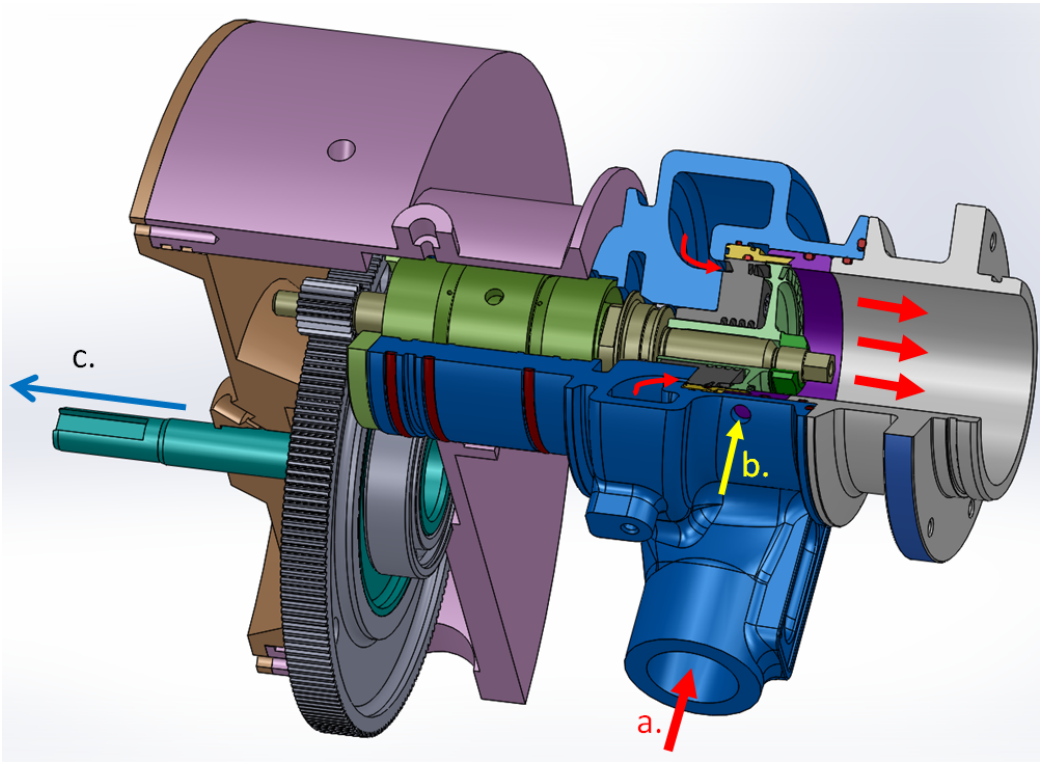

Figure 6.2: Cut Through Expander Unit Assembly Including Bearing Chamber and Gearbox with a. Indicating Main Flow Inlet and b. Fluidic Seal Flow Inlet as well as c. Slow Shaft Power Transmission Output.

Figure 6.2 shows a cut-through of the modified Turbo Expander Unit and gearbox with modifications to the seal implemented as described in Section 4.3.3. In the experiment the fluidic jet air was supplied through a single port through the housing of the Expander Unit (labeled 'b' in Figure 6.2). The jet pressure was also measured through a single port in the housing inside the jet cavity (Section 4.3.3) close to the jet air supply port. The possible jet supply and pressure measurement locations were restricted to a narrow section of the jet cavity by the volute covering most of the area.

Figure 6.3 shows the major shaftline components in the rotating facility:

I Turbo Expander Unit with modifications as described in Section 4.3.3.

II Gearbox, which was custom made and consisted of two gear wheels with a 10:1 reduction ratio. The fast shaft of the gearbox was connected to the Turbo Expander Unit and the slow shaft (c. in Figure 6.2) was connected to the following torque transducer.

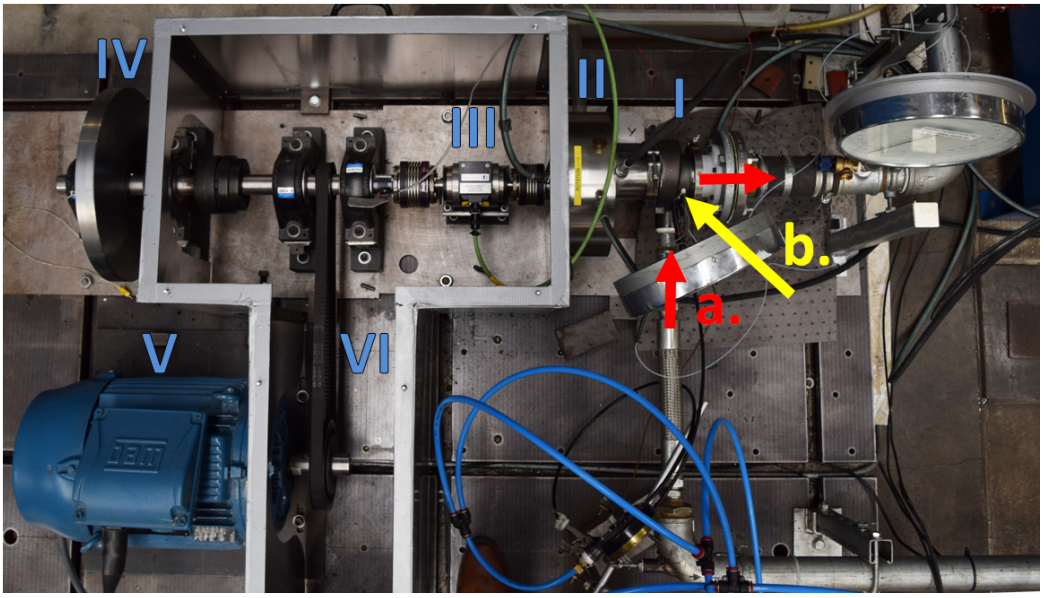

Figure 6.3: Rotating Rig Components: I - Turbo Expander Unit, II - Gearbox, III - Torque Transducer, IV - Flywheel, V - Electric Motor, VI - Synchronized Belt System. Turbo Expander Main Inlet a. and Fluidic Seal Inlet b.

III Torque Transducer used was a Magtrol Torquemaster TM 210, which was connected to the gearbox output shaft (dotted line in Figure 6.1 and c. in Figure 6.2) and the following component using flexible couplings. The torque transducer was used to measure torque as well as speed of the rotation.

IV Fly Wheel was added to the system to limit acceleration and deceleration of the system by adding extra inertia. Further, the fly wheel provided a dampening effect against high frequency rotational instabilities. The wheel was made of mild steel with 0.4 m diameter and 0.035 m thickness and with density of mild steel of 7850 kg/m^3 resulting in a weight of 34.5 kg.

V Electric Motor was used for two purposes during the operation of the experiment. Firstly, it provided a means of accelerating of the system up to operational speed before the air supply was turned on, preventing waste of pressurised air during the start-up procedure. Secondly, after the air supply had been turned on, the motor provided a means to ensure constant speed operation by using the motor control system to dissipate generated electrical energy in breaking resistors. During this second mode of operation the motor

was acting in reverse as an electrical generator. The key characteristics of the motor, as stated by the manufacturer, are given in the Table 6.1.

Table 6.1: Electric Motor Characteristics.

Full Load Speed	2935 $[RPM]$
Voltage	400 $[V]$
Output	11.2 $[kW]$
Efficiency	IE2 91%

VI Drive Belt (toothed or timing belt) Pulleys were used together with a drive belt to connect the turbine shaft line to the electric motor and were selected such, that the turbine shaft line rotation was twice the speed of the electric motor.

VII Dynamic Braking Resistors The Braking Resistors (not shown in Figure 6.3) were used in motor-inverter-braking resistor control system for rapid deceleration of the system in case of emergency and for governing the speed of the turbine under operating conditions where power was being generated at levels greater than the losses in the system. Four resistor with the specifications shown in Table 6.2 were implemented into the system.

Table 6.2: Dynamic Braking Resistor Characteristics.

Part No	EST2-22R-SB
Resistance	20 $Ohms$
Power Rating	2000 W
Max Overload	10 x Power for 12 Seconds

6.1.2 Instrumentation

The instrumentation used on the Rotating Rig was similar to the "Mosquito" experiment with additional torque and speed measurements. As in the Mosquito experiment

the voltage signals from pressure transducers as well as from the temperature probes were logged using a National Instruments USB-6218 logging card. An OPB 704 opto-senso was used to measure turbine speed. This involved painting one half of the shaft black and other half white generating a one impulse per revolution rectangular signal which was subsequently logged using the USB-6218 logging card.

The Magtrol Torquemaster TM 210 torque transducer used had a rated torque of up to 50 Nm and maximum speed of 10000 RPM. It was used to measure the torque generated by the turbine and its speed output was used to validate the OPB 704 opto-sensor speed measurement.

Similar to the "Mosquito" experiment the pressures on the inlet of the unit as well as jet inlet pressure and the turbine outlet pressures were all measured using a ScaniValve DSA3217 pressure scanner.

6.1.2.1 Error Analysis

The error analysis for ScaniValve DSA3217 has been described previously in Section 3.3.5. The measurement error for Magtrol Torquemaster TM210 and Opto-Sensor OPB 704 is shown in Table 6.3. As stated in section above the voltages from Magtrol Torquemaster TM210 and OPB 704 were logged using USB-6218 logging card.

Table 6.3: Combined Measurement Error in Torque Transducer TM210 Data.

Magtrol Torquemaster TM210	<1%
Opto-Sensor OPB 704	<1 RPM

For the TM210 torque transducer, the temperature induced zero drift is less than 0.1% of the full range per 10 K. It has been neglected in this study, as there was only very slight variation in the ambient temperature during the tests. Further the influence of the speed on the torque measurement was less than 0.01% of the full range per 1000 RPM and was not taken into consideration. The measurement accuracy of the torque transducer was stated to be less than 0.1% of the measuring range of 50 Nm. With the absolute accuracy of the USB-6218 logging card voltage measurement, the torque measurement error was calculated to be less than 1%.

In case of Opto-Sensor OPB 704 sensor the speed measurement was validated against the speed signal provided by the torque transducer and the differences between the two measurement systems was found to be less than 1 RPM.

6.1.3 Data Evaluation

Durham Software for Wind-tunnels was used to post-process the logged data from the logging card. Pressures and temperatures were calculated and subsequently used to calculate mass flow rates. The logged pressure data from the ScaniValve was also used to determine the performance of the Expander Unit using Durham Software for Wind-tunnels and Matlab scripts.

6.2 Test Preparation and Measurement of the Components

6.2.1 Measurement of Jet and Leakage path Dimensions

The physical dimensions of the jet components were measured prior to the testing so that the manufactured dimensions were known. The measured dimensions are presented in Table 6.4. The measurement of the diameters of fluidic seal components H1 and H2 were carried out using vernier callipers. For each diameter several measurements were made with the average value and the variation shown in the Table 6.4. The measured critical dimension of the fluidic seal part H1 was $a_{measured} = 63.60 \pm 0.01mm$. In case of part H2 measured diameter was $b_{measured} = 63.55 \pm 0.01mm$. The leakage path diameter at location b was the smallest and therefor principal diameter. The size of a and b also represented the clearance diameter formed by the original labyrinth seal as described in Section 4.2.1.

The gap sizes of radial and axial leakage path dimensions were measured with the Expander partly assembled and carefully mechanically loaded so that the forces applied to the fluidic seal components were similar to these expected during normal operations of the test facility. Feeler gauges were used to measure gap sizes.

The measurement of the leakage path hight c as defined by the part H1 of the fluidic seal and the turbine rotor shroud, showed a gap size between $0.40mm < c_{measured} < 0.45mm$. The design gap size was $c_{def} = 0.44mm$. The axial leakage path

exit gap size, d, was measured to be between $0.20mm < d_{measured} < 0.25mm$.The design value was $d_{def} = 0.25mm$.

The fluidic seal jet gap e is formed between H1 and H2 fluidic seal components by using evenly circumferentially distributed shims between the jet gap surfaces as described in Section 4.3.3. During preparation for the fluidic seal tests it was found that the jet gap size was significantly affected by the clamping forces applied to the seal parts. To ensure a clamping force between 250 N and 300 N an 1.8 mm o-ring was positioned between the part H2 and pipe connector as shown in Figure 6.4. By fastening the pipe connector to the housing the o-ring was compressed axially by around 20% - 25% thereat a clamping force of around 260 N was required to do so. Without clamping force applied the jet curtain gap e was measured to be $0.10 < e_{measured} < 0.20mm$ whereat in assembled conditions the gap size was expected to be smaller. Due to the position of the jet gap, a direct measurement of the gap size e was not possible in assembled expander unit, therefore to verify the jet gap size, a choked test was carried out as described in Section 6.2.2.

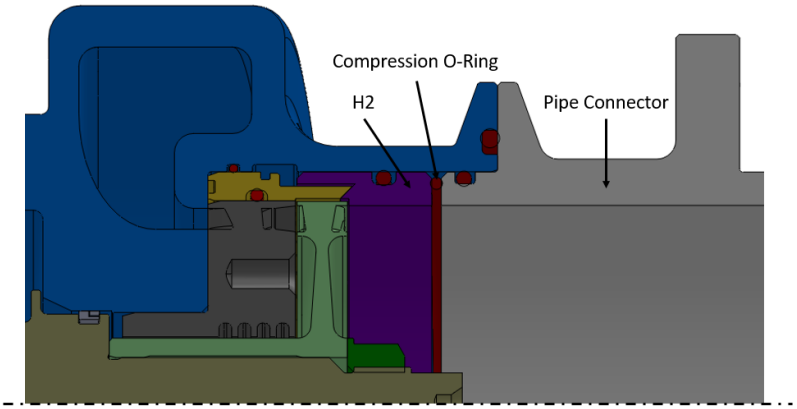

Figure 6.4: Cut-Through Rotating Rig with Compression O-Ring Positioned Between H2 and Pipe Connector.

Table 6.4: Measured Physical Dimensions of Fluidic Seal Components in Rotating Rig.

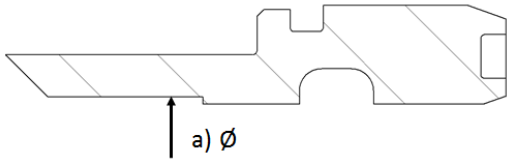 Fluidic Seal Component H1 Leakage Path Outer Diameter.	$a = 63.60 \pm 0.01mm$
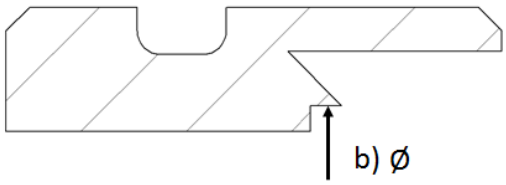 Fluidic Seal Component H2 Leakage Path Outer Diameter.	$b = 63.55 \pm 0.01mm$
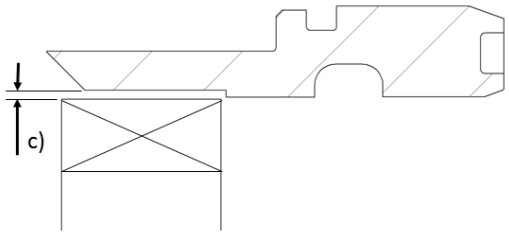 Leakage Path Gap Size Between H1 and Rotor Shroud.	$0.40 < c < 0.45mm$
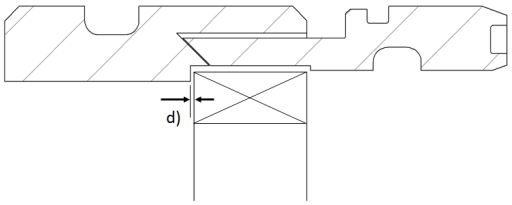 Axial Leakage Path Gap Size Between H2 and Rotor.	$0.20 < d < 0.30mm$
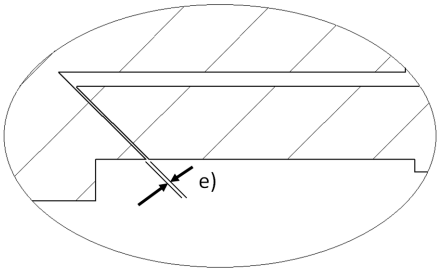 Jet Gap Width Formed by H1 and H2	$0.10 < e < 0.20mm$

6.2.2 Choked Test to Determine Mean Jet Width

In contrast to the "Mosquito" experiment, a direct physical measurement of the jet gap between components, H1 and H2, was not possible in the fully assembled rotating rig. In Section 6.2.1 the jet gap was determined by measuring components H1 and H2 outside of the Turbo Expander unit using feeler gauges. In order to investigate the jet gap size in the fully assembled and mechanically pre-loaded Turbo Expander unit, a choked flow test was carried out. A range of fluidic jet supply pressures were applied, whilst a constant pressure level was maintained at the outlet of the leakage path by controlling the turbine outlet pressure.

During the choked flow test, the mass flow rate was measured using O-plate 2 with flow temperature measured at the orifice plate position and jet pressure measured inside the jet cavity. The measurements were used to calculate jet area from Equation 6.1, which is derived from the basic compressible flow equation. With choked area as shown in Figure 6.5 representing a surface area of a cut cone the jet gap size e is calculated using rearranged equation for the cone surface, Equation 6.2, where b is the measured H2 diameter.

$$\dot{m}_{jet} = 2A_{choked}\left(\frac{1}{\gamma+1}\right)^{\frac{1}{\gamma-1}}\sqrt{p_{in\_jet}\rho_{in\_jet}\frac{2\gamma}{\gamma-1}} \tag{6.1}$$

$$th = \frac{\sqrt{\left(\frac{b}{2}\right)^2\pi^2 + \frac{\sqrt{2}}{2}A_{choked}\,\pi} - \left(\frac{b}{2}\right)\pi}{\frac{\sqrt{2}}{2}} \tag{6.2}$$

The choked conditions were expected to have been established at jet outlet to inlet pressure ratios of $pr_{jet} < 0.528$. In the Table 6.5 the summary of choked test conditions is presented.

Table 6.5: Choked Test Experimental Conditions.

Turbine Outlet Pressure	1 *bar*
Jet Inlet Pressure	Variable Pressure Range 3 - 7 *bar*
Turbine Rotational Speed	No Rotation, Stationary Test

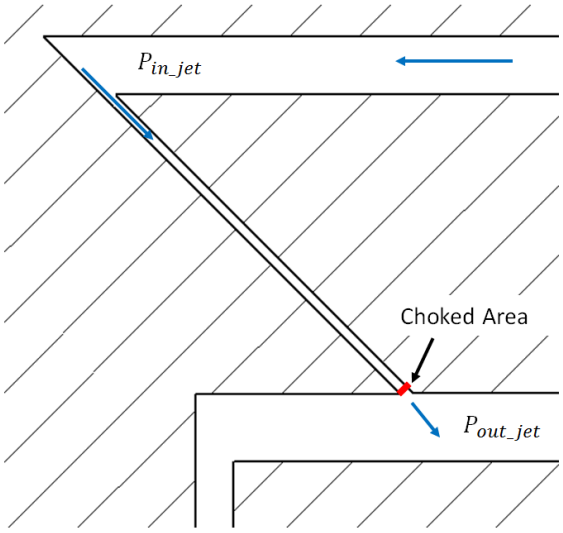

Figure 6.5: Expected Choked Area Position on the Outlet of the Jet Gap.

The effective gap size th was plotted for pressure jet outlet/inlet ratios below 0.528 in Figure 6.6.

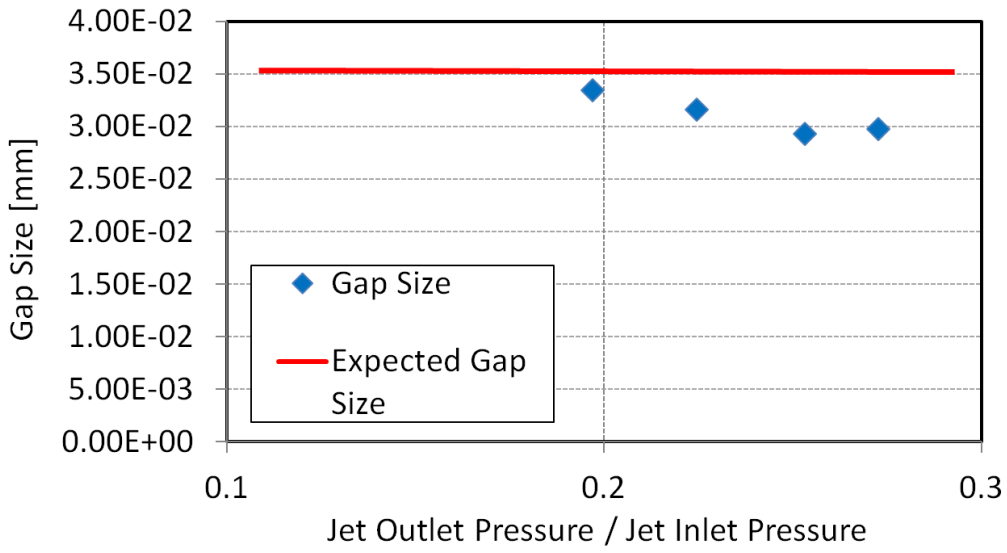

Figure 6.6: Calculated Gap Size.

The evaluation of the choked test effective area and effective gap size was complicated by the position and size of the distance holders between H1 and H2 components impeding correct prediction of the position of the established vertical shock. Based on previous experiences with fluidic seal components up to 10% reduction in measured gap size due to presence of the distance holders was expected. Despite the mea-

surement uncertainties and expected gap reduction, the values of the gap clearance measured in the choked tests were very close, within 15% of the design value, to the intended design specification.

As shown in Figure 6.6 with lower outlet-inlet pressure ratio the from measurements calculated gap size approaches the ideal dimension of 0.035 mm.

6.2.3 Stage Reaction Test

Throughout the rotating experiment the operational speed of the turbine was set to 36000 RPM, which is below normal operational speed of up to 60000 RPM in its intended configuration. This was done firstly to satisfy health and safety concerns and secondly to reduce the physical vibrations in the system increasing measurement accuracy of the torque transducer TM210 measurement. The experimental conditions were off-design and so the stage reaction was not known for the range of test conditions evaluated. The reaction of the stage changed at a constant operational speed due to changes in inlet and outlet pressures, which dictated, among others the mass flow rates through the turbo expander as well as stator outlet flow angles and rotor inlet angles.

A direct measurement of the pressure and flow conditions at the inlet of the rotor during operation was not possible, as explained previously in Section 6.1.2. The evaluation of the reaction was necessary for later experimental tests assessment, since the pressure drop across the rotor also affected the flow through the leakage gap and the performance of the fluidic jet seal.

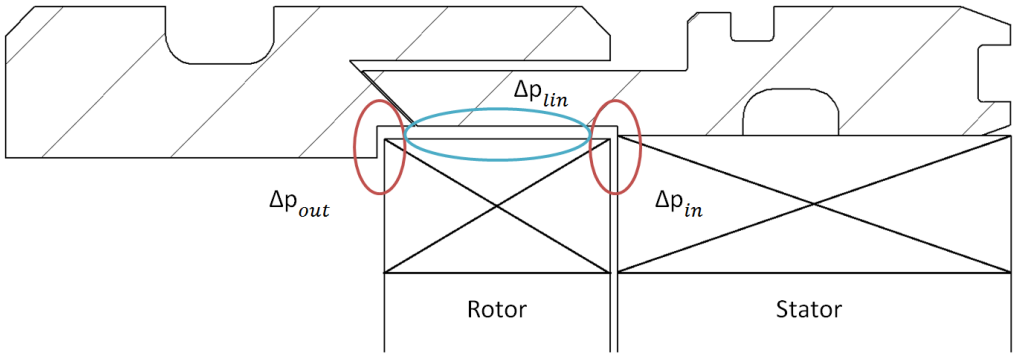

Figure 6.7: Leakage Path Main Pressure Drop Locations.

As shown in Figure 6.7 and described in Chapter 4 the governing pressure drops in the leakage path occur on the inlet and outlet axial restrictions indicated by the red circles in the figure.

For all experiments on rotating rig the outlet pressure was set to 4 *bar* and with constant turbine speed the reaction was only affected by the stage inlet pressure. During the stage reaction test the jet supply was closed off and pressure measurement of the jet inlet plenum pressure could be used to measure static pressure at the position of the fluidic jet exit above the rotor shroud.The conditions used in the tests to determine the reaction are summarised in Table 6.6.

Table 6.6: Reaction Test Experimental Conditions.

Turbine Inlet Pressure	Variable Pressure Range 5 - 9 [bar]
Turbine Outlet Pressure	4 [bar]
Turbine Rotational Speed	3600 [RPM]

$$r_s = \frac{p_{jet} - p_{out}}{p_{rot} - p_{out}} = \frac{\triangle p_{jet}}{\triangle p_{rotor}} \tag{6.3}$$

Under normal conditions a seal ratio coefficient r_s of 50% for the jet cavity pressure drop $\triangle p_{jet}$ is expected, although higher percentage is possible in cases of axial misalignment between the rotor and the seal components leading to smaller leakage path exit restriction. Since it was not possible to measure the rotor inlet pressure directly during operation, a seal ratio coefficient had to be assumed. The seal ratio coefficient is defined in Equation 6.3.

The reaction ratio of the turbine is defined as a pressure drop across the rotor over the pressure drop across the whole stage as shown in Equation 6.4 .

$$\hat{R} = \frac{\triangle p_{rotor}}{\triangle p_{stage}} \tag{6.4}$$

With the definition of the reaction ratio as well as assumption of certain fraction of pressure reduction up to position of the jet exit into the leakage path the Equation 6.5 is derived.

$$\hat{R} = r_s \frac{(p_{jet} - p_{out})}{\triangle p_{stage}} \tag{6.5}$$

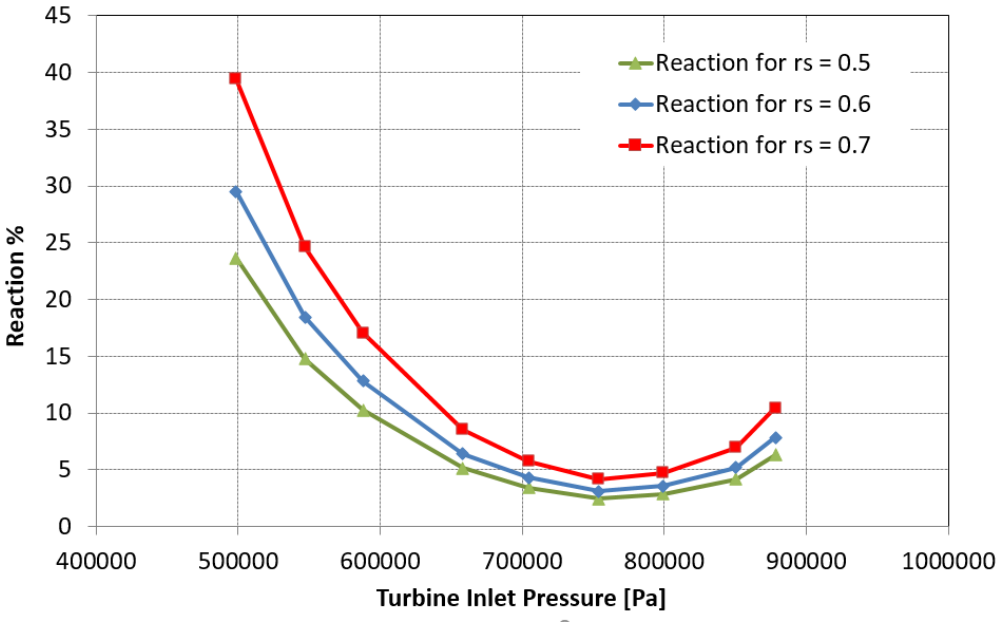

Figure 6.8: Reaction Calculated.

The results from the experiments are evaluated in Figure 6.8 assuming jet cavity pressure drop $\triangle p_{jet}$ around 50%, 60% and 70% of the pressure drop $\triangle p_{rot}$ across the rotor.

It can be seen in Figure 6.8 that the degree of reaction is highly dependent on turbine inlet pressure. A Turbine inlet pressure of 8 *bar* was selected for the further investigations carried out on the rotating rig. The selection of this particular pressure was based on the relatively small gradient changes of reaction due to pressures changes on inlet of the turbine and because the nozzles will be choked, so that the mass flow rate through the stage will be governed by stage upstream pressure. Further it was thought that introduction of the fluidic jet in the tests might influence the rotor inlet pressure which could change the reaction so selecting this value of inlet pressure minimises any impact of this effect. In the test described below the reaction was assumed to be constant.

6.3 Rotating Rig Test Results

This final test campaign on the rotating rig was carried out to evaluate the effect of the fluidic curtain type seal on the full turbine geometry under operational conditions including rotation at 36000 RPM. The performance of the turbine was measured for conditions with the jet switched off, in which case the geometry of the leakage path represented a standard turbine design and with the jet switched on with different jet supply pressures.

Following the initial fluidic seal investigations described in Chapter 3 and subsequent static rig "Mosquito" tests, a performance benefit of the turbine was expected with fluidic curtain applied. Further it was expected that increasing jet supply pressure would improve the turbine performance benefit up to the point where the fluidic seal became overblown, reversing the over-tip leakage and fluidic jet fluid to flow upstream and back out into the rotor inlet flow causing high losses.

Additionally to the mass flow rate and effective area evaluation used earlier in this chapter, specific power was also used to measure Turbo Expander performance calculated from Equation 6.6, where $P\,[W]$ is power generated by the turbine and $\dot{m}\,[kg/s]$ the total mass flow rate through the turbine.

$$P_{sp} = \frac{P}{\dot{m}} \tag{6.6}$$

The general test conditions for the normal test with jet switched on and off are summarised in Table 6.7.

Table 6.7: Normal Test Experimental Conditions.

Turbine Inlet Pressure	8 *bar*
Turbine Outlet Pressure	4 *bar*
Jet Inlet Pressure	Variable Pressure
Turbine Rotational Speed	3600 RPM

The turbo expander unit was supplied with a pressure of 8 *bar* on the inlet and 4 *bar* on the outlet with the aim to have a choked flow through the stator nozzles. Using

turbine reactions from the previous reaction evaluation of 3%, 4% and 5% the stator outlet over inlet pressure ratio was calculated as shown in Table 6.8. Maintaining pressure ratio below 0.528 ensured choked flow conditions and independence of nozzle mass flow rate from downstream pressure.

Table 6.8: Stator Pressure Ratio Depending on Turbine Reaction.

	1	2	3
Turbine Inlet Pressure	8 *bar*	8 *bar*	8 *bar*
Turbine Outlet Pressure	4 *bar*	4 *bar*	4 *bar*
Assumed Turbine Reaction	3%	4%	5%
Stator Outlet Pressure	4.12 *bar*	4.16 *bar*	4.2 *bar*
Stator Pressure Ratio	0.515	0.52	0.525
Choked Stator	Yes	Yes	Yes

The results of the test were evaluated for an assumed maximum and minimum reaction of 5% and 3% for fluidic jet pressure ratios up to 5. The seal over blown conditions were expected to be reached at pressure ratios between 2.5 and 3. Between pressure ratios of 3 and 5 a definitive specific power reduction was expected due to rotor inlet flow distortion induced by jet flow being forced out of the inlet to shroud tip seal.

The mass flow rates through the expander unit measured in the rotating tests are plotted against jet pressure ratio for 5% turbine reaction and 3% turbine reaction in Figure 6.9b and Figure 6.9c. For comparison, the mass flow rates through static test facility 'Mosquito' are shown in Figure 6.9a. In comparison to the static test the graphs for rotating test show an almost constant turbine inlet mass flow rate (squares) and constantly increasing turbine outlet flow rate (triangles) which is due to addition of jet flow (rhombus). Similar to the results shown for the static test, Figure 6.9a, a benefit was expected in rotating test in form of reduced outlet mass flow rate for seal pressure ratios up to 2.5, which was not observed.

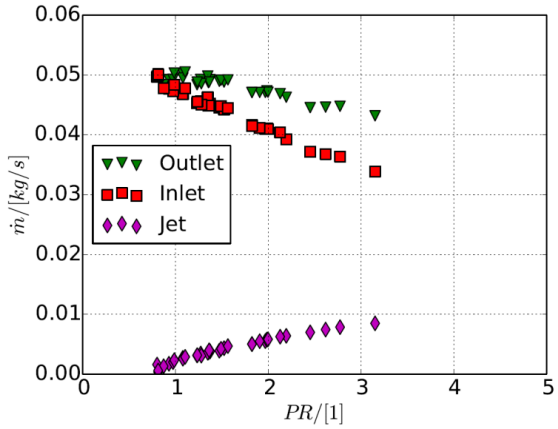

(a) Mosquito: Mass Flow Rate During Normal Test For Δp Measurements Within 3% of 8500 [Pa], Chapter 5.

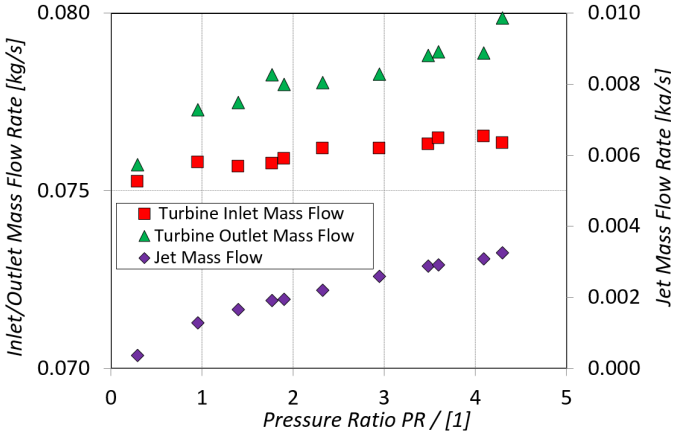

(b) Mass Flow Rate of the Rotating Turbo Expander Unit Plotted Against Jet Pressure Ratio (PR) for 5% Reaction.

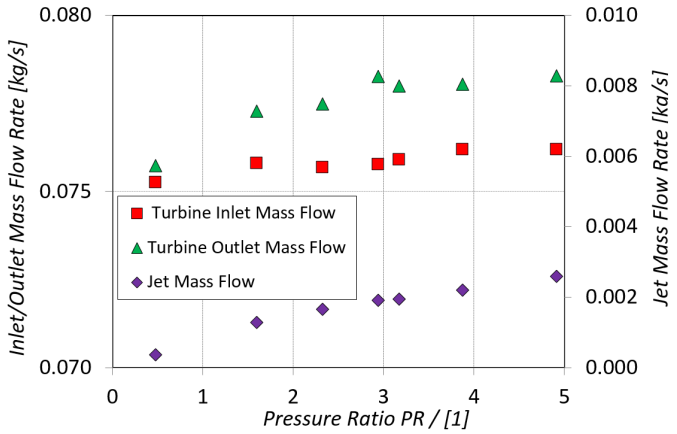

(c) Mass Flow Rate of the Rotating Turbo Expander Unit Plotted Against Jet Pressure Ratio (PR) for 3% Reaction.

Figure 6.9: Mass Flow Rate of the Rotating Test (c), (b), Compared to Static Test 'Mosquito' (a).

Further, the jet mass flow rate in the rotating test was only 25% - 30% of the static test jet flow rate at the same pressure ratio ($PR = 3$) indicating a possible reduced jet gap size during operation of the rotating turbine expander unit. Still, even with a reduced jet gap size a reduction in overall mass flow rate was expected but not observed. From the plots for mass flow rate, Figure 6.9b and Figure 6.9c, it is apparent, that the fluidic jet seal didn't perform as expected to reduce the outlet flow rate.

Figure 6.10 shows the specific power (crosses), Equation 6.6, plotted together with the actual power (yellow circles) against seal pressure ratio for the 3% reaction case. As expected the scatter in the data is reduced by plotting specific power, which shows more clearly the constant reduction in specific power and with it turbine performance seen in the test. In contrast to the experimental data shown in Figure 6.10, the 2D axis-symmetrical calculation of the leakage path with fluidic jet seal implemented, as described in Chapter 4, showed a clear benefit and an increase in specific power for increasing jet pressure ratio.

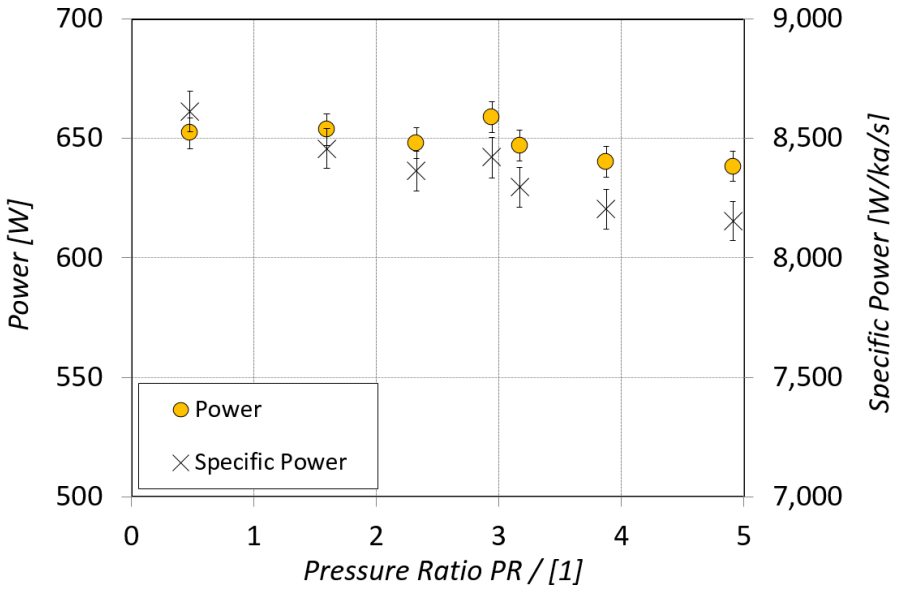

Figure 6.10: Power and Specific Power of the Turbo Expander Unit Plotted Against Jet Pressure Ratio (PR) for 3% Reaction.

The effective area (blue circles) was evaluated in Figure 6.10 using Equation 6.7 as described in Section 5.1.4 and plotted together with specific power (crosses) against

seal pressure ratio for the 3% reaction case. The rotor inlet pressure P_{0in} was determined assuming the 3% reaction and C_f and $Norm$ found as described in Section 5.1.4. As shown in Figure 6.10 the effective area increased between the no-jet case and assumed overblown condition at a pressure ratio of 2.5 by approximately 2%. Again the data in Figure 6.10 shows a contrary behaviour of the effective area to the effective area reduction observed in the static tests as shown in Section 5.2.2, Figure 5.8.

$$A_{eff} = \frac{\dot{m}_{outlet}}{\sqrt{2 \cdot \rho \cdot (p_{0in} - p_{out})}} \cdot \frac{1}{C_f} \cdot Norm \tag{6.7}$$

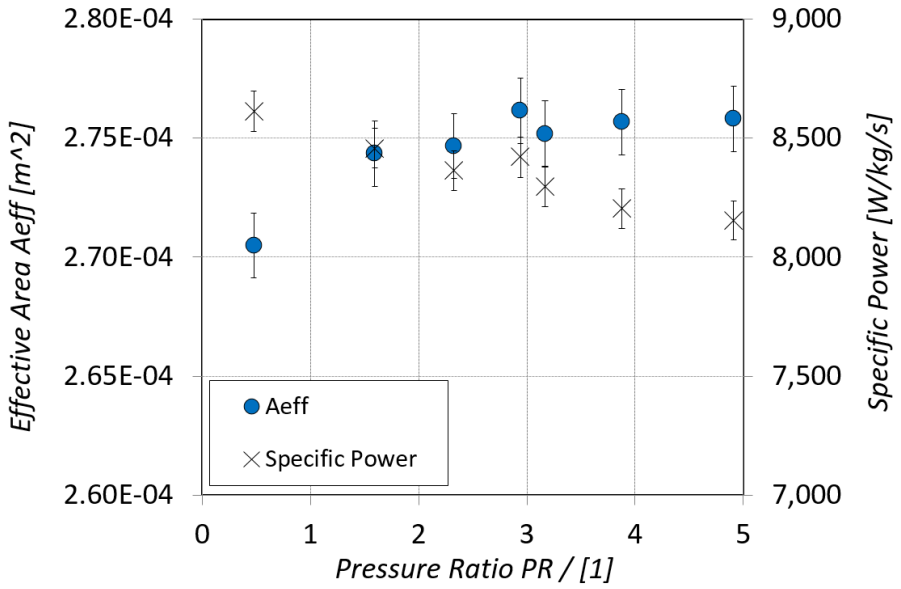

Figure 6.11: Power and Calculated Effective Area Plotted Against Jet Pressure Ratio (PR) for 3% Reaction.

In Figures 6.12a, 6.12b and 6.12c expanded plots for mass flow rates, specific power and effective area are shown against pressure ratios up to 10 for a 3% reaction. As mentioned above from a certain pressure ratio on (approximately 2.5), over-blown conditions were expected to be observed with sudden significant drop in specific power. In Figure 6.12b, no sudden change in specific power is observed, showing a continuous and constant reduction in specific power and with it turbine performance beyond the point of over-blown condition.

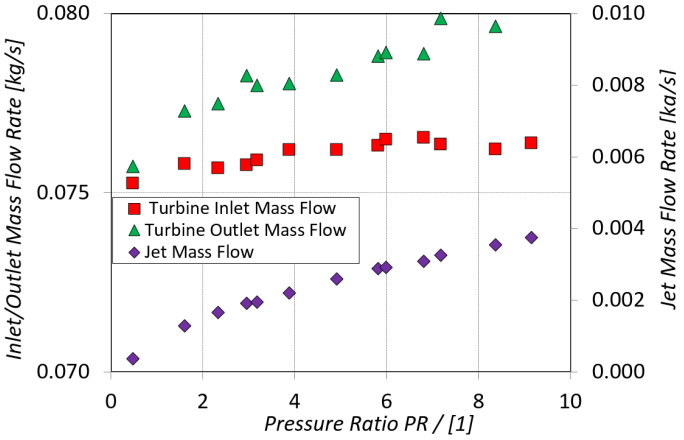

(a) Mass Flow Rate of the Rotating Turbo Expander Unit Test Plotted Against Jet Pressure Ratio ($PR < 10$) for 3% Reaction.

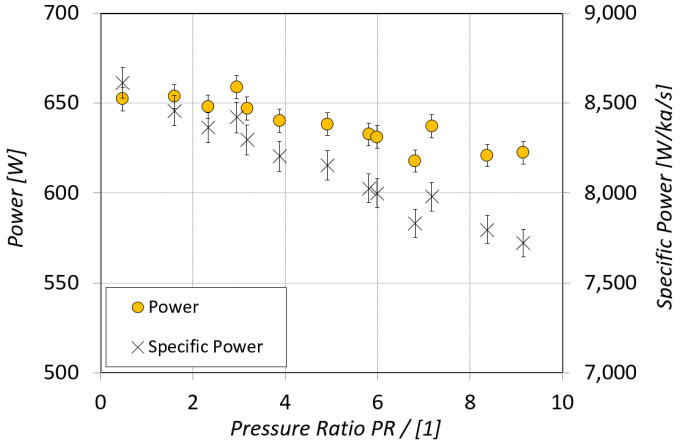

(b) Power and Specific Power of the Rotating Turbo Expander Unit Test Plotted Against Jet Pressure Ratio ($PR < 10$) for 3% Reaction.

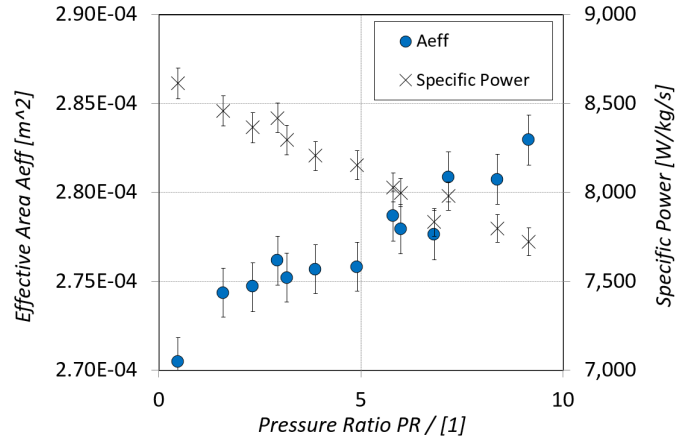

(c) Effective Area and Specific Power of the Rotating Turbo Expander Unit Test Plotted Against Jet Pressure Ratio ($PR < 10$) for 3% Reaction.

Figure 6.12: Expanded Plots for the Rotating Turbo Expander Unit Test.

It is apparent from the results shown above, that the fluidic seal implemented in the rotating turbo expander unit didn't perform as expected. The results shown in this section are in contrast to the investigations carried out on a 2D axis-symmetrical calculation of the leakage path with fluidic seal implemented (Chapter 4), showing a clear benefit by increasing the specific power as well as the static tests on the expander unit geometry (Chapter 5), showing a clear reduction in turbine inlet and outlet flow with increasing jet pressure ratio.

6.4 Conclusion

During the test campaign described in this chapter the performance of the fluidic seal was evaluated in the turbo expander unit under operational conditions. In the first part the jet seal gap size was verified using choked flow conditions, showing a gap size of 0.034 mm which was close to ideal gap size of 0.035 mm. Further the reaction of the turbine was calculated showing a reaction at operational conditions between 3% and 5%. Finally the performance of the fluidic seal was tested showing a trend opposing previous assumptions as well as previous experimental and numerical investigations.

The benefit of the fluidic jet was clearly shown in the 2D axis-symmetrical investigations as well as in static experimental tests performed on the actual expander unit geometry, but in the rotating test described in this chapter it was not possible to demonstrate the expected performance improvement.

A definitive cause of the malfunction of the rotating experiment could not be established by the end of this investigation campaign, but possible suggestions for this will form future work and are:

- **Axial movement of the seal inserts.** A possible change in seal geometry during operation especially an axial movement of the seal inserts positioning the jet slot downstream toward the leakage path exit, resulting in the jet flow being injected into the rotor outlet flow without interference with the leakage flow. Such a behavior could be contributing to the overall outlet flow increase. Further the axial movement would increase the downstream restriction additionally decreasing the performance of the seal, which relies on tight downstream restriction.

- **Change of jet gap size during operation.** A change in gap size could be caused by elastic deformation of the jet inserts due to exceeding pressure forces. Further, due to the low temperatures downstream of the stator, the water in the jet air supply could condense and freeze creating a full or partial blockage of the jet gap during operation.

- **Thermal expansion of the expander unit components** The expander unit, integrated inside the Durham Blow Down Facility, is operated with air as a working fluid at much lower thermal conditions, as low as 250 K, in a contrast to the original temperatures of up to 350 K with organic fluid as a working medium in intended application. Additionally, during the tests in Durham Blow Down Facility, the lower temperatures are reached suddenly and with only short test durations possible, due to Durham Blow Down Facility configuration, an even thermal expansion of all Turbo Expander components could not be possible resulting in changing seal geometry.

- **Axial movement of the rotor.** Axial movement of the rotor is the least likely possibility, due to the nature of the rotor bearings, but an axial movement upstream or downstream could result in tightening of the axial leakage path gap resulting in much reduced leakage flow rate and resulting in the over-blown conditions reached at much lower pressure ratio with overall reduced benefit in specific power.

- **Additional leakage paths.** Additional leakage paths could not been properly investigated or quantified in the rotating facility and could have had a negative effect on the overall expander unit performance, depending on jet inlet pressure. In the successful static tests on the Mosquito all additional leakage paths were eliminated. Mosquito experiment was also designed to include all possible additional leakage paths with the possibility of observation and evaluation during operation in future work.

Chapter 7

Conclusion and Future Work

7.1 Conclusion

The literature analysis in Chapter 2 showed, that fluidic seals were first patented in 1954 by Auyer et al. [6]. Up to the year 2009 fluidic seal devices appeared several times in various patents, but there were only a few publications focusing on fluidic seals development. In 2009 Curtis et al [14] published a paper on a fludic seal installed on an experimental single stage, low speed, axial flow air turbine, showing the potential of a fludic seal for reducing shroud leakage flow. Following this work Hogg and Ruiz [34] and other authors showed the potential of the fluidic seal in several other applications.

The experiment presented in Chapter 3 was developed to investigate fluidic seal in combination with kinetic energy blocker and downstream restrictions. The idea of kinetic energy blocker and the fluidic seal was developed into a patent and was based on the observation that a fluidic jet with high kinetic energy could compromised the performance of the downstream seal, if the kinetic energy of the jet flow was allowed to impinge on the downstream restriction. Similar effects can be observed in see-through labyrinth seals, where the first restriction would generate a wall jet which, if not carefully treated, would carry high kinetic energy jet fluid beyond the following expansion and into the next restriction downstream. Failure to fully dissipate the kinetic energy in this way will result in pressure recovery beyond the seal restriction and negation of intended leakage flow reduction. The new design features a jet inclined towards the leakage flow direction with a kinetic energy blocker situated around 160% of the leakage path height downstream of the jet entry slot location and

before any downstream restrictions. IN the tests described in Chapter 3 the downstream restriction consisted of a two fin see-through labyrinth configuration with an expansion cavity between the fins. The experimental and numerical investigations on this geometry showed an effective reduction of leakage mass flow rate up to 40% with jet switched on. The numerical investigations on the geometry also showed a much lower maximal leakage flow reduction of only 17% and at a much higher seal pressure ratio PR with the blocker removed.

The investigations presented in Chapters 4 and 5 on a small high-speed single stage axial flow turbine geometry demonstrated the great potential of fluidic seals to reduce turbine stage leakage flow. Firstly, the CFD investigation and optimisation of a fluidic rotor tip seal were preformed, followed by an experiment on a static rig featuring the turbine rotor and seal components. This work involved replacing the original labyrinth tip seal geometry of the turbo expander unit with the new fluidic seal design. The seal replacement was done by machining the turbo expander casing and some other original components. The design of the new fluidic seal assembly comprised of two inserts, which were easily replaceable and could be quickly modified. The analysis of the performance benefit from the switch between the labyrinth and the fluidic seal was carried out by CFD using a semi-automated optimisation process. The CFD results predicted that the change from the labyrinth geometry to the fluidic seal reduced the rotor tip leakage flow by approximately 25% which was confirmed by the tests carried out on the static test rig.

In a final experiment presented in Chapter 6, the fluidic seal was tested in the rotating single stage turbo expander unit. It was not possible to detect any notable performance improvements from applying the fluidic seal in these experiments. The lack of detectable improvement could be due to one or more of a number of causes, such as, secondary flow leakages including leakages through the bearing chamber, which could not been measured or reliably approximated in the test rig with the existing instrumentation setup.

The experimental result on both static test rigs and the numerical results on static and rotating applications, plus the analytic analysis all showed that fluid seals have the potential to be used as higher performance alternatives to conventional seal designs such as labyrinth seals. Further, the fluidic seal could also be applied in gas

turbines to deliver additional benefits flrom rotor cooling flows. It could also be used to influence the rotor dynamics due to the ability of the fluidic seal arrangement to dynamically change pressures in certain areas of the over-shroud leakage path.

A summary of the main contributions from this thesis are:

- Overall, this thesis on the use of the fluidic seal devices to minimize or restrict parasitic flow through leakage paths, has demonstrated the potential of fluidic seal technology to significantly reduce the leakage flows and to potentially offer higher performance alternatives to other established types of seal technology.

- An original concept for a fluidic seal was presented in Chapter 3, where the fluid jet was used to decrease the pressure drop across standard turbomachinery seals, showing conclusively that the presence of the fluidic jet reduced the leakage flow by over 40% in some cases.

- The fluidic seal concept presented in Chapter 3 has been patented.

- An analytical model has been developed and presented for calculating fluidic seal performance, which shows excellent agreement with CFD and experiments validation data.

- In Chapter 4 the design of the fluidic seal for an application as a rotor tip seal on a small high-speed single stage axial flow turbine, was described. The optimisation process based on CFD predicted an overall turbine output power improvement of just over 3% due to the application of the fluidic tip seal.

- A static test facility was developed and used to test the rotor shroud tip seal design developed in Chapter 4. The experiments carried out on this rig showed up to 4% reduction in total stage throughflow due to the new seal and a leakage flow path area reduction of 32%.

- A rotating test facility was created to demonstrate the turbine output power improvement from applying the fluidic tip seal. Extra work is required in order to be able to demonstrate the benefits of the fluidic seal in these facility.

7.2 Future Work

Following on from the study described in this thesis it is recommended that the following topics are addressed in further work.

- **Improvement of the Rotating Rig Experiment** - The improvement of the rotating rig experiment, as presented in Chapter 6, is needed in order to demonstrate the fluidic seal concept delivering benefits in a rotating environment. To achieve this, additional instrumentation is needed i.e to measure the bearing chamber pressure, the pressure at blade tip hight between the stator and the rotor, etc. Further, the positions of the seal components relative to the rotor and stator under load conditions have to be monitored. To validate future rotating experiment results, a three dimensional CFD simulation of the rig including a rotating rotor geometry is needed.

- **Cooling Effects** - With ever increasing temperatures in modern turbo-machinery, in some cases beyond melting points of the components, the need for cooling of the components is also increasing or becomes critical in areas where absence of cooling for short period of time leads to a total loss of the machinery. In recent decades, cooling has been widely used on the high pressure stages of gas turbines, where cooling is achieved by using air bled from the compressor supplied through internal cooling channels or through holes in blades themselves or by impinging cooler air jets onto the hot surfaces. Since fluidic seals also include an impinging jet, the potential exists to also use the cooling flow to supply the fluidc jet. Several further questions arise on cooling efficiency of the fluidic jet influenced by presence of the kinetic energy blocker or downstream restrictions size, shape and position, as well as the position of the fluidic jet itself and dependency of cooling flow on pressure ratios and jet mass flow rates. For example, a cooler impinging fluidic jet fluid could be used to interact with housing before it is used to form the fluidic jet, already creating a cooling effect upon the housing (or stationary) component. In the leakage path it would create a fluidic seal impinging upon the rotor and simultaneously providing cooling for the rotor. Further down the leakage path the strong fluidic jet could be guided

alternating between the stationary and rotor surfaces, impinging and providing further cooling effects for both surfaces.

- **Rotor Dynamic Effects.** - The presence of the fluidic jet can change the radial and axial forces acting upon the rotor inside the leakage cavity by changing the static pressure, and the shroud shear forces. In cases, where the rotor dynamic can be influenced by the seal geometry, the fluidic seal can have a negative or a positive effect introducing dampening or feeding energy into the dynamic system. For example, this effect can be achieved by rapidly changing the jet supply pressures at every location along the circumference simultaneously, or by splitting the fluidic jet slot into sections with separate supplies which could have different supply pressures.

- **Fluidic Seal Outside of Normal Operational Conditions** - Throughout turbine operation, different operational conditions are experienced, especially during start-up and shut-down events as well as during partial load operations. During these events, the fluidic seal has to provide seal capabilities as well as secondary capabilities such as cooling.

  Further, the capability of the fluidic seal is dependent upon the seal geometry and changes to the geometry which could occur during the turbine variable load operation should be investigated, including partial blockage of the jet slot or holes, erosion of the seal material and depositions of secondary materials inside the seal geometry etc.

- **Effects of Fluidic Jet Pre-swirl** - The efficiency of the fluidic seal can be improved by introduction of pre-swirled jet instead of a jet introduced into the leakage path in strictly radial direction. The effects and improvements possible as well as the influence of the seal geometry upon such jets has to be further investigated.

- **Optimisation of the Downstream Restriction and Combination with Other Seal Designs** - The presented work in this thesis only considered simple downstream restriction geometries with a labyrinth seal or axial shroud exit restriction. Further investigation is required to find an optimal complimentary seal designs.

Appendix A

Fluidic Seal Patent

The experimental, CFD and analytical studies described in Chapter 3 have demonstrated the potential for using fluid jets to reduce the pressure drop across conventional seal types and therefore decrease the leakage flow through them. A patent was filled (PCT/GB2014/051683) and subsequently published on December 4th 2014 by the collaborating industry partner Cummins Turbo Technologies, in order to protect the findings. The patent referred to "a seal assembly for restricting fluid leakage flow through a fluid leakage cavity defined between rotating and stationary components. The seal assembly comprising a fluid jet outlet configured to admit a fluid jet into the fluid leakage cavity in an upstream direction, which is inclined to the axis, a first flow restriction located downstream of the fluid jet outlet and at a location such, that the fluid jet admitted from the fluid jet outlet would impinge on the first flow restriction once the fluid jet has turned to flow in an axial direction, and a second flow restriction located downstream of the first flow restriction".

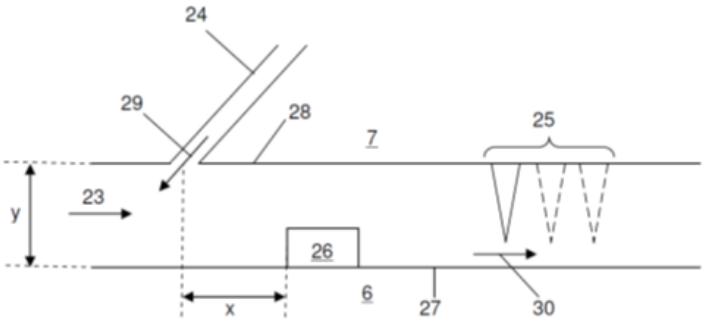

Figure A.1: Patent: Seal Assembly, Possible Seal Configuration A

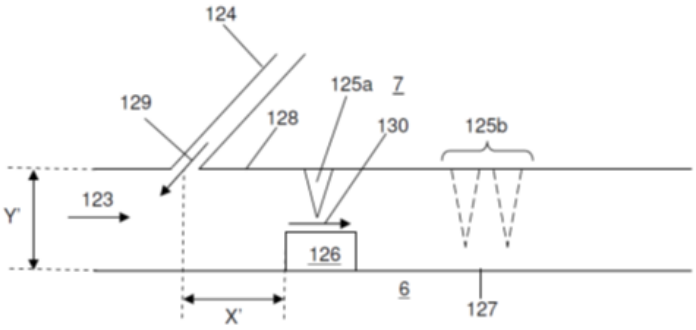

Figure A.2: Patent: Seal Assembly, Further Seal Configuration B

Schematic diagrams of some possible seal assemblies are presented In Figure A.1 and Figure A.2 from the patent application. Position 24 and 124 indicate the jet supply slot or holes, position 26 and 126 indicate the kinetic energy stopper so the jet emitted from opposing component 28 or 128 is impinging upon the component 27 or 127 shortly in front of the stopper 26 and 126. The position x and x' describe the distance of the first restriction downstream of the jet slit or holes. The dimension x or x' have to be carefully selected during the design process and ideally the impingement of the jet upon the wall should be in front of the first kinetic energy stopper (component 27 or 127). Positions 25 and 125b show possible conventional seal configurations downstream of the jet outlet and the first restriction, however a combination of kinetic energy stopper and downstream restriction is possible as shown by 125a.

The diagrams in Figures A.1 and A.2 show the fluid jet being used in combination with labyrinth restrictions. However, the patent covers the fluid jet being used with any form of other type of sealing element e. g. brush seal, leaf seal etc. The fundamental principle describe in the paten of using fluid jets to decrease the pressure drop across sealing elements, in order to reduce the leakage flow past them, applies to tall types and forms of turbomachinery seal.

References

[1] *ANSYS Fluent Theory Guide*, v15 edition, 2013.

[2] J. S. Alford. Protecting turbomachinery from self-excited rotor whirl. *Journal of Engineering for Gas Turbines and Power*, 87(4):333–343, October 1965.

[3] F. Armstrong, J.; Perricone. Turbine instability solution - honeycomb seals. pages 47–56, Texas A&M University, College Station, TX, 1996.

[4] Gul Arora, Margaret Proctor, Bruce Steinetz, and Irebert Delgado. Pressure balanced, low hysteresis, finger seal test results. In *Joint Propulsion Conferences*, pages –. American Institute of Aeronautics and Astronautics, June 1999.

[5] A. Auld, M. Hilfer, S. I. Hogg, G. Ingram, and Messenger A. Application of an air-curtain jet type seal to reduce turbine shroud leakage. *Proceedings of the ASME Turbo Expo 2013*, (GT2013-94198), June 2013.

[6] E. L. Auyer. Dynamic seaseal arrangements for turbomachines, 1954.

[7] P. Basu, A. Datta, R. Loewenthal, J. Short, and R. Johnson. Hysteresis and bristle stiffening effects in brush seals. *Journal of Propulsion and Power*, 10(4):569–575, July 1994.

[8] Aaron Bowsher, Peter Crudgington, Clayton M. Grondahl, James C. Dudley, Tracey Kirk, and Andrew Pawlak. Pressure activated leaf seal technology readiness testing. *Journal of Engineering for Gas Turbines and Power*, 137(6):062503–062503, June 2015.

[9] D. Childs, D. A. Elrod, and Keith Hale. Annlular honeycomb seals: Test results for leakage and rotordynamic coefficient; comparisons to labyrinth and smoth configurations. *NASA Technical Reports*, (N89-22899), 1989.

[10] D. W. Childs. *Turbomachinery Rotordynamics: phenomena, modelling and analysis.* John Wiley and Sons Inc, 1993.

[11] J. M. Childs, D. W.; Vance. Annular gas seals and rotordynamics of compressors and turbines. pages 201–220, Texas A&M University, College Station, TX, 1997. 26th Turbomachinery Symposium.

[12] Lattime Scott B. Steinetz Bruce M. Chupp Raymond E., Hendrics Robert C. Sealing in turbomachinery. *Journal of Propulsion and Power*, 22(2(2006)):313–349, 2006.

[13] John. I. Cofer, John. K. Reinker, and William J. Sumner. Advances in steam path technology. *GE Power Generation*, (GER-3713E), 1996.

[14] E. M. Curtis, J. D. Denton, J. P. Longley, and B. Rosic. Controlling tip leakage flow over a schrouded turbine rotor using an air-curtain. *ASME TURBO Expo 2009*, (GT2009-59411), 2009. Orlando.

[15] I. Delgado and M. Proctor. Continued investigation of leakage and power loss test results for competing turbine engine seals. *42nd Joint Propulsion Conference and Exhibit*, (AIAA20064754), 2006.

[16] Saim Dinc, Mehmet Demiroglu, Norman Turnquist, Jason Mortzheim, Gayle Goetze, John Maupin, James Hopkins, Christopher Wolfe, and Mark Florin. Fundamental design issues of brush seals for industrial applications. *Journal of Turbomachinery*, 124(2):293–300, April 2002.

[17] Y. Dogu, M. C. Sertcakan, A. S. Bahar, A. Piskin, and M. Ancan, E. Kocaguel. Computational fluid dynamic investigation of labyrinth seal leakage performance depending on muschroom-shaped tooth wear. *J. Eng. Gas Turbines Power 138(3)*, (GTP-15-1319), 2015.

[18] A. Egli. The leakage of steam through labyrinth seals. Number 57, pages 115–122. Transactions of the ASME, 1935.

[19] Achmed Mohamed Gamal Eldin. *Leakage And Rotordynamic Effects Of Pocket Damper Seals And See-Through Labyrinth Seals.* PhD thesis, Texas A&M University, 2007.

[20] D. A. Elrod. Discussion: the acoustic influence of cell depth on the rotordynamic characteristics of smooth-rotor/honeycomb-stator annular gas seals (kleynhans, g. f., and childs, d. w., 1997, asme j. eng. gas turbines power, 119, pp. 949-956). *Journal of Engineering for Gas Turbines and Power*, 119(4):956–956, October 1997.

[21] J. Ferguson. Brushesashturbomachinery gas turbine seal. *ASME Gas Turbine and Aeroengine Congress*, (88-GT-182), June 1988. Amsterdam, The Netherlands.

[22] Robert Flitney. *Seals and Sealing Handbook*. Elsevier Ltd., fifth edition edition, 2007.

[23] Ahmed M. Gamal, Bugra H. Ertas, and John M. Vance. High-pressure pocket damper seals: Leakage rates and cavity pressures. *Journal of Turbomachinery*, 129(4):826–834, September 2006.

[24] D. Gansle, A. & Childs. Experimental leakage and rotordynamic results for helically groved annlular gas seals. *ASME Journal of Engineering for Gas Turbines and Power*, 118:389–393, 1996.

[25] C.M. Grondahl. Seal assembly and rotary machine containing such seal, November 2003.

[26] W. Grtner. Rb199, technologischer spitzenreiter seiner zeit. Symposium '40 jahre erstflug tornado', MTU Aero-Engines, October 2014.

[27] Ed Halliwell. Testing waste heat expanders for new generation diesels. HTi, Company Magazine 3766118 Edition 17, Cummins Turbo Technologies, 2012.

[28] Jr Harold Addy, E, Harold Howe, Joseph Flowers, and Bruce Steinetz. Preliminary results of silicon carbide brush seal testing at nasa lewis research center. In *Joint Propulsion Conferences*, pages –. American Institute of Aeronautics and Astronautics, July 1995.

[29] L. T.; Muszynska A. Hendricks, R. C.; Tam. Turbomachine sealing and secondary flows. part 2; review of rotordynamics issues in inherently unsteady flow systems

with small clearances. Technical Report NASA/TM-2004-211991/PT2, NASA Glenn Research Center, Cleveland, OH, United States, July 2004.

[30] R. C. Hendricks and T. Trent Stetz. Flow rate and pressure profile for one to four axially alined orifice inlets. *NASA Technical Paper*, (2460), May 1985.

[31] M. Hilfer, S. I. Hogg, and G. Ingram. Experimental validation of a curtain type fluidic jet seal on a turbine rotor shroud. *Proceedings of the ASME Turbo Expo 2015*, (GT2015-42624), June 2015.

[32] Ernst H. Hirschel, Horst Prem, and Gero Madelung. *Luftfahrtforschung in Deutschland*. Bernard and Graefe, January 2001.

[33] B. Hodkinson. Estimation of the leakage through a labyrinth gland. *Proceedings of the Institution of Mechanical Engineers*, 141:283–288, 1939.

[34] I. G. Hogg, S. I. & Ruiz. Fluidic jet barriers for sealign applications. Number GT2011-45353, Vancouver, British Columbia, Canada, June 6-10 2011. ASME Turbo Expo 2011.

[35] K. G. ; Silvaggio J. A. Jr. Hoppock, W. G.; Van Bramer. Abradable seals in turbomachinery. *11th Turbomachinery Symposium*, pages 61–68, 1982.

[36] J. R. Johnston. Performance and reliability improvements for heavy-duty gas turbines. *GE Power Systems*, (GER-3571H), 2000.

[37] B. E. Launder and D. B. Spalding. Lectures in mathematical models of turbulence. *Academic Press, London, England*, 1972.

[38] B. E. Launder and D. B. Spalding. The numerical computation of turbulent flows. *Computer Methods in Applied Mechanics and Engineering*, 3:269 – 289, 1974.

[39] F. H. Mahler. Advanced seal technology. *Pratt & Whitney Aircraft Report*, (PWA-4372), 1972.

[40] Martin. Labyrinth packings. *Engineering*, pages 35–36, January 19 1908.

[41] Bernard Massey. *Mechanics of Fluids*. Taylor & Francis Group, eighth edition edition, 2006.

[42] Andrew Messenger. Design of a fluidic seal test facility. M.Eng Research Project, April 2013.

[43] M. Minoda, S. Inoue, H. Usui, and H. Nouse. Air sealed turbine blades, 1988.

[44] B. R. Morton, G. Taylor, and J. S. Turner. Turbulent gravitational convection from maintained and instantaneous sources. *Proceedings of the Royal Society of London A: Mathematical, Physical and Engineering Sciences*, 234(1196), 1956.

[45] Kutz Myer, editor. *Mechanical Engineers Handbook, Fourth Edition: Manufacturing and Management*. John Wiley And Sons Inc, 2015.

[46] NASA. *Liquid Rocket Engine Turbopump Rotating-Shaft Seal*, nasa sp-8121 edition, February 1978.

[47] M. J. Neale, editor. *The Tribology Handbook*. Butterworth-Heinemann, Oxford, second edition edition, 1995.

[48] S. Paillat and E. Kaminski. Second-order model of entrainment in planar turbulent jets at low reynolds number. *Physics of Fluids*, 26(045110 (2014)), 2014.

[49] R. M. Pastrana, C. E. Wolfe, N. Turnquist, and M. E. Burnett. Improved steam turbine leakage control with a brush seal design. In *30th Turbomachinery Symposium*, 2001.

[50] M. P. Proctor and I. R. Delgado. Leakage and power loss test results for competing turbine engine seals. *Turbo Expo 2004*, (GT200453935).

[51] S. Quoilin and V. Lemort. Technological and economical survey of organic rankine cycle systems. In *5th European Conference Economics and Management of Energy in Industry*, Vilamoura, Algarve, Portugal, 14-17 August 2009.

[52] N. Rajaratnam. *Turbulent Jets*. Number ISBN 0-444-41372-3. Elsevier Ltd., 1976.

[53] F. P. Ricou and D. B. Spalding. Measurements of entrainment by axisymmetrical turbulent jets. *Journal of Fluid Mechanics*, 11(10.1017/S0022112061000834):21–32, 1961.

[54] ScaniValve. *Model DSA 3217/3218 Digital Sensor Array Data Sheet No. G511.* Scanivalve Corp., 1722 N. Madson Street, Liberty Lake, WA 99019, USA, 2013.

[55] Robert J. Schmal. A discussion of turbine and compressor sealing ddevice and systems. *Proceedings of the 6th Turbomachinery Symposium*, pages 153–168, 1977.

[56] John Short, Prithwish Basu, Amitava Datta, Robert Loewenthal, and Robert Prior. Advanced brush seal development. In *Joint Propulsion Conferences*, pages –. American Institute of Aeronautics and Astronautics, July 1996.

[57] H. J. Smile. Pressurized seal, 1960.

[58] Aksel N. Spuck J. H. *Fluid Mechanics.* Springer-Verlag Berlin Hidelberg, ISBN 978-3-540-73536-6, 2008.

[59] R. C. & Munson J. Steinetz, B. M.; Hendricks. Advanced seal technology role in meeting next generation turbine engine goals. *NASA Technical Report Server*, (20000020798), 1999.

[60] H. Stocker. Advanced labyrinth seal design performance for high pressure ratio gas turbines. Houston, Texas, USA, Nov 30th - Dec 4th 1975.

[61] Aurel Stodola. *Steam and Gas Turbines: With a Supplement on The Prospects of Thermal Prime Mover; Authorized Translation From the Sixth German Edition by Dr. Louis C. Loewenstein.* McGraw Hill book company, 1927.

[62] S. Suryanarayanan and G. L. Morrison. Analysis of flow parameters influencing carry-over coefficient of labyrinth seals. *Proceedings of the ASME Turbo Expo 2009*, (GT2009-59245), Orlando, Florida, June 8-12 2009.

[63] A. H. Turner. Rotary seal with pressureized air directed at fluid approaching the seal, 1978.

[64] N. A. Turnquist, K. L. Bruce, C. Cerretelli, and J. E. Tourigny. Fluidic sealing for turbomachinery, 2009.

[65] R. G. Unsworth and R. K. Burton. Turbines, 1971.

[66] J. Vance, J. M. & Li. Test results of a new damper seal for vibration reduction in turbomachinery. Number 95-GT-036, Houston, Texas, USA, June 58 1995. ASME 1995 International Gas Turbine and Aeroengine Congress and Exposition.

[67] R. R. Vance, J. M.; Shultz. New damper seal for turbomachinery. volume DE-Vol 60, pages 139–148, Albuerquerque, New Mexico, 1993. ASME.

[68] John K. Vennard. *Elementary Fluid Mecanics*. John Wiley And Sons Inc, 1940.

[69] G. Vermes. A fluid mechanics approach to the labyrinth seal leakage problem. *ASME Transactions-Journal of Engineering for Power*, 83:161–169, 1961.

[70] John K. Whalen, Eduardo Alvarez, and Lester P. Palliser. Thermoplastic labyrinth seals for centrifugal compressors. *Procedings of the 33d Turbomachinery Symposium*, 2004.

[71] J. Xu, M. S. Ambrosia, and D. L. Rhode. Effectof tooth bending damange on the leakage of straight through labyrinth seals. In *ASME 2005 Fluids Engineering Division Summer Meeting*, number FEDSM2005-77455, Houston, Texas, USA, June 19-23, 2005.

[72] H. Zimmerman and K. H. Wolff. Comparison between empirical and numerical labyrinth flow correlations. *ASME 87-GT-86*, 1987.